

https://dspace.org/

Influence of synthesis conditions on solid phosphoric acid catalyst structure

Mahuhushe, Blessing

2022

https://hdl.handle.net/10539/35472

Downloaded from a DSpace repository. https://dspace.org/

Influence of synthesis conditions on solid phosphoric acid catalyst structure



UNIVERSITY OF THE
WITWATERSRAND,
JOHANNESBURG

A dissertation submitted to the Faculty of Science, University of the Witwatersrand, Johannesburg, in fulfilment of the requirements

for the degree of Master of Science.

By

Blessing Mahuhushe

Student number:

2039314



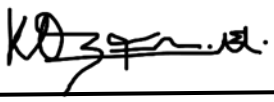
Blessing Mahuhushe — August 2021

Date



Dr Dean Barrett — August 2021

Supervisor — Date



Professor Kenneth I Ozoemena — August 2021

Co-Supervisor — Date

Declaration

I declare that the work reported herein is my own, unaided work, submitted at the school of Chemistry, University of the Witwatersrand, Johannesburg. This work has not been submitted for any degree or examination in any other institution of higher learning.



August 2021

Blessing Mahuhushe

Date

Abstract.

The effect of alkaline earth metals and transition metals such as calcium and vanadium on Solid phosphoric acid catalyst (SPA) structure is questionable. The influence of calcium and vanadium doping and other SPA catalyst synthesis conditions on the SPA catalyst structural parameters (that is, free acid, crystallinity, pore volume and mechanical hardness) was investigated.

The SPA catalyst was synthesized using the impregnation method at a mixing temperature of 75 ^{o}C using both amorphous and synthetic kieselguhr together with phosphoric acid. In addition to that, calcium and vanadium doped SPA catalyst was also synthesized. It was observed that the pre-calcination (drying the synthesis mixture at 200 ^{o}C for twenty minutes) step is crucial for the extrudability of the SPA reaction mixture. Different geometries of SPA catalysts such as cylindrical and quadrilobed shaped catalyst were synthesized and calcined at varying temperatures ranging from 400 ^{o}C up to 800 ^{o}C. The optimal calcination temperature of 500 ^{o}C was reported. The synthesized catalyst was characterized using XRD, N_2- adsorption, XRF, Mercury Intrusion Technique, TEM, STEM and EDS techniques.

Herein, pore volume data from the calcium and vanadium promoted SPA catalyst indicated that the SPA catalysts have the slit-shaped and ink-bottle type of pores. However, the un-promoted SPA catalyst exhibited a narrow distribution of uniform pores connected by constrictions. This forms the novelty part of this study since SPA catalyst porosity data is not available in the open literature.

SPA catalyst synthesized from synthetic kieselguhr exhibited higher crystallinity compared to SPA catalyst synthesized from amorphous kieselguhr. However, data from TEM characterization revealed that there is no difference in grain size of the SPA catalyst synthesized from amorphous and synthetic kieselguhr. Nevertheless, SPA catalyst calcium and vanadium doping foster the synthesis of larger crystal grains compared to the grains of un-promoted SPA catalyst. This led to the conclusion that the use of calcium and vanadium as doping agents will not result in the synthesis of SPA catalyst with higher mechanical strength compared to un-promoted SPA catalyst. EDS confirmed the homogeneous distribution of the calcium and vanadium atoms on the SPA catalysts surface.

Dedication

I dedicate this work to my daughter Nicole Panashe Mahuhushe, my better half Sarah Jatisai Rushwaya and my family at large.

Acknowledgements

- My sincerest appreciation goes to my supervisor's Dr Dean Barrett, Professor Kenneth I Ozoemena and Dr Jonathan Chetty. Thank you for helping me to traverse this academic journey and for your invaluable support and guidance.

- To Dr Jezreel Cloete, a special thank you for your constructive criticism it has been appreciated.

- My appreciation also goes to Clariant Sasol Catalyst for funding my studies. The School of Chemistry at the University of the Witwatersrand for allowing me to conduct my research.

- I would like to thank my wife and daughter for supporting me in pursuit of my dream and for all the sacrifices you have endured. Words truly cannot express my gratitude.

- Most importantly, to God my creator, thank you for answering my prayers and being with me always.

Table of contents

Abstract…… iv

Dedication……v

Acknowledgements……vi

List of figures……x

Chapter 1……x

Chapter 2……x

Chapter 3……x

Chapter 4……xii

List of tables……xiv

Chapter 2……xiv

Chapter 3……xiv

Chapter 4……xiv

List of abbreviations……xvi

Chapter 1……17

Introduction……17

Problem statement……21

Rationale and motivation……22

Dissertation overview……23

Literature review……23

1.2.1 Influence of phosphoric acid concentration on SPA catalyst parameters……24

1.2.2 The correlation between the SPA catalyst synthesis method and the final crystalline silicon phosphate polymorph……..26

1.2.3 The effect of the type of kieselguhr support on SPA catalyst physical and chemical parameters……..27

1.3 The influence of metal doping on SPA catalyst silicon phosphate crystalline phases……29

1.4 The effect of calcination temperature on SPA catalysts physical and chemical parameters……..…30

1.5 Influence of water content on SPA catalyst mechanical crushing strength……...32

1.6 PXRD characterization……...33

1.7 TEM characterization……..34

1.8 Objectives……..…35

1.9 References……..36

Chapter 2……..52

2.1 Effect of synthesis conditions on physical and chemical properties of SPA catalysts.52

2.2 Influence of the concentration of ancillary minerals in Kieselguhr on SPA catalyst physical and chemical properties……...53

2.3 Synthesis of the SPA catalysts……..58

2.4 Characterization of the synthesized SPA catalysts……...64

2.5 Conclusion……..70

2.6 References……71

Chapter 3……..79

3.1 Free Acid content of the synthesized SPA catalysts……..…79

3.2 Correlation between the crushing strength and porosity of the synthesized SPA catalysts……84

3.3 Mercury intrusion pore volume of the synthesized SPA catalysts……86

3.4 BET surface area of the synthesized SPA catalysts and their pore structure……93

3.5 Crystalline phases of the synthesized SPA catalysts……101

3.6 References……111

Chapter 4……120

4.1 Introduction……120

4.2 Crystal structure of SPA synthesized from mined kieselguhr……121

4.3 Crystalline grain size of the catalysts synthesized from synthetic and mined kieselguhr……122

4.4 Grain geometry of the synthesized SPA catalysts……129

4.5 Atomic composition of the SPA catalyst synthesized from both amorphous and crystalline kieselguhr……130

4.6 References……134

Chapter 5……139

5.1 Conclusions and recommendations for future studies……139

5.2 References……144

Appendix……146

Chapter 4 Supporting information……146

List of figures

Chapter 1

Figure 1.1 The reactant material oligomerized by SPA catalyst and the subsequent products……18

Chapter 2

Figure 2.1 PXRD diffractogram of synthetic and mined kieselguhr……54

Figure 2.2 Isothermal plot showing adsorption and desorption behaviour of mined kieselguhr……56

Figure 2.3 Isothermal plot showing adsorption and desorption behaviour of synthetic kieselguhr……...57

Figure 2.4 Synthesis of SPA catalysts process flow diagram……59

Figure 2.5 The photograph of the synthesized cylindrically shaped unpromoted SPAM catalyst using mined kieselguhr and calcined at 400 ^{o}C……61

Figure 2.6 The photograph of the SPAMCa catalyst calcined at 400 ^{o}C……62

Figure 2.7 The SPAMQ400 catalyst photograph showing the quadrilobed shaped extrudates……63

Figure 2.8 Cylindrically shaped SPAS400 catalyst synthesized from synthetic kieselguhr……64

Figure 2.9 The cylindrical-shaped SPASCa400 catalyst synthesized from synthetic kieselguhr……64

Chapter 3

Figure 3.1 Influence of calcination temperature on SPA catalyst free phosphoric acid…80

Figure 3.2 Variation in free phosphoric acid of the SPAM and SPAS catalyst synthesized from amorphous and crystalline kieselguhr……..81

Figure 3.3 Influence of calcination temperature on crushing strength (N/mm) of the SPAM, SPAS and SPASCa catalyst……..85

Figure 3.4 Mercury intrusion pore volume in mL/g of the SPAM, SPAMQ and SPAMV catalyst synthesized from mined kieselguhr……87

Figure 3.5 Influence of calcination temperature on pore volume of calcium promoted catalysts……89

Figure 3.6 Mercury Intrusion Pore volume of the synthesized SPA catalysts calcined at the optimal temperature of 500 ^{o}C……90

Figure 3.7 Mercury intrusion percentage pore diameter distribution for catalyst SPAM series……91

Figure 3.8 Influence of calcination temperature on catalyst SPAS and SPASCa pore volume compared to SPAM catalyst……93

Figure 3.9 BET surface area of the SPA catalyst synthesized from mined kieselguhr…….94

Figure 3.10 BJH desorption pore volume of the catalysts synthesized from mined kieselguhr……95

Figure 3.11 Isothermal linear plot showing adsorption and desorption behaviour of the SPAM500 catalyst……..96

Figure 3.12 Isothermal linear plot showing the adsorption and desorption characteristics of the SPAMCa500 catalyst……..97

Figure 3.13 Isothermal linear plot showing the adsorption and desorption behaviour of the SPAMQ500 catalyst……98

Figure 3.14 Isothermal linear plot showing the adsorption and desorption behaviour of the SPAMQCa500 catalyst……..99

Figure 3.15 Isothermal linear plot showing the adsorption and desorption characteristics of the SPAMV500 catalyst……..99

Figure 3.16a The isothermal linear plot showing adsorption and desorption behaviour of the SPAS500 catalyst……100

Figure 3.16b The Isothermal linear plot showing the adsorption and desorption characteristics of the SPASCa500 catalyst……101

Figure 3.17 Influence of calcination temperature on the transformation of silicon orthophosphate to silicon pyrophosphate of SPAM catalysts……..102

Figure 3.18 Influence of calcination temperature on crystalline phase transformations of the calcium promoted SPA catalysts synthesized from mined kieselguhr……..103

Figure 3.19. Effect of calcination temperature on the crystalline phase transformations of the vanadium promoted SPA catalysts synthesized from mined kieselguhr……..104

Figure 3.20 Influence of calcination temperature on the crystalline phases of the SPA catalyst synthesized from synthetic kieselguhr……..105

Figure 3.21 Influence of calcination temperature on the crystalline phase transformations of the calcium promoted SPA catalysts synthesized from crystalline synthetic kieselguhr……..106

Figure 3.22 Influence of calcination temperature on total relative crystallinity……..109

Chapter 4

Figure 4.1 Microstructure and SAED of the catalysts synthesized from amorphous kieselguhr……..121

Figure 4.2 Microstructure and SAED of the SPAS500 and SPASCa500 catalysts synthesized from crystalline synthetic kieselguhr……..122

Figure 4.3 The grain size box plot of SPAM500 and SPAS500……124

Figure 4.4 SPAM500 grain size distribution……125

Figure 4.5 SPAMCa500 grain size distribution……126

Figure 4.6 SPAMV500 grain size distribution……..127

Figure 4.7 SPAS500 grain size distribution……128

Figure 4.8 SPASCa500 catalyst grain size distribution……..128

Figure 4.9 The crystal morphology and shapes of the SPA catalysts synthesized from both amorphous and synthetic kieselguhr……..130

Figure 4.10 EDS map and the STEM image of SPAM500, SPAMCa500 and SPAMV catalyst……132

List of tables

Chapter 2.

Table 2.1 Percentile by volume particle size distribution of synthetic and mined kieselguhr……55

Table 2.2 BET surface area of synthetic and mined kieselguhr……57

Table 2.3 PXRD instrument settings used for all XRD experiments……67

Chapter 3

Table 3.1 Free acid (% P2O5) results for SPAM400 and SPAS400 catalysts……82

Table 3.2 Statistical data of catalyst SPAM400 and SPAS400……82

Table 3.3 Influence of calcination temperature on SPAM, SPAS and SPASCa crushing strength……85

Table 3.4 Mercury intrusion pore volume of the SPAM, SPAMQ and SPAMV catalyst synthesized from mined kieselguhr……87

Table 3.5 Influence of calcination temperature on pore volume of calcium promoted catalysts……88

Table 3.6 Mercury intrusion pore volume and BET surface area for SPAS and SPASCa catalyst……92

Table 3.7 Influence of calcination temperature on catalyst SPAS and SPASCa pore volume compared to SPAM catalyst……92

Table 3.8 Influence of calcination temperature on crystallite size of the SPA catalyst synthesized from amorphous and crystalline kieselguhr……107

Table 3.9 Variation in crystallite size of the SPA catalysts synthesized from amorphous and crystalline synthetic kieselguhr……108

Chapter 4

Table 4.1 The mean grain size of the unpromoted and promoted SPA catalyst measured by TEM……123

Table 4.2 The atomic composition of four major elements of solid phosphoric acid determined by STEM EDS……131

Table 4.3 Calcium and Vanadium composition determined by STEM EDS at different focal points of the sample……133

List of abbreviations

The following is the list of abbreviations used in the text.

SPA- Solid Phosphoric Acid

SPAM – Solid Phosphoric Acid catalyst synthesized from mined kieselguhr.

SPAMCa – Calcium promoted Solid Phosphoric Acid catalyst synthesized from mined kieselguhr.

SPAMV – Vanadium promoted Solid Phosphoric Acid catalyst synthesized from mined kieselguhr.

SPAS – Solid Phosphoric Acid catalyst synthesized from synthetic kieselguhr.

SPASCa – Calcium promoted Solid Phosphoric Acid catalyst synthesized from synthetic kieselguhr.

LOI- Loss On Ignition

XRD- X-Ray Diffraction

SiO_2- Silicon dioxide

XRF- X-ray Fluorescence

BET – Brunauer Emmett Teller.

PPA- Poly Phosphoric Acid

ICDD – International Centre for Diffraction Database

PXRD – Powder X-Ray Diffraction

TEM – Transmission Electron Microscopy

HRTEM- High-Resolution Transmission Electron Microscopy

STEM – Scanning Transmission Electron Microscopy

SAED – Selected Area Electron Diffraction.

ICSD - Inorganic Crystal Structure Database

SEM – Scanning Electron Microscopy.

EDX – Energy Dispersive X-ray.

EDS – Energy Dispersive Spectroscopy.

Gpa – Gigapascal.

Chapter 1

1. Introduction.

The synthesis of a solid phosphoric acid catalyst (SPA) from environmentally friendly raw materials (that is diatomaceous earth and phosphoric acid) led to it being characterized as an environmentally friendly catalyst. The diatomaceous earth(kieselguhr) is formed by the assembling of the remains of the obsolete diatoms in lakes or marine sediments[1]. The remains are composed of amorphous silica that can be used as structural support in catalysts synthesis. The diatomaceous earth is mined and dried at 200 ^{o}C to drive off volatiles and used without further processing[2]. The particle sizes of the kieselguhr used in SPA catalysts synthesis influence the structure of the catalyst. Very fine particles of the support foster marked aggregation of the SPA catalyst crystal grains. Contrary to that, synthesis of SPA catalyst using course kieselguhr particles promotes poor agglomeration of SPA catalyst crystal grains resulting in lower catalyst hardness[3].

The agglomeration mechanism of the SPA catalyst crystal grains in the catalyst crystal system dictates the pore structure of the catalyst and it is the structure of the pores that influences the pore volume of the SPA catalyst[4]. In catalysis science, open pores are the class of pores that are connected to the surface of the catalyst and they contribute to the pore volume of the catalyst. Whereas closed pores are a category of pores that are not accessible to the surface of the catalyst and do not contribute to the pore volume and specific surface area of the catalyst[5]. A study to investigate the optimum kieselguhr particle size that is needed for the development of porous SPA catalyst structure is required.

The chemical composition of the kieselguhr is somewhat influenced by its geological source[6]. Paunka et al., investigated diatomaceous earth naturally mined from Bulgaria and reported a silica content of 67 % and alumina concentration of 14 %[7]. However, Derek et al., reported 85 % silica content and alumina concentration of 4 % of the kieselguhr mined in the United States of America [8]. One would question the effect of the variation in the chemical composition of the kieselguhr on the structure of the SPA catalyst.

The SPA catalyst was invented by Ipatieff in late 1935[9] with the structure suited for the oligomerization of C_2-C_5 olefins. It was later used for alkylation of aromatics and conversion of propylene to distillate products[10].



Figure 1.1 The reactant material oligomerized by SPA catalyst and the subsequent products(adapted from reference 11)[11].

The oligomerization of short-chain alkenes over solid acid catalysts is a mature technology. However, it represents an efficient route for the synthesis of petrol and diesel for the transport industry[12]. As such the efficiency of the oligomerization reaction is somewhat related to the efficiency of the solid phosphoric acid catalyst and other solid acid catalysts[13]. It can be improved by the conventional method of manipulating the catalyst structure and the active phase of the catalyst[14].

The active component of the solid phosphoric acid catalyst is unbonded free phosphoric acid[15]. That is the phosphoric acid which is not chemisorbed to the kieselguhr support and this free acid is a Brønsted acid. The amount of free phosphoric acid in the SPA catalyst influences catalyst structure. It was reported that the SPA catalyst with 30 wt. % free acid and above is pulpy compared to a rigid catalyst with free acid of less than 30 wt. %[16]. The free phosphoric acid dissociates according to the following reaction scheme below to give dihydrogen phosphate and hydronium.

$$H_3PO_{4(aq)} + H_2O_{(aq)} \Leftrightarrow H_2PO^-_{4(aq)} + H_3O^+_{(aq)} \qquad K_{a1} = 7.25 \times 10^{-3}$$

Reaction scheme 1.1 The dissociation of phosphoric acid in an aqueous environment[17].

The free phosphoric acid fosters the formation of phosphoric acid propyl ester intermediate during the propylene oligomerization reaction. The formed propyl ester is unstable and decomposes to give phosphoric acid and a propyl dimer. The dimer further polymerizes into an oligomer of propylene[18].

The concentration of the free phosphoric acid in the SPA catalyst influences the amount of the acidic species(H_3O^+) in oligomerization reactions. High free acid content corresponds to higher SPA catalyst activity(higher propylene conversion rate)[19]. However, there are different types of free phosphoric acid reported in SPA catalysts dependening on synthesis conditions. The typical synthesis conditions of SPA catalyst are (i) Silica content of 95 %, (ii) P_2O_5 concentration of 72 %, (iii) Calcination temperature of 300 ^oC and (iv) Calcination time of 30 minutes [20].

Zhu et al., investigated the type of free phosphoric acid in a SPA catalyst to find the free acid species ratio in a SPA catalyst composed of 26 wt. % P_2O_5. The author reported that there is 35 wt. % H_3PO_4, 7 wt. % $H_4P_2O_7$ and less than 1 % polyphosphoric acid species in free acid [21]. Furthermore, if there is 9 – 26 wt. % P_2O_5 in the free acid, the SPA catalyst can have 75 wt. % propylene conversion. Nevertheless, their work did not study the influence of such high free phosphoric acid on the SPA catalyst structure.

Even though the amount of free acid depends on synthesis conditions it is also to a lesser extent dependent on the elemental concentration of the ancillary metals in kieselguhr support(Ca, K, Al and Fe)[22]. Santander et al., investigated the use of SPA catalyst for levoglucosenone production via cellulose fast pyrolysis. The authors synthesized aluminium promoted SPA catalyst and reported a correlation between the free acid and the concentration of aluminium in catalyst support. The higher the concentration of aluminium in synthesized SPA catalyst the lower the free acid. This was however due to the formation of aluminium phosphates[23]. The study is lacking on the effect of other ancillary minerals on the free phosphoric acid content in SPA catalyst.

Prinsloo et al., investigated the effect of low-quality kieselguhr on SPA catalyst parameters (that is free acid, silicon phosphate and acid to silica ratio). The author reported no variation in phosphoric acid. Moreover, the optimum ratio of the phosphoric acid to silica was found to be a

function of the morphology of the amorphous kieselguhr, the concentration of the acid, and the mixing temperature[24]. The author also reported the optimal mixing temperature of 150 ^{o}C.

The question could be, what would happen to the synthesis mixture if phosphoric acid and crystalline silica are mixed at lower temperatures? How could pre-calcination (drying at 200 ^{o}C for 20 minutes) influence the SPA catalyst crystal grain growth? In what way will the use of crystalline kieselguhr influence the SPA catalyst grain size? The solutions to the stated hypothesis could be used to determine the feasibility of using low mixing temperatures such as 75 ^{o}C. Low mixing temperature is beneficial to the development of homogeneous crystal grains especially in the presence of crystal seeds[25].

At the mixing temperatures(reaction temperature) below 100 ^{o}C, the mixture of phosphoric acid and amorphous kieselguhr is amorphous[26]. In fact, controlled calcination of the amorphous mixture could result in the development of the smallest possible homogeneously distributed crystal grains[27]. Smaller grains closely agglomerate compared to bigger grains which leave void spaces in their packing. The close packing of the small crystal grains enhances catalyst mechanical strength[28].

The structural integrity of the SPA catalyst is highly influenced by the presents of water. This is so even though the feed material used in the oligomerization reaction is hydrated[29]. The crystalline silicon phosphates of the SPA catalyst have hygroscopic and polar hydroxyl groups. These polar hydroxyl groups interact with the oxygen and hydrogen elements of water resulting in the formation of hydrogen bonding[30]. The formed hydrogen bonding partially weakens the silicon-phosphorus bond of the crystalline phases in the SPA catalyst. This influences the geometry of the catalyst structure ultimately causing structural collapse[31]. To that end, the development of the SPA catalyst with a structure that can tolerate hydration conditions of the feed material is required.

The solid phosphoric acid catalyst structural collapse contributes to pressure drop in the petrochemical reactor which follows the Forchheimer model[32]. The model tells us that pressure drop is the sum of viscous and inertial contributions[33]. Analysis of the solid phosphoric acid catalyst pressure drop data and reports points to the lack of continuous structural engineering

of the solid phosphoric acid catalyst structure[34]. The pellets or extrudates of SPA catalyst in a reactor suffers from mechanical stress that results in the formation of fines, which can cause turbulent fluid flow, blockage and pressure drop across the reactor and if not attended to, can cause variation in heat flux[35]. To that end, the generation of fines from the SPA pellets in a fixed bed reactor is considered a SPA catalyst mechanical hardness issue which is related to the SPA catalyst synthesis conditions.

Coetzee et al., investigated the influence of synthesis conditions on silicon phosphate, focusing on the effect of silicon pyrophosphate on the SPA catalyst hardness[36]. Their findings clarified the correlation between the silicon-pyrophosphate phase and the particle crushing strength of the catalyst. However, silicon pyrophosphate is not the only crystalline phase in SPA catalyst[37]. Further studies investigating the role of other crystalline phases such as silicon orthophosphate and silicon hydrogen phosphate are required to characterise their effects on catalyst hardness.

Aomura and Ohtsuka investigated the influence of the mineralogy of kieselguhr from different sources on the SPA catalyst structure. The author argued that, the geological origin of the kieselguhr influences the elemental composition of the kieselguhr consequently its density, the higher the concentration of ancillary metals(such as Al, Ca, K, Mg and Fe) in kieselguhr the higher the density of the kieselguhr[38].

The kieselguhr with high density fosters the synthesis of SPA catalyst with low free acid due to the formation of metal phosphates[39]. The author concluded that the most active SPA catalyst was synthesized from the kieselguhr with low bulk density, large micropore volume, high acid holding power, and high heat stability. Although true and correct, their study is lacking on the effect of crystalline kieselguhr on solid phosphoric acid catalyst parameters such as the pore volume, free acid, crushing strength and crystallinity.

2. Problem statement.

The environmental friendliness of the SPA catalyst makes it a preferred catalyst in the oligomerization and the synthesis of fine chemical processes[40]. However, the solid phosphoric acid catalyst crushing strength is reported to have a direct relationship with the oligomerization reactor pressure drop[41]. The SPA catalyst pellets in a packed bed reactor disintegrate into fine

powders, which agglomerates together causing the turbulent flow of the gaseous olefin feed, this result in pressure drop.

The SPA catalyst crushing strength is a structural problem that can be resolved by a controlled morphological manipulation[42]. Investigation into the synthesis conditions of the SPA catalyst such as calcination temperature can help to unravel the SPA catalyst crystallization mechanism[43]. Understanding the SPA catalyst crystallization mechanism helps the designing of the crystal grains with high grain boundaries that inhibit stress propagation and enhances SPA catalyst hardness[44].

The interconnection between synthesis conditions (that is, calcination temperature, shape formation and metal promotion) and catalyst structure (that is, crystallinity, porosity, pore size distribution, surface area and mechanical strength) is poorly understood. How does metal promotion influence the SPA catalyst crystal grain size? How will the metal-doped SPA catalyst crystal grain size influence the mechanical hardness and porosity of the catalyst? Therefore, how is the nanostructure related to the bulky properties of the catalyst, and in what way does it influence the overall parameters of the catalyst?

3. Rationale and Motivation.

SPA catalyst is traditionally calcined at temperatures below 400 ^{o}C[45], changes in the synthesis conditions, especially calcination temperature, alter the crystallite size[46]. Thermal treatment of the material will induce a cell expansion which could result in altered catalyst morphology.

The core issue is to bridge the knowledge gap between synthesis conditions and SPA catalyst parameters (chemical and physical parameters; that is free acid, porosity, mechanical hardness, and grain sizes). The ideal approach to effectuate this goal is based on the structural design of the catalyst, followed by controlled synthesis[47]. However, a prerequisite for a rational structural design of the solid phosphoric acid catalyst is a complete understanding of its structure[48]. Therefore, the investigation into the empirical relationship of catalyst synthesis conditions and their physicochemical properties is imperative.

4. Dissertation overview.

Chapter 1 introduced the study and provides the background and concepts to the study, by referring to the literature on these discourses and summarizing previous research on Solid Phosphoric Acid catalysts. Chapter 2 presents a description of the experimental work covering the SPA catalyst synthesis using both mined and synthetic kieselguhr as silica sources. Chapter 3 focuses on the presentation and discussion of the experimental data of the SPA catalysts that were synthesized in Chapter 2 and the interpretation of the results. Chapter 4 delves into the morphological study of the SPA catalyst. Chapter 5 draws the overall conclusions of the whole study, stating the limitations and suggestions for future work.

1.2 Literature Review.

The use of the solid phosphoric acid catalyst for oligomerization of olefins in petrochemical reactions has been around for nearly a century[49]. Various solid acid catalysts are used in the dimerization and trimerization reactions to yield C_7 - C_9 carbon chains[50]. The examples of solid acid catalysts are sulphated zirconium oxide, alumina silicates, MCM-41 supported tungstophosphoric acid catalyst and H-ZSM-5 zeolite[51]. The oligomerization process over solid acid catalysts has given the petrochemical industry flexibility in the synthesis of liquid fuels from polyalkenes compared to the use of a liquid mineral acid catalyst such as hydrofluoric acid and sulphuric acid[52].

The liquid mineral acids are very effective in oligomerization reactions however, they have a high acid regeneration cost due to purification and denitration[53]. In addition to that, they are environmentally hazardous with a high risk that can emanate from accidents during catalyst transportation and they are very corrosive to the reactor surfaces. The risk of using a liquid acid catalyst in oligomerization processes outweighs its benefit in favour of using a solid acid catalyst for the same process[54].

Solid Phosphoric Acid catalyst belongs to the group of solid acid catalysts used in oligomerization reactions[55]. The solid phosphoric acid catalyst was initially invented for catalytic polymerization of olefin by Ipatief[56]. The catalyst later found use in ethylation of benzene, in

Fischer-Tropsch processes, moreover SPA catalyst can be used in the upgrading of the Fischer-Tropsch processess[57].

The solid phosphoric acid catalyst is synthesized from environmentally friendly raw materials, that is diatomaceous earth and phosphoric acid [58]. Kieselguhr is mined and thermally treated to remove organic matter and impurities to match the catalyst grade requirements[59]. Its outstanding physical properties such as high silica content, low density because of a high porosity that fosters high BET specific surface area makes it a preferred candidate for catalyst support[60].

The phosphoric acid can be produced by three different methods which are (i) Wet process, (ii) Dry kiln process and (iii) Thermal process. However, thermal synthesis of phosphoric acid yields industrial grade (75-85 wt. % P_2O_5) of phosphoric acid that is suitable for the synthesis of solid phosphoric acid catalyst[61]. The process involves oxidation of elemental phosphorus in ambient air at temperatures above 1650 ^{o}C to give phosphorus pentoxide Reaction scheme 1.2 below.

$$P_4 + 5O_2 \longrightarrow 2P_2O_5$$

Reaction scheme 1.2 Synthesis of phosphorus pentoxide[62].

The synthesized phosphorus pentoxide is hydrated with water to give phosphoric acid syrup Reaction scheme 1.3 below.

$$2P_2O_5\ (s) + 6H_2O(l) \xrightarrow{\triangle} 4H_3PO_4(aq)$$

Reaction scheme 1.3 Synthesis of phosphoric acid from phosphorus pentoxide and water[63].

1.2.1 Influence of phosphoric acid concentration on SPA catalyst parameters.

Phosphoric acid has a broader range of applications, it can be used as an intermediate in pharmaceuticals especially in anti-nausea medicines[64]. In the food industry, phosphoric acid is used as a food additive that acts as an acidity regulator and an acidulant in beverage drinks[65]. Above all, 80 % of the produced phosphoric acid find its application in the synthesis of fertilizers in the agriculture industry[66].

In catalysis, the concentration of the phosphoric acid used depends on the application of the synthesized catalyst. The phosphoric acid with P_2O_5 concentration below 50 % can be used for the catalysis of Passerini reaction[67]. The phosphoric acid used for the synthesis of SPA catalyst

with application in oligomerization reactions requires that the concentration of P_2O_5 be 70 % and higher[68]. This is done to ensure that the free acid concentration requirement of the oligomerization reaction can be achieved.

The naming of a phosphoric acid(PA) species is derived from the number of phosphorus atoms in a phosphoric acid polymer $H_{n+2}P_nO_{3n+1}$, where n is an integer. If there is one phosphorus atom such as H_3PO_4, the acid species is called orthophosphoric acid, two phosphorus atoms such as in $H_4P_2O_7$, the name becomes pyrophosphoric acid and if they are as many as n phosphorus atoms, n>3, the acid is called polyphosphoric acid[69].

The phosphoric acid concentration is expressed in terms of percentage weight phosphorus pentoxide[70], alternatively, it can be expressed as an equivalent percentage H_3PO_4 (% H_3PO_4) mass % $\frac{p}{0.316}$. However, 100 % H_3PO_4 does not consist of a single species but a mixture of water, H_3PO_4, and $H_4P_2O_7$ it is also referring to the state of dryness [71]. As a result, when phosphoric acid is impregnated on a silicon dioxide support, the acid strength and proton density do not have a direct relationship with the phosphoric acid concentration[72].

In a typical catalytic reaction, different surface geometries provide different configurations to the reactant molecule for bonding [73]. Phosphoric acid exhibits self-dissociative behaviour as shown in Reaction scheme 1.4 below.

$$2H_3PO_4 \longleftrightarrow H_4\,PO_4^+ + H_2PO_4^-$$

$$2H_3PO_4 \longleftrightarrow H_4P_2O_7 + H_2O$$

$$3H_3PO_4 \longleftrightarrow H_4PO_4^+ + H_2P_2O_7^{2-} + H_3O^+$$

Reaction scheme 1.4 Self-dissociative behaviour of phosphoric acid[74].

The self-dissociative property is liable for Brønsted acid sites on SPA catalyst, these acid sites promote oligomerization reactions to proceed via both carbocation and ester formation routes[75].

Reaction scheme 1.4 shows that orthophosphoric acid and pyrophosphoric acid can coexist in equilibrium. During the preparation of the SPA catalyst, phosphoric acid reacts with silicon dioxide to form different phosphate phases[76]. It is reported that pyrophosphoric acid has better catalytic activity in olefin oligomerization[77]. However, the influence of either orthophosphoric

acid or pyrophosphoric acid on the morphology of the solid phosphoric acid catalyst remains questionable.

1.2.2 The correlation between the SPA catalyst synthesis method and the final crystalline silicon phosphate polymorph.

Silicon and phosphorus are the major elements that form the cornerstone of the solid phosphoric acid catalyst. As such it is a silicon phosphate-based catalyst, various methods have been used to synthesize silicon phosphates such as non-hydrolytic sol-gel reaction[78]. In which, nanocrystalline silicon orthophosphate was synthesized via condensation of silicon acetate, and tris(trimethylsilyl) phosphate. The reaction was carried out in non-aqueous solvents driven by the elimination of trimethylsilyl acetate which provides a homogeneous network with a high content of Si–O–P bonds[78]. The method is difficult to control and can result in the synthesis of amorphous and crystalline silicon phosphate phases containing octahedral SiO_6 units.

Furthermore, high temperature and the high-pressure reaction of silica, P_4O_{10} and H_3PO_4 have been used to synthesize silicon-phosphate compounds[79]. This method was successfully used to synthesize silicon pyrophosphate from silicon orthophosphate. The starting material was silicon orthophosphate that was subjected to 16 GPa(Giga Pascal) pressure and a maximum sintering temperature of 2000 ^oC targeting a single crystal of silicon pyrophosphate[80]. This method is difficult to control and can result in the synthesis of different and undesired silicon phosphate phases. This is clarified by the formation of eight different structural polymorphs of silicon pyrophosphate reported by the author on using this method[81].

In addition to that, researchers have attempted to synthesise silicon phosphate material with high purity by exploiting the chemistry of the $m\mathbf{SiO_2}–n\mathbf{P_2O_5}$ system, where *m* and *n* are the molar ratios of the silica and phosphorus pentoxide, respectively. Stearns et al., synthesized silicon phosphate hydroxide, $SiPO_4(OH)$, at 8.3 Gigapascal and 1000 ^oC[82]. However, after doubling the pressure and temperature conditions, that is at 16 Gigapascal and 2000 ^oC, Leinenweber et al., synthesized high-pressure crystalline polymorph of SiP_2O_7. The formed silicon pyrophosphate was as stable as the same SiP_2O_7 synthesized at ambient conditions[80].

The high pressure and high-temperature synthesis conditions suffer from reproducibility challenges, it is difficult to control the polymorph of the crystalline silicon phosphate material that can be synthesized by the high pressure and temperature conditions.

The preferred solid phosphoric acid catalyst synthesis method is the impregnation method due to its versatility. Whereby, phosphoric acid is impregnated on the porous kieselguhr and mixed in a mixing chamber to form a paste which could be calcined in air to foster crystallization[83]. The calcination conditions can be altered depending on the desired crystalline silicon phosphate phase. The impregnation synthesis technique allows the researcher to tailor a variety of synthesis conditions and optimize the catalyst parameters such as free acid, mechanical hardness, porosity, and silicon to phosphorus ratio[84].

The solid phosphoric acid catalyst used for polypropylene oligomerization is synthesized targeting the phosphorus to silicon ratio of 1.5 and above. Phosphorus to silicon ratios that are lower than 1.5 means the catalyst does not have enough free phosphoric acid to catalyze the propylene oligomerization reactions[85]. This is because the active component in the SPA catalyst is the free phosphoric acid that depends on the relative amount of P_2O_5 in the catalyst. Therefore, lower phosphorus to silicon ratio means lower P_2O_5 content ultimately lower free acid and consequently poor catalytic activity[86].

1.2.3 The effect of the type of kieselguhr support on SPA catalyst physical and chemical parameters.

Kieselguhr is formed from the remains of obsolete diatoms deposited in ocean or lakes, mined, ground up and processed to suit the end-user requirements[87] it is rich in silicon dioxide. Acidic treatment of kieselguhr can change the physical and chemical parameters of the support material. Khraisheh et al., treated diatomaceous earth with sulphuric acid and hydrochloric acid[88]. The author reported that the hydrochloric acid treatment of the kieselguhr resulted in the removal of the surface OH groups of the support. The process ultimately reduced the surface area on the surface of the kieselguhr, this lowers the efficiency of the SPA catalyst.

R. Wang, et al., assumed that the kieselguhr support does not influence the activity of the SPA catalyst[89]. Contrary to Kotsarenko et al., findings reported that the diatomaceous earth support forms the phosphates which are catalytically active[90]. However, there is a general agreement among the research community that, there is an interrelationship between the surface phosphoric acid and the crystalline silicon phosphates of the SPA catalyst support[91]. In an oligomerization reaction, the water in the feed material hydrolyses the crystalline silicon phosphates of the SPA catalyst support and reinstitute the acidic P–OH groups on the SPA catalyst surface[92]. To that end, the SPA catalyst with high crystalline silicon phosphates content has longer catalyst life compared to the SPA catalyst with low crystalline silicon phosphates[93].

Gianguido, et al., studied Phosphoric acid on silica, alumina, and titania focusing on catalyst surface acidity and reactivity towards olefin oligomerisation[94]. In their findings, alumina and titania supported catalysts reported higher total acid. This was due to the availability of both Lewis and Brønsted sites on alumina and titania supported catalyst whilst there was only Brønsted acid sites reported for silica-supported phosphoric acid catalyst[95]. Nevertheless, the study is silent on the optimum concentration of the alumina. Alumina can react with phosphoric acid at ambient conditions to form molecular sieve aluminium phosphate rendering the phosphoric acid poisoned for the oligomerization reaction[96].

$$Al_2O_3 \quad + \quad 2H_3PO_4 \longrightarrow \quad 2AlPO_4 \quad + \quad 3H_2O$$

Reaction scheme 1.5 Formation of aluminium phosphate from the reaction of aluminium oxide and phosphoric acid[97].

In a similar study, Fougret et al., studied the effect of the carrier material on the performance of SPA catalyst during hydration of ethylene. The support material that was used to synthesize the SPA catalyst used for their investigation was zinc oxide/titania, tin oxide/titania, zirconia oxide and niobic acid [98]. All these oxides reported poor catalytic activity which can be attributed to the formation of strong bonds between the support material and phosphoric acid[99].

$$3ZnO + 2H_3PO_4 \longrightarrow Zn_3(PO_4)_2 + H_2O$$

Reaction scheme 1.6 Formation of zinc phosphate from a reaction of zinc oxide and orthophosphoric acid[100].

The formed zinc orthophosphate is insoluble in water therefore once the surface phosphoric acid is used up during catalytic oligomerization there is no replenishment of the acidic group P-OH this explains the low catalytic activity of the zinc oxide/titania supported SPA catalyst. A good SPA catalyst carrier should have weak interactions between the support material and phosphoric acid [101].

1.3 The influence of metal doping on SPA catalyst silicon phosphate crystalline phases.

Vanadium is not part of the naturally found metals in kieselguhr, but its phosphates $VO(PO_3)_2$ and $(VO)_2P_2O_7$ are used for the oxidation of alkanes and aldol condensation of formaldehyde with acetic acid to form methyl vinyl ketone [102]. Vanadium pyrophosphate phase $(VO)_2P_2O_7$ shares structural similarities to silicon pyrophosphate (SiP_2O_7) phase in SPA catalyst[103]. The $(VO)_2P_2O_7$ can be synthesized by reacting vanadium pentoxide and phosphoric acid according to the following synthesis scheme.

$$V_2O_5 + H_3PO_3 \longrightarrow 2VO_2 + H_3PO_4$$

$$VO_2 + H_3PO_4 \longrightarrow VOHPO_4 0.5H_2O + 0.5H_2O$$

Reaction scheme 1.7 Synthesis of vanadium hemihydrate[104].

The reduction of the hemihydrate could be aided by the use of hydrocarbon solvents[105], after which it can undergo a structural transformation in the calcination step to give $(VO)_2P_2O_7$. The $(VO)_2P_2O_7$ crystallizes into a monoclinic symmetry with a space group $P2_1$ and lattice parameters a = 7.28 Å, b = 16.58 Å and c = 9.58 Å and β = 89.97 º [106]. The vanadium pyrophosphate can be formed in excess if the starting material have the P: V ratio of 2 or more[106,107]. The structure of the $(VO)_2P_2O_7$ closely resemble that of silicon pyrophosphate SiP_2O_7 which is a SPA catalyst crystalline component phase[108]. Having said that, the effect of vanadium pyrophosphate on the physical parameters of the solid phosphoric acid catalyst was questionable.

Researchers have suggested that the synthesis of composite compounds have a positive additive effect on final material[109]. This implies that for a solid phosphoric acid catalyst, the

catalyst hardness which is influenced by silicon pyrophosphate can be improved by additional vanadium pyrophosphate if the catalyst is promoted by vanadium.

Hypothetically, the addition of vanadium pentoxide to a synthesis mixture of phosphoric acid and silicon dioxide could result in the composite formation of vanadium pyrophosphates and silicon pyrophosphates phases[110]. In view of that, vanadium was selected as a suitable candidate for the promotion of solid phosphoric acid catalyst. Herein, vanadium pentoxide was used to synthesize vanadium promoted solid phosphoric acid catalyst to enhance SPA catalyst crushing strength[111].

1.4 The effect of calcination temperature on SPA catalysts physical and chemical parameters.

Calcination temperature is an important factor in determining the physicochemical parameters of the catalyst. It influences the catalyst hardness, crystal structure, pore volume and pore size distribution[112].

1.4.1 Influence of calcination temperature on SPA catalyst silicon phosphate crystalline phases.

Phosphoric acid and Silicon dioxide react to form different silicon phosphate species as presented in Reaction scheme 1.8 below.

$$SiO_2 + 2H_3PO_4 \longleftrightarrow Si(HPO_4)_2.H_2O + H_2O$$

$$5SiO_2 + 6H_3PO_4 \longleftrightarrow Si_5O(PO_4)_2 + 9H_2O$$

$$5SiO_2 + 10H_3PO_4 \longleftrightarrow 5SiP_2O_7 + 15H_2O$$

$$SiO_2 + 3H_3PO_4 \longleftrightarrow SiHP_3O_{10} + 4H_2O$$

Reaction scheme 1.8 Reaction of silicon dioxide and phosphoric acid to give different silicon phosphates[86].

Historically, two different silicon phosphate phases were reported as silicon orthophosphate and silicon pyrophosphate respectively[113]. Thomas et al., investigated the synthesis, structure, and acid function of solid phosphoric acid catalysts using nuclear magnetic resonance. The author reported the presence of silicon orthophosphate and silicon pyrophosphate phases and a further phase of silicon hydrogen phosphate monohydrate[92]. The author suggested a direct proportionality between phase distribution and calcination temperatures. Their study is lacking on the effect of the identified crystalline phases on the pore volume of the SPA catalyst.

1.4.2 The correlation between calcination conditions and silicon pyrophosphate polymorph.

Coetzee et al., investigated the effect of calcination temperature on SPA catalyst hardness[36], the author reported that an increase in calcination temperature results in an increase in the conversion of silicon orthophosphate to silicon pyrophosphate. Although true as it is, the report is lacking details such as what is the optimal calcination temperature that gives optimal silicon pyrophosphate which will ultimately give optimal SPA catalyst hardness? What is the crystallite size range that corresponds to the beneficial calcination temperature, how does the atomic distribution of the silicon and phosphorus atoms on the SPA catalyst influence the catalyst mechanical hardness? Nevertheless, in this work, the study of the crystallite and grain size was conducted, the knowledge gained could be used to investigate the rate of formation of the silicon phosphates and optimal porosity.

1.4.3 The effect of calcination temperature on SPA catalysts pores volume and pore structure.

The internal void space is an important parameter of the SPA catalysts, as it defines SPA catalyst permeability to reactants, products and finally, it's mass and heat transfer coefficient[114]. The pore shapes, size and pore size distribution directly influences the SPA catalyst activity and selectivity[115]. The rate of the product formation in SPA catalytic reaction is a function of available surface area which is directly influenced by the pore size distribution and pore structure. The details of SPA catalyst porosity, pore size distribution and the effect of synthesis conditions on the SPA catalyst pore structure are not available in the open literature.

The understanding of the science of porosity provides invaluable information for the development of porous SPA catalyst[116]. The catalyst micropores can limit the size of reactants that can diffuse through them and vastly contribute to the specific surface area[117]. The catalyst characterized by micropores has a larger specific surface area compared to the catalyst characterized by macropores[118]. Typically, there are two types of pores in catalyst materials, these are.

(i) Closed pores, these pores are inaccessible to the catalyst surface and reacting species, it may be such that some of the internal surface areas is inaccessible to bulky reactant molecules and can limit the rate of conversion to products[119].

(ii) Open pores are pores with the opening of the pore channel accessible to the catalyst surface and the reactants and products, they contribute to the rate of conversion of reactants to products[120].

However, porosity and pore shape is affected by calcination, an uncontrolled increase in calcination temperature can cause material thermal shock, resulting in microcracks which can be wrongly quantified as pore volume of the SPA catalyst[121]. The over calcination of the catalyst can result in catalytic material loss and false-positive pore volume[122]. In this work, SPA catalyst pore volume is defined as all cavities and void spaces found in the catalyst.

The catalyst pore size can be controlled successfully through morphological manipulation and various synthesis methods. Targeting synthesis of hierarchical pores in SPA catalyst, corn starch was added during synthesis at impregnation temperature of 75 ^{o}C[123]. This enhances porosity but hardness might shift towards the lower side. This is so because porosity is inversely proportional to mechanical hardness, that is the catalyst with high porosity exhibits lower catalyst hardness[124]. Herein, the influence of synthesis conditions on SPA catalyst pore structure was investigated.

1.5 Influence of water content on SPA catalyst mechanical crushing strength.

Significant work has been done to investigate the influence of hydration on SPA catalyst performance, however, more focus was directed on hydration from the feed during catalysis.

Bethea et al., reported that high hydration levels negatively affect activity and catalyst lifetime[125]. This is because water molecules form hydrogen bonding with silicon phosphates thereby hydrolyzing the silicon phosphates resulting in SPA catalyst structural collapse, yet under hydration, can result in the SPA catalyst becoming brittle and prone to high catalyst loss on attrition[126]. SPA catalyst structural collapse and attrition pitfalls are both related to the levels of water in the SPA catalyst structure.

During SPA catalyst synthesis water can be added as steam on calcination process step[127]. The effect of water addition during calcination on the SPA catalyst properties was initially investigated by Fougret et al., the author reported that an increase in hydration during calcination results in an increase in unbonded free phosphoric acid[128]. In a similar study, Coetzee et al., clarified that increasing the water concentration reduces the relative silicon pyrophosphate content and the catalyst crushing strength ultimately lowering the SPA catalyst crushing strength. In addition to that, the amount of free acid in the SPA catalyst increased with an increase in water concentration. These observations indicate that silicon pyrophosphate reacts with water to form silicon orthophosphate and silica in a hydrolysis reaction[129].

1.6 PXRD characterization.

1.6.1 Introduction

Knowledge of catalyst composition and structure is vital to the understanding of catalysis chemistry. PXRD offers a unique way to accurately measure atomic spacing, strain and preferred orientation[130]. It is widely used for the characterization of solid, crystalline materials[131]. Information from a diffraction experiment can be used to fingerprint the material under analysis with the aid of a suitable database[132].

1.6.2 Crystallography

Diffraction experimental results provide useful information such as peak intensities which are determined by atomic coordinates within a unit cell as well as scattering factors. Peak positions (d-spacing) are influenced by the shape, size, and symmetry of the unit cell. The peak shape is

affected by instrumental effects and the microstructure of sample [133]**.** A crystal is a solid made up of repeating unit cells in three-dimensional space[134]. A crystal structure and its diffraction pattern are related to each other by Fourier transformation from reciprocal to real space[135]. The diffraction pattern is a Fourier transform of the crystal structure, corresponding to the pattern of waves diffracted from an incident X-ray beam by a single crystal. The unit cell has lattice points which are geometric locations of atoms [136]. The arrangement of these atoms in a unit cell is described by Miller indices, which have a constant distance between parallel hkl throughout the lattice and is referred to as d-spacing[137]. The d-spacing is unique to each crystalline phase, hence we can use them to identify crystalline phases in reference peaks[138]

The data from XRD can be used to calculate crystallite size using the Scherrer model with an assumption that all crystallites are spherical[139]. This model is prone to errors, especially if the sample under investigation has non-spherical crystallites. That being said, Transmission Electron Microscopy was here used as a complementary technique to allow visualization of the shape of the crystal grains of the synthesized SPA catalysts[140].

1.7 TEM characterization.

Transmission electron microscopy (TEM) was used to investigate the SPA catalysts morphology as a complementary technique to PXRD. TEM utilizes a beam of electrons that passes through the ultra-thin sample to the detector, a 2D image is formed using a charge-coupled device camera[141]. The images can be used to extract morphological, compositional, and crystallographic information engrained in them. This technique can create high-resolution 2D images which are easier to interpret compared to 3D SEM images[142]. The 2D TEM images allow the researcher to view the sample at a molecular level and investigate a wide range of characteristics[143].

1.8 Objectives

The main objectives of this study are to

i. Synthesize cylindrical Solid Phosphoric Acid catalyst using phosphoric acid.

ii. Synthesize cylindrical calcium promoted Solid Phosphoric Acid catalyst using phosphoric acid.

iii. Synthesize quadrilobed Solid Phosphoric Acid catalyst using phosphoric acid.

iv. Synthesize quadrilobed calcium promoted Solid Phosphoric Acid catalyst using phosphoric acid.

v. Synthesize vanadium promoted Solid Phosphoric Acid catalyst using phosphoric acid.

vi. Investigate the effect of calcination temperature on crystallinity.

vii. Study the influence of catalyst shape on porosity, crush strength and surface area.

viii. Investigate the influence of synthesis conditions on catalyst structure and morphology.

1.9 References.

(1) Šaponjić, A.; Stanković, M.; Majstorović, J.; Matović, B.; Ilić, S.; Egelja, A.; Kokunešoski, M. Porous Ceramic Monoliths Based on Diatomite. *Ceram. Int.* **2015**, *41* (8), 9745–9752. https://doi.org/10.1016/j.ceramint.2015.04.046.

(2) Calvert, R. Diatomaceous Earth. *ACS Sustain. Chem. Eng.* **1930**, No. 52.

(3) Yang, B.; Vehoff, H. Dependence of Nanohardness upon Indentation Size and Grain Size - A Local Examination of the Interaction between Dislocations and Grain Boundaries. *Acta Mater.* **2007**, *55* (3), 849–856. https://doi.org/10.1016/j.actamat.2006.09.004.

(4) Hajnos, M. Porosimetry. In *Encyclopedia of Earth Sciences Series*; Springer Netherlands, 2011; Vol. Part 4, pp 647–650. https://doi.org/10.1007/978-90-481-3585-1_125.

(5) Villarroel Rocha, J.; Barrera, D.; Sapag, K. Improvement in the Pore Size Distribution for Ordered Mesoporous Materials with Cylindrical and Spherical Pores Using the Kelvin Equation. In *Topics in Catalysis*; 2011. https://doi.org/10.1007/s11244-011-9631-z.

(6) Datsko, T. Y.; Zelentsov, V. I.; Dvornikova, E. E. Physicochemical and Adsorption-Structural Properties of Diatomite Modified with Aluminum Compounds. *Surf. Eng. Appl. Electrochem.* **2011**, *47* (6), 530–539. https://doi.org/10.3103/S1068375511060081.

(7) Vassileva, P. S.; Apostolova, M. S.; Detcheva, A. K.; Ivanova, E. H. Bulgarian Natural Diatomites: Modification and Characterization. *Chem. Pap. 2012 673* **2012**, *67* (3), 342–349. https://doi.org/10.2478/S11696-012-0272-X.

(8) Purchas, D. B.; Sutherland, K. Packed Beds. In *Handbook of Filter Media*; Elsevier, 2002; pp 411–452. https://doi.org/10.1016/b978-185617375-9/50011-0.

(9) Ipatieff, V. N.; Corson, B. B. Gasoline from Ethylene by Catalytic Polymerization. *Ind. Eng. Chem.* **1936**. https://doi.org/10.1021/ie50319a027.

(10) Egloff, G.; Jones, E. K. New and Advanced Developments in Tetramer, Cumene and Motor Polymer Manufacture. In *World Petroleum Congress Proceedings*; 1955.

(11) Wang, R.; Li, Y.; Guo, B.; Sun, H. Catalytic Mechanism of MCM-41 Supported Phosphoric Acid Catalyst for FCC Gasoline Desulfurization by Alkylation: Experimental and Theoretical Investigation. *Energy and Fuels* **2011**. https://doi.org/10.1021/ef200705b.

(12) Corma, A.; Iborra, S. Oligomerization of Alkenes. In *Catalysts for Fine Chemical Synthesis*; John Wiley & Sons, Ltd: Chichester, UK, 2006; Vol. 4, pp 125–140. https://doi.org/10.1002/0470094214.ch6.

(13) Saavedra Lopez, J.; Dagle, R. A.; Dagle, V. L.; Smith, C.; Albrecht, K. O. Oligomerization of Ethanol-Derived Propene and Isobutene Mixtures to Transportation Fuels: Catalyst and Process Considerations. *Catal. Sci. Technol.* **2019**, *9* (5), 1117–1131. https://doi.org/10.1039/c8cy02297f.

(14) Max, J. H.; Chia, W. L.; Ning, Y. Promoting Heterogeneous Catalysis beyond Catalyst Design. *Chem. Sci.* **2020**, *11*, 1456–1468. https://doi.org/10.1039/c9sc05947d.

(15) Mashapa, T. N.; de Klerk, A. Solid Phosphoric Acid Catalysed Conversion of Oxygenate Containing Fischer-Tropsch Naphtha. *Appl. Catal. A Gen.* **2007**. https://doi.org/10.1016/j.apcata.2007.08.001.

(16) Ipatieff, V. N.; Schmerling, L. Ethylation of Benzene in Presence of Solid Phosphoric Acid. *Ind. Eng. Chem.* **1946**, *38* (4), 400–402. https://doi.org/10.1021/ie50436a017.

(17) Nims, L. F. The First Dissociation Constant of Phosphoric Acid from 0 to 50°. *J. Am. Chem. Soc.* **1934**, *56* (5), 1110–1112. https://doi.org/10.1021/ja01320a031.

(18) Forestière, A.; Olivier-Bourbigou, H.; Saussine, L. Oligomerization of Monoolefins by Homogeneous Catalysts and Adsorbents: From Molecular Insight to Industrial Optimization Catalyseurs et Adsorbants : De La Compréhension Moléculaire à l'optimisation Industrielle. *Oil Gas Sci. Technol. IFP* **2009**, *64* (6), 649–667. https://doi.org/10.2516/ogst/2009027.

(19) Lawrence N Jacob. Reactivation of Solid Phosphoric Acid Catalyst the United States Patent US2945822A. United States Patent US2945822A, 6 December 1957.

(20) Ipatieff, V. N.; Schaad, R. E. Mixed Polymerization of Butenes by Solid Phosphric Acid Catalyst. *Ind. Eng. Chem.* **2002**, *30* (5), 595–599. https://doi.org/10.1021/IE50341A024.

(21) Zhu, Z.; Xie, Z.; Chen, Y.; Wang, R.; Yao, Y. Free Phosphoric Acid of Diatomite-Phosphate Solid Acid and Its Catalytic Performance for Propylene Oligomerization. *React. Kinet. Catal. Lett.* **2000**. https://doi.org/10.1023/a:1010369707149.

(22) Korunić, Z.; Liška, A.; Lucić, P.; Hamel, D.; Rozman, V. Evaluation of Diatomaceous Earth Formulations Enhanced with Natural Products against Stored Product Insects. *J. Stored Prod. Res.* **2020**, *86*, 101565. https://doi.org/10.1016/j.jspr.2019.101565.

(23) Santander, J. A.; Alvarez, M.; Gutierrez, V.; Volpe, M. A. Solid Phosphoric Acid Catalysts Based on Mesoporous Silica for Levoglucosenone Production via Cellulose Fast Pyrolysis. *J. Chem. Technol. Biotechnol.* **2019**, *94* (2), 484–493. https://doi.org/10.1002/JCTB.5795.

(24) Prinsloo, N. M. Preparation of a Solid Phosphoric Acid Catalyst from Low-Quality KieselguhrParameters Controlling Catalyst Quality and Performance. *Ind. Eng. Chem. Res.* **2007**, *46* (23), 7838–7843. https://doi.org/10.1021/IE070644G.

(25) Allahyarov, E.; Sandomirski, K.; Egelhaaf, S. U.; Löwen, H. Crystallization Seeds Favour Crystallization Only during Initial Growth. *Nat. Commun.* **2015**, *6* (1), 1–9. https://doi.org/10.1038/ncomms8110.

(26) Ohtsuka, H.; Aomura, K. Activation of Solid Phosphoric Acid by Heat Treatment. *Bull. Japan Pet. Inst.* **1962**, *4*, 3–14. https://doi.org/10.1627/jpi1959.4.3.

(27) Gasser, U.; Weeks, E. R.; Schofield, A.; Pusey, P. N.; Weitz, D. A. Real-Space Imaging of Nucleation and Growth in Colloidal Crystallization. *Science (80-.).* **2001**, *292* (5515), 258–262. https://doi.org/10.1126/science.1058457.

(28) McMahon, C. J.; Gentner, D. H.; Ucisik, A. H. An Investigation of the Effects of Grain Size and Hardness in Temper-Embrittled 2 1/4 Cr-1 Mo Steel. *J. Eng. Mater. Technol. Trans. ASME* **1984**, *106* (1), 66–70. https://doi.org/10.1115/1.3225678.

(29) Van Werner Merwe, D. E. R. Conversion of Spent Solid Phosphoric Acid Catalyst to

Environmentally Friendly Fertilizer. *Environ. Sci. Technol.* **2010**. https://doi.org/10.1021/es902603d.

(30) Friedman, P.; Pinder, K. L.; Pinder, K. L. Kinetics of Polymerization of Olefins in Production of Polymer Gasoline. *Ind. Eng. Chem. Process Des. Dev.* **1971**. https://doi.org/10.1021/i260040a021.

(31) Chakrabarty, M.; Mukherjee, R.; Mukherji, A.; Arima, S.; Harigaya, Y. Phosphoric Acid-on-Silica Gel: A Green Catalyst for the Synthesis of Symmetrical Bis(Indolyl)Alkanes. *Heterocycles* **2006**. https://doi.org/10.3987/COM-06-10783.

(32) Wu, D.; Song, L.; Zhang, B.; Li, Y. Effect of the Mechanical Failure of Catalyst Pellets on the Pressure Drop of a Reactor. *Chem. Eng. Sci.* **2003**, *58* (17), 3995–4004. https://doi.org/10.1016/S0009-2509(03)00286-0.

(33) Johnson, O. Acidity and Polymerization Activity of Solid Acid Catalysts. *J. Phys. Chem.* **1955**. https://doi.org/10.1021/j150531a007.

(34) Klerk, A. D.; Furimsky, E. *Catalysis in the Upgrading of Fischer – Tropsch Syncrude*; RSC Catalysis Series, 2010.

(35) Kishore Ravindran, G. M. Impact of Shape and Size of Catalysts on the Physical Properties and Pressure Drop in Fixed Bed Catalytic Systems. *Int. J. Innov. Technol. Explor. Eng.* **2020**, *9* (6), 1103–1109. https://doi.org/10.35940/ijitee.f4214.049620.

(36) Coetzee, J. H.; Mashapa, T. N.; Prinsloo, N. M.; Rademan, J. D. An Improved Solid Phosphoric Acid Catalyst for Alkene Oligomerization in a Fischer-Tropsch Refinery. *Appl. Catal. A Gen.* **2006**, *308*, 204–209. https://doi.org/10.1016/j.apcata.2006.04.023.

(37) Edward, H. O. P.; Gary, Y. U. O. P. Method for the Manufacture of Solid Phosphoric Acid Catalyst, United States of America Patent. US3673111A, 1970.

(38) Prinsloo, N. M. Solid Phosphoric Acid Oligomerisation: Manipulating Diesel Selectivity by Controlling Catalyst Hydration. *Fuel Process. Technol.* **2006**. https://doi.org/10.1016/j.fuproc.2005.11.005.

(39) Parmar, D.; Sugiono, E.; Raja, S.; Rueping, M. Complete Field Guide to Asymmetric BINOL-Phosphate Derived Brønsted Acid and Metal Catalysis: History and Classification by Mode of Activation; Brønsted Acidity, Hydrogen Bonding, Ion Pairing, and Metal Phosphates. *Chem. Rev.* **2014**, *114* (18), 9047–9153. https://doi.org/10.1021/CR5001496.

(40) De Klerk, A.; Nel, R. J. J. Phenol Alkylation with 1-Octene on Solid Acid Catalysts. *Ind. Eng. Chem. Res.* **2007**. https://doi.org/10.1021/ie0706459.

(41) Lacroix, M.; Nguyen, P.; Schweich, D.; Pham Huu, C.; Savin-Poncet, S.; Edouard, D. Pressure Drop Measurements and Modeling on SiC Foams. *Chem. Eng. Sci.* **2007**, *62* (12), 3259–3267. https://doi.org/10.1016/j.ces.2007.03.027.

(42) Yang, W.; Ding, F.; Sang, L.; Ma, Z.; Shao, and Shao, G. Carbon. **2017**, No. 111, 419–427.

(43) Schilling, T.; Schöpe, H. J.; Oettel, M.; Opletal, G.; Snook, I. Precursor-Mediated Crystallization Process in Suspensions of Hard Spheres. *Phys. Rev. Lett.* **2010**, *105* (2), 025701. https://doi.org/10.1103/PhysRevLett.105.025701.

(44) Dove, P. M.; Han, N.; De Yoreo, J. J. Mechanisms of Classical Crystal Growth Theory Explain Quartz and Silicate Dissolution Behavior. *Proc. Natl. Acad. Sci.* **2005**, *102* (43).

(45) Shon, J. K.; Yuan, X. D.; Ko, C. H.; Lee, H. I.; Thakur, S. S.; Kang, M.; Kang, M. S.; Li, D. J.; Kim, J. N.; Kim, M. J. . No. *J. Ind. Eng. Chem.* **2007**, *13*, 1201–1207.

(46) Wu, H.; Zou, M.; Guo, L.; Ma, F.; Mo, W.; Yu, Y. Effects of Calcination Temperatures on the Structure–Activity Relationship of Ni–La/Al2O3 Catalysts for Syngas Methanation. *RSC Adv.* **2020**, *10*, 4166–4174. https://doi.org/10.1039/c9ra09674d.

(47) Jagadeesan, D.; Vernekar, D.; Gupta, S.; Jaiswal, G. New Opportunities in Heterogeneous Catalysis. *Proc. Indian Natl. Sci. Acad.* **2019**, *85* (1), 23–41. https://doi.org/10.16943/PTINSA/2018/49504.

(48) Ertl, G.; Knözinger, H.; Weitkamp, J. *Handbook of Heterogeneous Catalysis*; Wiley-VCH Verlag GmbH, 2008; Vol. 1–5. https://doi.org/10.1002/9783527619474.FMATTER.

(49) Sanati, M.; Hornell, C.; Jaras, S. G. The Oligomerization of Alkenes by Heterogeneous

Catalysts. *ChemInform* **1999**, *30* (44), no-no. https://doi.org/10.1002/CHIN.199944327.

(50) Zheng, A.; Huang, S. J.; Liu, S. Bin; Deng, F. Acid Properties of Solid Acid Catalysts Characterized by Solid-State 31P NMR of Adsorbed Phosphorous Probe Molecules. *Phys. Chem. Chem. Phys.* **2011**, *13* (33), 14889–14901. https://doi.org/10.1039/c1cp20417c.

(51) Coelho, A.; Caeiro, G.; Lemos, M. A. N. D. A.; Lemos, F.; Ribeiro, F. R. 1-Butene Oligomerization over ZSM-5 Zeolite : Part 1 – Effect of Reaction Conditions. *Fuel* **2013**, *111*, 449–460. https://doi.org/10.1016/j.fuel.2013.03.066.

(52) Al-Kinany, M. C.; Al-Drees, S. A.; Al -Megren, H. A.; Alshihri, S. M.; Alghilan, E. A.; Al-Shehri, F. A.; Al-Hamdan, A. S.; Alghamdi, A. J.; Al-Dress, S. D. High-Quality Fuel Distillates Produced from Oligomerization of Light Olefin over Supported Phosphoric Acid on H-Zeolite-Y. *Appl. Petrochemical Res.* **2019**. https://doi.org/10.1007/s13203-019-0225-1.

(53) Clark, M. C.; Subramaniam, B. Extended Alkylate Production Activity during Fixed-Bed Supercritical 1-Butene/Isobutane Alkylation on Solid Acid Catalysts Using Carbon Dioxide as a Diluent. *Ind. Eng. Chem. Res.* **1998**, *37* (4), 1243–1250. https://doi.org/10.1021/ie970513n.

(54) Wilson, K.; Clark, J. H. Solid Acids and Their Use as Environmentally Friendly Catalysts in Organic Synthesis. *Pure Appl. Chem* **2000**, *72* (7), 1313–1319.

(55) Hattori, H. Solid Acid Catalysts: Roles in Chemical Industries and New Concepts. In *Topics in Catalysis*; Kluwer Academic Publishers, 2010; Vol. 53, pp 432–438. https://doi.org/10.1007/s11244-010-9469-9.

(56) Bellière, V.; Lorentz, C.; Geantet, C.; Yoshimura, Y.; Laurenti, D.; Vrinat, M. Kinetics and Mechanism of Liquid-Phase Alkylation of 3-Methylthiophene with 2-Methyl-2-Butene over a Solid Phosphoric Acid. *Appl. Catal. B Environ.* **2006**, *64* (3–4), 254–261. https://doi.org/10.1016/j.apcatb.2005.11.011.

(57) Dry, M. E. Present and Future Applications of the Fischer-Tropsch Process. *Applied Catalysis A: General*. 2004. https://doi.org/10.1016/j.apcata.2004.08.014.

(58) Khabbouchi, M.; Hosni, K.; Mezni, M.; Srasra, E. Simplified Synthesis of Silicophosphate Materials Using an Activated Metakaolin as a Natural Source of Active Silica. *Appl. Clay Sci.* **2018**, *158*, 169–176. https://doi.org/10.1016/j.clay.2018.03.027.

(59) Kamatani, A. Studies on the Dissolution of Diatomaceous Silica as a Function of Heating. *J. Oceanogr. Soc. Japan* **1974**, *30* (4), 157–162. https://doi.org/10.1007/BF02111066.

(60) Freund, H. J. The Surface Science of Catalysis and More, Using Ultrathin Oxide Films as Templates: A Perspective. *J. Am. Chem. Soc.* **2016**, *138* (29), 8985–8996. https://doi.org/10.1021/jacs.6b05565.

(61) Hocking, M. B. Phosphorus and Phosphoric Acid. In *Handbook of Chemical Technology and Pollution Control*; Elsevier, 2005; pp 289–320. https://doi.org/10.1016/b978-012088796-5/50013-2.

(62) Spainhour, C. B. Phosphoric Acid. In *Encyclopedia of Toxicology: Third Edition*; 2014. https://doi.org/10.1016/B978-0-12-386454-3.00904-0.

(63) Ma, H.; Feng, X.; Deng, C. Water-Phosphorus Nexus for Wet-Process Phosphoric Acid Production. *Ind. Eng. Chem. Res.* **2018**, *57* (20), 6968–6979. https://doi.org/10.1021/acs.iecr.7b05399.

(64) Rahman, A.; Lin, X. Biomolecular Chemistry Phosphoric Acids in Asymmetric Catalysis. *Org. Biomol. Chem.* **2018**, *16*, 4753–4777. https://doi.org/10.1039/c8ob00900g.

(65) Gilmour, R. Polyphosphoric Acid. In *Phosphoric Acid*; 2013. https://doi.org/10.1201/b16187-4.

(66) Platonov, V. A. Properties of Polyphosphoric Acid. *Fibre Chem.* **2000**. https://doi.org/10.1007/BF02360636.

(67) Zhang, J.; Lin, S.-X.; Cheng, D.-J.; Liu, X.-Y.; Tan, B. Phosphoric Acid-Catalyzed Asymmetric Classic Passerini Reaction. *J. Am. Chem. Soc.* **2015**, *137* (44), 14039–14042. https://doi.org/10.1021/JACS.5B09117.

(68) Huhti, A.-L.; Gartaganis, P. A. The Composition of the Strong Phosphoric Acids. *Can. J.*

Chem. **1956**. https://doi.org/10.1139/v56-102.

(69) Jameson, R. F. The Composition of the Strong Phosphoric Acids. *J. Chem. Soc.* **1959**, No. 752.

(70) Ross, W. H.; Durgin, C. B.; Jones, R. M. The Composition of Commercial Phosphoric Acid. *J. Ind. Eng. Chem.* **2002**, *14* (6), 533–535. https://doi.org/10.1021/IE50150A027.

(71) Jameson, R. F. The Composition of the 'Strong' Phosphoric Acids. *J. Chem. Soc.* **1959**. https://doi.org/10.1039/JR9590000752.

(72) Bell, R. N. Composition of Strong Phosphoric Acids. *Ind. Eng. Chem.* **2002**, *40* (8), 1464–1467. https://doi.org/10.1021/IE50464A027.

(73) Davis, B. H.; Ertl, G.; Knozinger, H.; Schuth, F.; Weitkamp, J. Eter. In *Handbook of Heterogeneous Catalysis*; 2008.

(74) Morris, R. A.; Knighton, W. B.; Viggiano, A. A.; Hoffman, B. C.; Schaefer, H. F. The Gas-Phase Acidity of H3PO4. *J. Chem. Phys.* **1997**, *106* (9), 3545–3547. https://doi.org/10.1063/1.473465.

(75) Munson, R. . N. *J. Phys.Chem* **1964**, *68*, 3374.

(76) Devedjiev, I. A Novel Method for the Synthesis of Acetyl Phosphate. *Phosphorus, Sulfur Silicon Relat. Elem.* **2006**, *181* (8), 1785–1787. https://doi.org/10.1080/10426500500536598.

(77) Munson, R. . N. *J. Phys.Chem* **1965**, *69*, 1761.

(78) Styskalik, A.; Skoda, D.; Moravec, Z.; Roupcova, P.; Barnes, E.; Pinkas, J. Non-Aqueous Template-Assisted Synthesis of Mesoporous Nanocrystalline Silicon Orthophosphate. *RSV Adv.* **2015**, *5*, 73670–73676. https://doi.org/10.1039/c5ra10982e.

(79) Liebau, F.; Bissert, G.; Köppen, N. Synthese Und Kristallographische Eigenschaften Einiger Phasen Im System SiO2–P2O5. *ZAAC - J. Inorg. Gen. Chem.* **1968**, *359* (3–4), 113–134. https://doi.org/10.1002/zaac.19683590302.

(80) Leinenweber, K.; Stearns, L. A.; Nite, J. M.; Németh, P.; Groy, T. L. Structure of a New Form of Silicon Phosphate (SiP 2O 7) Synthesized at High Pressures and Temperatures. *J. Solid State Chem.* **2012**, *190*, 221–225. https://doi.org/10.1016/j.jssc.2012.02.031.

(81) Bettermann, P.; Liebau, F. The Transformation of Amorphous Silica to Crystalline Silica under Hydrothermal Conditions. *Contrib. to Mineral. Petrol.* **1975**, *53* (1), 25–36. https://doi.org/10.1007/BF00402452.

(82) Stearns, L. A.; Groy, T. L.; Leinenweber, K. High-Pressure Synthesis and Crystal Structure of Silicon Phosphate Hydroxide, SiPO4(OH). *J. Solid State Chem.* **2005**, *178* (9), 2594–2601. https://doi.org/10.1016/j.jssc.2005.05.030.

(83) Norouzi, H. R.; Fatemi, S. Economic Optimization of the Cumene Production Process Using Response Surface Methodology. *Chem. Eng. Commun.* **2012**, *199* (11), 1375–1393. https://doi.org/10.1080/00986445.2012.660895.

(84) Fernández-Lorenzo, C.; Esquivias, L.; Barboux, P.; Maquet, J.; Taulelle, F. Sol-Gel Synthesis of SiO2P2O5 Glasses. *J. Non. Cryst. Solids* **1994**, *176* (2–3), 189–199. https://doi.org/10.1016/0022-3093(94)90077-9.

(85) Marchionna, M.; Di Girolamo, M.; Patrini, R. Light Olefins Dimerization to High Quality Gasoline Components. *Catal. Today* **2001**, *65* (2–4), 397–403. https://doi.org/10.1016/S0920-5861(00)00587-3.

(86) Schwarzer, R.; du Toit, E.; Nicol, W. Solid Phosphoric Acid Catalysts: The Effect of Free Acid Composition on Selectivity and Activity for 1-Hexene Dimerisation. *Appl. Catal. A Gen.* **2009**, *369* (1–2), 83–89. https://doi.org/10.1016/j.apcata.2009.09.002.

(87) Goren, R.; Baykara, T.; Marsoglu, M. Effects of Purification and Heat Treatment on Pore Structure and Composition of Diatomite. *Br. Ceram. Trans.* **2002**, *101* (4), 177–180. https://doi.org/10.1179/096797802225003361.

(88) Khraisheh, M. A. M.; Al-Ghouti, M. A.; Allen, S. J.; Ahmad, M. N. Effect of OH and Silanol Groups in the Removal of Dyes from Aqueous Solution Using Diatomite. *Water Res.* **2005**,

39 (5), 922–932. https://doi.org/10.1016/j.watres.2004.12.008.

(89) Wang, R.; Li, Y. Preparation of MCM-41 Supported Phosphoric Acid Catalyst for Thiophenic Compounds Alkylation in FCC Gasoline. *Catal. Commun.* **2010**, *11* (8), 705–709. https://doi.org/10.1016/j.catcom.2010.01.025.

(90) Kotsarenko, N. S.; Shmachkova, V. P.; Mudrakovskii, I. L.; Mastikhin, V. M. Investigation of the Interaction of Phosphoric Acid with Silica Gel by High-Resolution Solid-State /Sup 31/P and /Sup 29/Si NMR. Kinet. Catal. (Engl. Transl.); (United States). 29:1. *Kinet Catal* **1989**, *30* (974).

(91) Grünert, A.; Schmidt, W.; Schüth, F. Carbon Supported Phosphoric Acid Catalysts for Gas-Phase Synthesis of Diesel Additives. *Catal. Lett. 2020 15010* **2020**, *150* (10), 2951–2958. https://doi.org/10.1007/S10562-020-03200-4.

(92) Krawietz, T. R.; Lin, P.; Lotterhos, K. E.; Torres, P. D.; Barich, D. H.; Clearfield, A.; Haw, J. F. Solid Phosphoric Acid Catalyst: A Multinuclear NMR and Theoretical Study. *J. Am. Chem. Soc.* **1998**, *120* (33), 8502–8511. https://doi.org/10.1021/ja9813461.

(93) Haake, P. C.; Westheimer, F. H. Hydrolysis and Exchange in Esters of Phosphoric Acid1a,B. *J. Am. Chem. Soc.* **2002**, *83* (5), 1102–1109. https://doi.org/10.1021/JA01466A025.

(94) Ramis, G.; Rossi, P. F.; Busca, G.; Lorenzelli, V.; Chimica, I.; Ingegneria, F.; Kennedy, P.; Chimica, D.; La, R.; Moro, P. A.; Patrono, P.; Avánzate, M.; Ricerca, A.; Roma, M. S. Phosphoric Acid Oxide Carriers . 2 . Surface Acidity and Reactivity toward Olefins. *Langmuir* **1989**, No. 8, 917–923.

(95) Coster, D.; Blumenfeld, A. L.; Fripiat, J. J. Lewis Acid Sites and Surface Aluminum in Aluminas and Zeolites: A High-Resolution NMR Study. *J. Phys. Chem.* **1994**, *98* (24), 6201–6211. https://doi.org/10.1021/j100075a024.

(96) Shin, E. W.; Han, J. S.; Jang, M.; Min, S. H.; Park, J. K.; Rowell, R. M. Phosphate Adsorption on Aluminum-Impregnated Mesoporous Silicates: Surface Structure and Behavior of Adsorbents. *Environ. Sci. Technol.* **2004**, *38* (3), 912–917.

https://doi.org/10.1021/es030488e.

(97) Bothe, J. V.; Brown, P. W. Reactivity of Alumina toward Phosphoric Acid. *J. Am. Ceram. Soc.* **1993**, *76* (9), 2353–2358. https://doi.org/10.1111/j.1151-2916.1993.tb07776.x.

(98) Fougret, C. M.; Atkins, M. P.; Hölderich, W. F. Influence of the Carrier on the Catalytic Performance of Impregnated Phosphoric Acid in the Hydration of Ethylene. *Appl. Catal. A Gen.* **1999**. https://doi.org/10.1016/S0926-860X(98)00416-5.

(99) Satterfield; N, C. Heterogeneous Catalysis in Industrial Practice. 2nd Edition. New York, NY (United States); McGraw Hill Book Co. January 1, 1991.

(100) Jabri, M.; Mejdoubi, E.; El Gadi, M.; Hammouti, B. Optimisation of Hardness and Setting Time of Dental Zinc Phosphate Cement Using a Design of Experiments. *Arab. J. Chem.* **2012**, *5* (3), 347–351. https://doi.org/10.1016/J.ARABJC.2010.09.004.

(101) Freund, H.-J. Model Studies in Heterogeneous Catalysis. *Chem. - A Eur. J.* **2010**, *16* (31), 9384–9397. https://doi.org/10.1002/chem.201001724.

(102) Hutchings, G. J. Vanadium Phosphate: A New Look at the Active Components of Catalysts for the Oxidation of Butane to Maleic Anhydride. *Journal of Materials Chemistry*. 2004. https://doi.org/10.1039/b404610m.

(103) Guliants, V. V.; Benziger, J. B.; Sundaresan, S.; Wachs, I. E.; Jehng, J. M.; Roberts, J. E. The Effect of the Phase Composition of Model VPO Catalysts for Partial Oxidation of N-Butane. *Catal. Today* **1996**. https://doi.org/10.1016/S0920-5861(96)00043-0.

(104) Wen-Sheng Dong; Jonathan K. Bartley; Nian-Xue Song, and; Hutchings, G. J. Synthesis and Characterization of Vanadyl Hydrogen Phosphite Hydrate. *Chem. Mater.* **2005**, *17* (10), 2757–2764. https://doi.org/10.1021/CM0477568.

(105) Cavani, F.; Trifirò, F. The Characterization of the Surface Properties of V-P-O-Based Catalysts by Probe Molecules. *Appl. Catal. A Gen.* **1997**. https://doi.org/10.1016/S0926-860X(97)00052-5.

(106) Nguyen, P. T.; Hoffman, R. D.; Sleight, A. W. Structure of (VO)2P2O7. *Mater. Res. Bull.*

1995. https://doi.org/10.1016/0025-5408(95)00116-6.

(107) Wang, F.; Dubois, J. L.; Ueda, W. Catalytic Performance of Vanadium Pyrophosphate Oxides (VPO) in the Oxidative Dehydration of Glycerol. *Appl. Catal. A Gen.* **2010**. https://doi.org/10.1016/j.apcata.2009.11.031.

(108) Liu, Q.; Liu, W.; Lü, L.; Li, R.; Liang, B.; Yue, H.; Tang, S.; Li, C. Study on Reactions of Gaseous P2O5 with Ca3(PO4)2 and SiO2 during a Rotary Kiln Process for Phosphoric Acid Production. *Chinese J. Chem. Eng.* **2018**, *26* (4), 795–805. https://doi.org/10.1016/j.cjche.2017.11.016.

(109) Xie, Z.; Liu, Z.; Wang, Y.; Yang, Q.; Xu, L.; Ding, W. An Overview of Recent Development in Composite Catalysts from Porous Materials for Various Reactions and Processes. *Int. J. Mol. Sci.* **2010**, *11* (5), 2152. https://doi.org/10.3390/IJMS11052152.

(110) Taufiq-Yap, Y. H.; Joshua Hoh, R.; Wong, Y. C. Synthesis of Nanostructured Vanadium Phosphate Catalysts Using Sonochemical Route for Partial Oxidation of N-Butane. *J. Appl. Sci.* **2011**, *11* (13), 2370–2375. https://doi.org/10.3923/JAS.2011.2370.2375.

(111) Strempel, V. E.; Löffler, D.; Kröhnert, J.; Skorupska, K.; Johnson, B.; d'Alnoncourt, R. N.; Driess, M.; Rosowski, F. Enhancing of Catalytic Properties of Vanadia via Surface Doping with Phosphorus Using Atomic Layer Deposition. *J. Vac. Sci. Technol. A Vacuum, Surfaces, Film.* **2016**. https://doi.org/10.1116/1.4936390.

(112) da Silva, L. M.; de Oliveira Santiago Santos, G.; de Salles Pupo, M. M.; Eguiluz, K. I. B.; Salazar-Banda, G. R. Influence of Heating Rate on the Physical and Electrochemical Properties of Mixed Metal Oxides Anodes Synthesized by Thermal Decomposition Method Applying an Ionic Liquid. *J. Electroanal. Chem.* **2018**, *813*, 127–133. https://doi.org/10.1016/j.jelechem.2018.02.026.

(113) Poojary, D. M.; Borade, R. B.; Clearfield, A. Structural Characterization of Silicon Orthophosphate. *Inorganica Chim. Acta* **1993**, *208* (1), 23–29. https://doi.org/10.1016/S0020-1693(00)82879-0.

(114) Ercan, C.; Dautzenberg, F. M.; Yeh, C. Y.; Barner, H. E. Mass-Transfer Effects in Liquid-Phase Alkylation of Benzene with Zeolite Catalysts. *Ind. Eng. Chem. Res.* **1998**. https://doi.org/10.1021/ie970797b.

(115) Wei, P. S.; Hsiao, S. Y. Effects of Mass Transfer Coefficient on Pore Shape in Solid. *Int. J. Heat Mass Transf.* **2016**, *103*, 931–939. https://doi.org/10.1016/J.IJHEATMASSTRANSFER.2016.07.081.

(116) Shcherban, N. D.; Filonenko, S. M.; Yaremov, P. S.; Nauky, P. Micro-Mesoporous Zeolite-like Matrices. **2017**, *52* (6), 356–361. https://doi.org/10.1007/s11237-017-9490-1.

(117) Jimeńez-García, G.; De Lasa, H.; Quintana-Solorźano, R.; Maya-Yescas, R. Catalyst Activity Decay Due to Pore Blockage during Catalytic Cracking of Hydrocarbons. *Fuel* **2013**, *110*, 89–98. https://doi.org/10.1016/j.fuel.2012.10.082.

(118) Shaji, A.; Zachariah, A. K. Surface Area Analysis of Nanomaterials. In *Thermal and Rheological Measurement Techniques for Nanomaterials Characterization*; 2017. https://doi.org/10.1016/B978-0-323-46139-9.00009-8.

(119) Xie, W.; Liang, D.; Li, L.; Qu, S.; Tao, W. Surface Chemical Properties and Pore Structure of the Activated Coke and Their Effects on the Denitrification Activity of Selective Catalytic Reduction. *Int. J. Coal Sci. Technol.* **2019**, *6* (4), 595–602. https://doi.org/10.1007/s40789-019-00267-2.

(120) Beeckman, J. W.; Froment, G. F. Catalyst Deactivation by Active Site Coverage and Pore Blockage. *Ind. Eng. Chem. Fundam.* **1979**, *18* (3), 245–256. https://doi.org/10.1021/i160071a009.

(121) Wu, D. F.; Zhou, J. C.; Y., and Y. D. L. Distribution of the Mechanical Strength of Solid Catalysts. *Chem. Eng. Res. Des.* **2006**, *84*, 1152–1157.

(122) Valverde, J. M.; Medina, S. Limestone Calcination under Calcium-Looping Conditions for CO2 Capture and Thermochemical Energy Storage in the Presence of H2O: An in Situ XRD Analysis. *Phys. Chem. Chem. Phys.* **2017**, *19* (11), 7587–7596.

https://doi.org/10.1039/c7cp00260b.

(123) Su, B. L.; Sanchez, C.; Yang, X. Y. Hierarchically Structured Porous Material from Nanoscience to Catalysis, Separation, Optics, Energy and Life Science. *Wiley-VCH* No. 2012.

(124) Sakuneka, T. M.; Nel, R. J. J.; Klerk, A. de. Benzene Reduction by Alkylation in a Solid Phosphoric Acid Catalyzed Olefin Oligomerization Process. *Ind. Eng. Chem. Res.* **2008**, *47* (19), 7178–7183. https://doi.org/10.1021/IE800672P.

(125) De Klerk, A.; Leckel, D. O.; Prinsloo, N. M. Butene Oligomerization by Phosphoric Acid Catalysis: Separating the Effects of Temperature and Catalyst Hydration on Product Selectivity. *Ind. Eng. Chem. Res.* **2006**. https://doi.org/10.1021/ie060207m.

(126) De Klerk, A. Oligomerization of 1-Hexene and 1-Octene over Solid Acid Catalysts. *Ind. Eng. Chem. Res.* **2005**. https://doi.org/10.1021/ie0487843.

(127) Bertolacini, R. J.; Bradley, A.; Gattuso, J. Characterization and Catalyst Development. *ACS Sustain. Chem. Eng.* **1989**, No. 380.

(128) Fougret, C. M.; Hölderich, W. F. Ethylene Hydration over Metal Phosphates Impregnated with Phosphoric Acid. *Appl. Catal. A Gen.* **2001**, *207* (1–2), 295–301. https://doi.org/10.1016/S0926-860X(00)00666-9.

(129) Cavani, F.; Girotti, G.; Terzoni, G. Effect of Water in the Performance of the 'Solid Phosphoric Acid' Catalyst for Alkylation of Benzene to Cumene and for Oligomerization of Propene. *Appl. Catal. A, Gen.* **1993**. https://doi.org/10.1016/0926-860X(93)80083-3.

(130) Solovyov, L. A. Diffraction Analysis of Mesostructured Mesoporous Materials. *Chem. Soc. Rev* **2013**, *42* (3708). https://doi.org/10.1039/c2cs35248f.

(131) Stanjek, H.; Häusler, W. Basics of X-Ray Diffraction. *Hyperfine Interact. 2004 1541* **2004**, *154* (1), 107–119. https://doi.org/10.1023/B:HYPE.0000032028.60546.38.

(132) Hammond, C. The Basics of Crystallography and Diffraction (2nd Edn). *Meas. Sci. Technol.* **2002**, *13* (2), 232. https://doi.org/10.1088/0957-0233/13/2/708.

(133) Mittemeijer, E. J.; Welzel, U. The 'State of the Art' of the Diffraction Analysis of Crystallite Size and Lattice Strain. *Zeitschrift fur Krist.* **2008**, *223* (9), 552–560. https://doi.org/10.1524/ZKRI.2008.1213.

(134) Niemantsverdriet, J. W. Spectroscopy in Catalysis: An Introduction, Third Edition. *WILEY-VCH Verlag GmbH Co. KGaA, Weinheim* **2007**, *8*, 148–152.

(135) Fewster, P. F. Estimating the Structure Factors in X-Ray Diffraction. *Acta Crystallogr. Sect. A Found. Adv.* **2018**, *74* (5), 481–498. https://doi.org/10.1107/S2053273318007593.

(136) Thomas, J. . M.; Thomas, W. J. Principles and Practice of Heterogeneous Catalysis, Second, Revised Edition 2015. *Wiley-VCH Verlag GmbH Co. KGaA, Boschstr. 12, 69469 Weinheim, Ger.* **2015**.

(137) Pope, C. G. X-Ray Diffraction and the Bragg Equation. *J. Chem. Educ.* **1997**, *74* (1), 129–131. https://doi.org/10.1021/ed074p129.

(138) Renouprez, A. J. Catalyst Characterization – Physical Techniques for Solid Materials (Eds. B. Imelik and J.C. V_edrine), Plenum Press, New York,. **1994**.

(139) Monshi, A.; Foroughi, M. R.; Monshi, M. R. Modified Scherrer Equation to Estimate More Accurately Nano-Crystallite Size Using XRD. *World J. Nano Sci. Eng.* **2012**, *02* (03), 154–160. https://doi.org/10.4236/wjnse.2012.23020.

(140) Nagayama, K.; Danev, R. Phase Contrast Electron Microscopy: Development of Thin-Film Phase Plates and Biological Applications. *Philosophical Transactions of the Royal Society B: Biological Sciences*. Royal Society June 27, 2008, pp 2153–2162. https://doi.org/10.1098/rstb.2008.2268.

(141) Egerton, R. F.; Li, P.; Malac, M. Radiation Damage in the TEM and SEM. In *Micron*; 2004; Vol. 35, pp 399–409. https://doi.org/10.1016/j.micron.2004.02.003.

(142) Abellan, P.; Woehl, T. J.; Parent, L. R.; Browning, N. D.; Evans, J. E.; Arslan, I. Factors Influencing Quantitative Liquid (Scanning) Transmission Electron Microscopy. *Chem. Commun.* **2014**, *50* (38), 4873–4880. https://doi.org/10.1039/c3cc48479c.

(143) Zhou, W.; Greer, H. F. What Can Electron Microscopy Tell Us Beyond Crystal Structures? *Eur. J. Inorg. Chem.* **2016**, *2016* (7), 941–950. https://doi.org/10.1002/ejic.201501342.

Chapter 2

2 Experimental methods.

2.1 Effect of synthesis conditions on physical and chemical properties of SPA catalysts.

The chemical and physical characteristics of a catalyst are greatly influenced by synthesis conditions. These catalyst parameters include crushing strength, specific surface area, pore volume and morphology of the catalyst[1]. The mechanical crushing strength of the catalyst is essential for the efficient operation of the chemical reactor. A solid catalyst with high crushing strength has low attrition resulting in longer catalyst life compared to a catalyst with low crushing strength[2]. However, catalyst attrition and hardness are interrelated, more so, they are both influenced by synthesis conditions.

Uncontrolled synthesis conditions such as the calcination temperature of the solid catalyst can result in the formation of microcracks in extrudates or pellets. The void space formed lowers catalyst mechanical hardness even though it is beneficial to mass diffusion[3]. The catalysts micropores or micro-void spaces influence the specific surface area which is defined as a total surface area of microporous material per unit mass[4]. These pores can restrict the rate of conversion of reactants to products by impeding the diffusion of reactants and products. However, the formation of microcracks and other unwanted void spaces could be reduced by controlling the drying rate of the synthesized catalyst[5].

Controlling the calcination conditions can only be beneficial if the appropriate synthesis method has been used to synthesize the catalyst. Various synthetic methods such as chemical vapour deposition, hydrolytic, sol-gel techniques and impregnation technique can be used for the synthesis of the SPA catalysts[6]. Styskalik et al., used non-hydrolytic polycondensation template-assisted synthesis to synthesize $Si_5P_6O_{25}$. The drawback of their method was that it uses non environmentally friendly reagents such as toluene[7]. Leinenweber et al., used high pressure and high-temperature synthesis technique to synthesize SiP_2O_7[8]. The challenges with their method are the synthesis conditions used are not economically sustainable. Furthermore, there is no control over the polymorph of the SiP_2O_7 phase in the catalyst synthesized. In addition to that,

Khabbouchi et al., has synthesized both silicon orthophosphate and silicon pyrophosphate phases using acid-activated clay. Their synthetic method does not foster homogeneous dispersion of silicon and phosphorus atoms on the SPA catalyst[6].

In this work, SPA catalysts were synthesized using the impregnation method due to their versatility. This method allows manipulation of silicon to phosphorus ratios from as low as 0.5 to as high as 5 Si/P ratio during synthesis[9]. A reason that gives control to the development of a catalyst of optimum silicon to phosphorus ratio. Silicon and phosphorus in the SPA catalyst form the basis of the catalyst[10]. Therefore, the relationship between these two atoms must be at the optimum for optimized SPA catalyst structure. The synthesized catalyst was then modified by heat treatment in a calciner to institute morphological changes such as crystallization and oxidation[11].

2.2 Influence of the concentration of ancillary minerals in kieselguhr on SPA catalysts physical and chemical properties.

The major raw materials used in this work for the synthesis of solid phosphoric acid catalysts are phosphoric acid and kieselguhr. In kieselguhr, there is a variable amount of ancillary compounds such as metal oxides, clays and salts albeit in low concentrations[12]. The quantities of these other compounds in kieselguhr are influenced by the geological source[13]. In some cases, these elements are incorporated into the crystal structure of the silica polymorph which can cause changes in the physical parameters of the kieselguhr material after its reaction with acid[14]. Wang et al., reported an increase in the diameter of macropores of the kieselguhr from a range of 1.3 µm - 2.8 µm to a range of 2.8 µm – 7.5 µm after acid treatment of the kieselguhr material[15]. The author said, “there is a decrease in macropore area, the pore volume, and the percentage of capillary pore after kieselguhr treatment with acid”.

SPA catalyst synthesis involves the treatment of kieselguhr with phosphoric acid, understanding the characteristics of kieselguhr after treatment with acids provides invaluable information for the evaluation of the effect of synthetic kieselguhr on SPA catalyst structure. On this account, the variation in the morphological properties of kieselguhr from different geological sources suggests that changing the type of kieselguhr for SPA catalyst synthesis can result in catalyst

morphological changes. These changes can be beneficial or detrimental to the SPA catalyst structure. Beneficial if we change the kieselguhr support and get improved SPA catalyst hardness strength without significantly compromising porosity and detrimental if changing the kieselguhr lowers the crystallinity and free acid.

2.2.1 Differences and similarities in crystalline phases of the kieselguhr used in this work.

To fully comprehend the effect of kieselguhr support on SPA catalyst, a study of the variation in properties of the two different kieselguhr used in this work was carried out. The mined kieselguhr with a SiO_2 assay of 94.5 % was purchased from Eagle Peacher and dried to drive out volatiles then used without further processing. The synthetic kieselguhr with a SiO_2 assay of 89.1 % was purchased from Eagle Peacher and calcined at 700 ^oC for 24 hours to initiate the formation of the cristobalite phase and used without further processing[16].

The crystalline and amorphous phases of the synthetic and mined kieselguhr catalyst support were investigated using the XRD technique[17]. Figure 2.1 below, shows the diffraction patterns of the two kieselguhr types that were here used to synthesize the SPA catalysts.

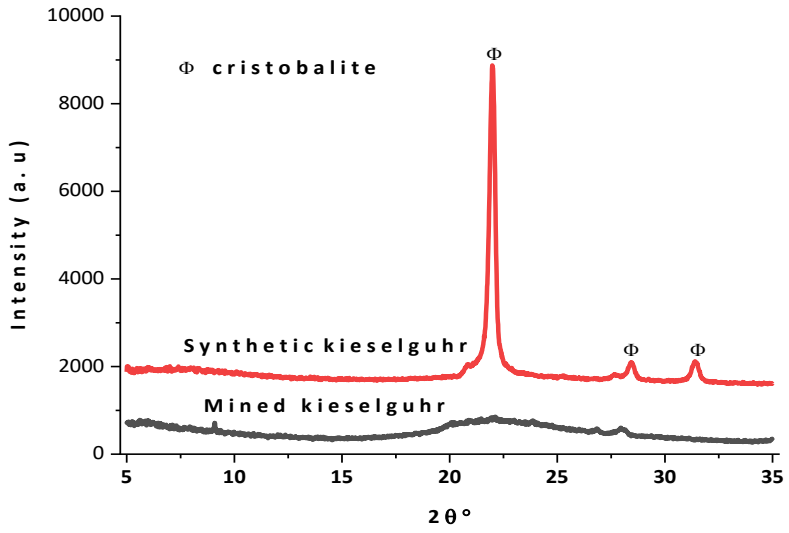


Figure 2.1 PXRD diffractogram of synthetic kieselguhr(red graph with distinct peaks that shows that it is crystalline with α-cristobalite silica phase) and mined kieselguhr (black broadened graph showing that the material is amorphous)[18].

The crystallinity differences between synthetic and mined kieselguhr show a definite difference in the crystallinity of the support material. Such a variation can influence the SPA catalyst pore volume. More so, the pore volume and pore structure of the catalyst is directly proportional to the particle size of the support material. Here below, the particle diameter of the kieselguhr used in this work was investigated.

2.2.2 Influence of particle size of the kieselguhr support material on SPA catalysts porosity.

The support with large particle size foster the synthesis of a catalyst with high porosity due to poor agglomeration of particles, the opposite is true for the support with fine particles[19]. To that end, the Laser light scattering particle diameter of the mined and synthetic kieselguhr was investigated. A sample of each 5 g kieselguhr was loaded into the instrument which uses water as a wet dispersion medium[20]. Inside the instrument (Micromeritics Saturn DigiSizer II 5205 V1.04 particle Analyzer instrument), the sample was homogenized and dispersed, these dispersed particles scatter a beam of Laser light at different angles corresponding to the particle sizes[21]. The intensity data was transferred to the software which uses the Mie equation to calculate the particle size based on the angle of light scattered, the measurement results are given as volume-weighted particle size distribution[22,23].

Table 2.1 Percentile by volume particle size distribution of synthetic and mined kieselguhr.

Percent finer	Particle diameter (μm)	
	Synthetic kieselguhr	Mined kieselguhr
100	345 ± 2	325 ± 2
99.0	302 ± 2	293 ± 2
90.0	235 ± 2	123 ± 2
50.0	54 ± 2	18 ± 2
10.0	147 ± 2	6 ± 2

Data from Table 2.1 above shows that synthetic kieselguhr has a bigger particle diameter compared to amorphous mined kieselguhr. 50 % of the particles from synthetic kieselguhr have a particle diameter of 54 µm and below, the same percentile in mined kieselguhr has a particle diameter of 18 µm which means that at 50 % synthetic kieselguhr have bigger particles relative to mined kieselguhr by more than two times. The hypothesis is what is the impact of variation in kieselguhr grain size on the mass transfer coefficient of the SPA catalyst and its mechanical hardness?

2.2.3 Variation in surface area of the synthetic and mined kieselguhr.

The influence of the particle size on kieselguhr BET surface area and adsorption behaviour was investigated using Micromeritics TriStar II 3020 V1.03 (V1.03) instrument and the results are reported in Figure 2.2, 2.3 and Table 2.2 below.

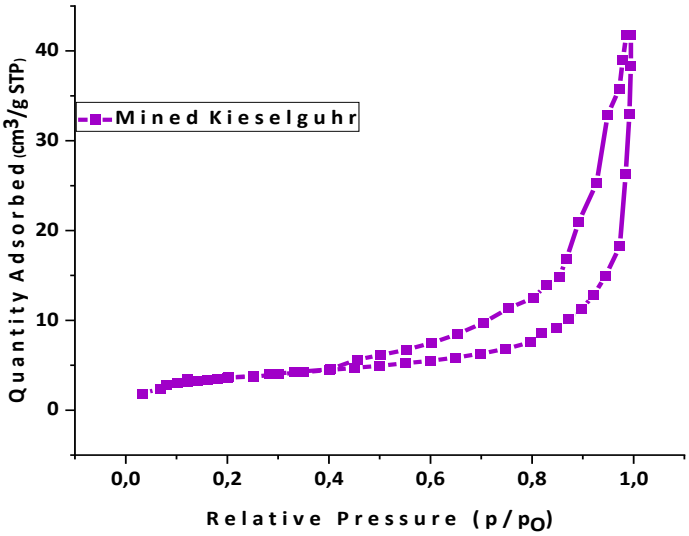


Figure 2.2 Isothermal plot showing the adsorption and desorption behaviour of mined kieselguhr.

The mined kieselguhr has shown a Type IV isotherm with an H3 hysteresis loop for mined kieselguhr. That means the material was characterized by mesopores which are slit-like pores[24].

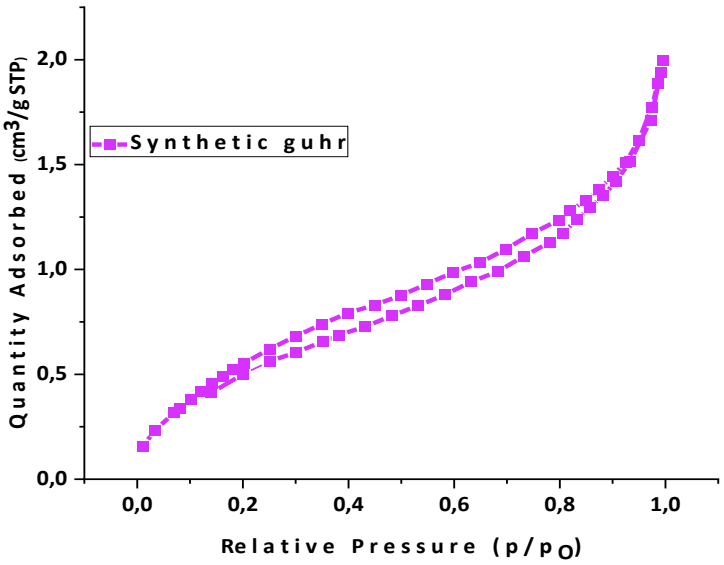


Figure 2.3 Isothermal plot showing the adsorption and desorption behaviour of synthetic kieselguhr.

The isothermal plot of synthetic kieselguhr in Figure 2.3 above has shown a Type IV isotherm with an H1 hysteresis loop for synthetic kieselguhr. That means the material was having mesopores with cylindrical pore geometry and facile pore connectivity[25]. The differences shown in the hysteresis loops of mined and synthetic kieselguhr implies that the two silica sources have different adsorption properties characterized by different pore structures.

Table 2.2 BET surface area of synthetic and mined kieselguhr.

Analysis	Synthetic kieselguhr	Mined kieselguhr
BET Surface area(m^2/g)	2 ± 1	14 ± 1

The BET specific surface area of the two kieselguhr samples Table 2.2 above is in agreement with the particle size results, that is larger particles (synthetic kieselguhr) have lower BET surface area and finer particles (mined kieselguhr) have larger BET surface area. Furthermore,

the BET surface area results agree with PXRD results in Figure 2.1 above, that is crystalline synthetic kieselguhr has a larger particle diameter compared to amorphous mined kieselguhr[26].

2.3 Synthesis of the SPA catalysts.

Traditionally, the SPA catalyst is synthesized in cylindrical extrudates and find its application in fixed bed reactors which can experience pressure drop[27]. The feed material in the reactor is hydrated, the water molecules react with loosely bound free phosphoric acid thereby deforming the solid structure of the SPA catalyst[28]. As such, deformation of extrudates results in a decrease in reactor volume ultimately causing pressure differences which destabilize the steady-state of the reactor causing an untimed reactor shut down[29]. However, extrudates degrade at a very lower rate compared to other shaped SPA catalyst[30].

2.3.1 Objectives.

The main objectives of the experiments conducted in this section were to;

(i) Synthesize cylindrically shaped (unpromoted and calcium promoted) SPA catalyst using H_3PO_4 acid and mined kieselguhr.

(ii) Synthesize quadrilobed shaped (unpromoted and calcium promoted) SPA catalyst using H_3PO_4 and mined kieselguhr.

(iii) Synthesize vanadium promoted SPA catalyst using H_3PO_4 and mined kieselguhr.

(iv) Synthesize cylindrically shaped (unpromoted and calcium promoted) SPA catalyst using H_3PO_4 and synthetic kieselguhr.

Herein, naturally mined and dried kieselguhr was used to synthesize SPAM, SPAMCa, SPAMQ, SPAMQCa and SPAMV catalyst. In addition to that, a new silica source synthetic kieselguhr was used to synthesize SPAS and SPASCa catalyst.

The phosphoric acid used was orthophosphoric acid, a colourless liquid purchased from LABCHEM with an assay of 85 % H_3PO_4, Cl 0.0005 %, NO_3 0.001 %, SO_4 0.003 %, CH_3COOH 0.001 %, As 0.02 % , Fe 0.02 % and reducing substance (H_3PO_3) 0.0025 %.

The synthetic kieselguhr, a white powder with an assay of SiO_2 89.05 %, Al_2O_3 0.81 %, FeO_3 1.5 %, CaO 0.6 %, MgO 0.3 % and loss on ignition 7.74 % purchased from Eagle Pearcher Minerals®.

Mined kieselguhr, a yellow powder with an assay of SiO_2 94.54 %, Al_2O_3 1.01 %, FeO_3 0.89 % CaO 0.5 % and loss on ignition 3.06 % also purchased from Eagle Pearcher Minerals®.

Vanadium pentoxide (yellow powder) had an assay of V_2O_5 99 %, CO_3 0.02 %, Cl 0.006 %, SO_4 0.002 %, Fe 0.01 %, Pb 0.002 % and loss on ignition 0.96 %. The calcium source had an assay of 34 – 40 % calcium basis of $HCa_5O_{13}P_3$ purchased from Sigma Aldrich. Corn-starch (yellow powder) had an assay of 99.9 % $C_{27}H_{48}O_{20}$ purchased from Bunge USA.

2.3.2 SPA catalyst synthesis diagram.

The SPA catalysts were synthesised according to the procedure depicted in the process flow diagram Figure 2.4 below.

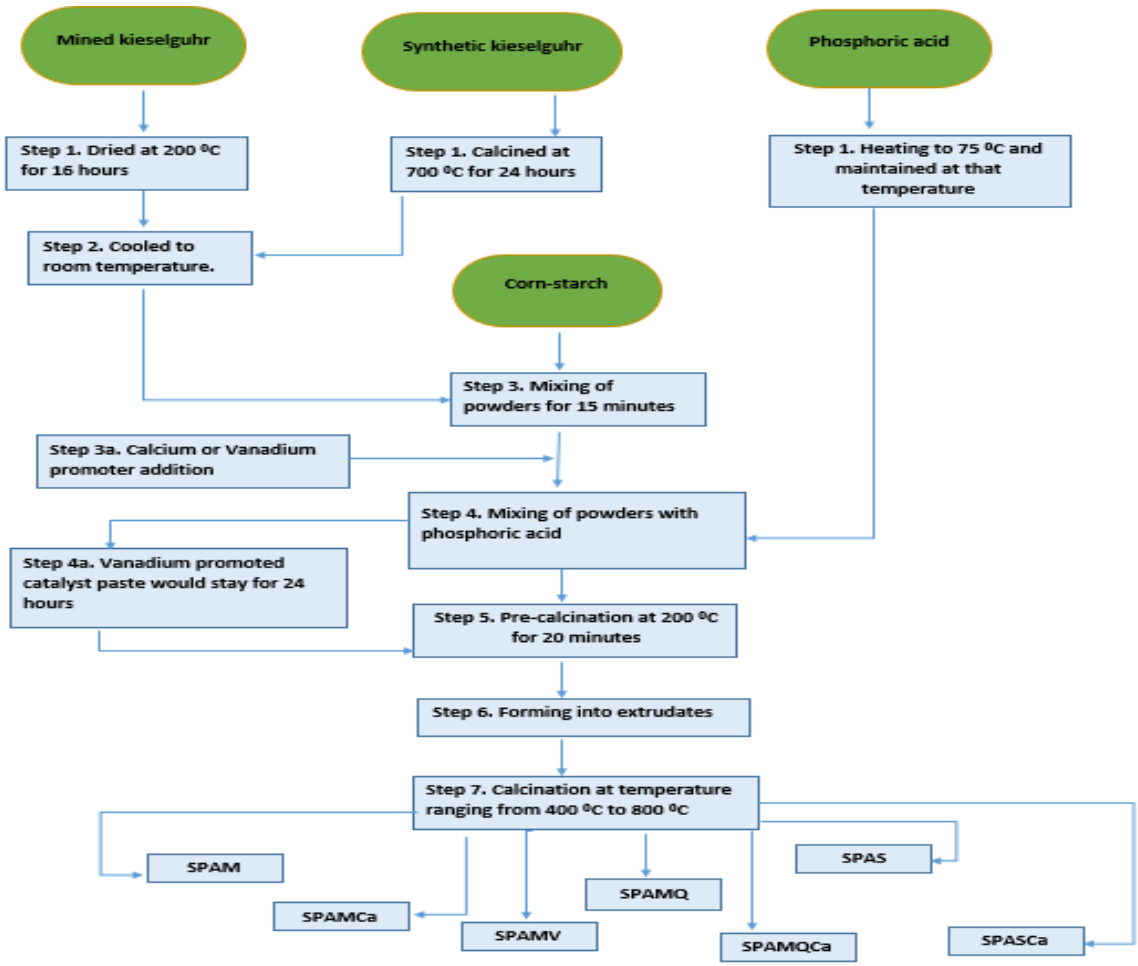


Figure 2.4 Synthesis of SPA catalysts process flow diagram.

2.3.3 Discussion of the synthesis procedure Figure 2.4

Step 1. Naturally mined kieselguhr was placed in an open container, taken to a laboratory furnace heated for 16 hours at 200 ^{o}C to drive out moisture. The synthetic kieselguhr was calcined at 700 ^{o}C for 24 hours to foster the formation of the α-cristobalite phase. The use of crystalline synthetic kieselguhr would enable a comparative study on the effect of amorphous versus crystalline kieselguhr on SPA catalyst structure. The last part of step 1 was heating phosphoric acid to a uniform temperature of 75 ^{o}C and maintained at that temperature. This was done to lower the viscosity of phosphoric acid which in turn would improve the homogeneity of the mixture during the phosphoric acid and kieselguhr mixing process[31].

The heated phosphoric acid was kept in a sealed glass container because of its hygroscopic nature. It has a greater affinity for water, in the presence of moisture, hydrogen bonds are formed between the polar phosphoric acid molecule and water molecules this result in a change of the concentration of phosphoric acid[32].

Step 2. The heat-treated kieselguhr was then transferred to a sealed container and allowed to cool to ambient temperature in a desiccator cabinet.

Step 3. A suitable quantity of corn starch was added to the kieselguhr samples at room temperature and mixed for 15 minutes in a Kenwood processor equipped with a rotating stainless-steel mixing bowl tightly covered to avoid raising dust during mixing.

Step 3a. If the synthesized catalyst was not calcium or vanadium promoted step 3a was skipped but if it was calcium/vanadium promoted the doping substance was added at step 3a and the powders were further mixed for 15 minutes. Powders were mixed before the addition of phosphoric acid to avoid lumping and provide the uniform blending of powders[33]. The mixing beater was started at the highest mixer speed to achieve the desired homogeneous mixture.

Step 4. Phosphoric acid was added at step number 4 to a mixture of powders and mixed for another 20 minutes to promote homogeneous mixing of the reacting species.

Step 4a. For vanadium promoted catalyst the paste was then allowed to stay for 24 hours before pre-calcination to foster the development of $(VO)_2P_2O_7$ phase[34].

Step 5. The resulting paste would be pre-calcined at 200 ^oC for 20 minutes to condition the paste for forming.

Step 6. For the shaped catalyst the conditioned paste was formed into different cylindrical and quadrilobed extrudates.

Step 7. The formed extrudates were then calcined at varying temperatures ranging from 400 ^oC to 800 ^oC to yield different catalyst series that were placed in a sealed plastic container to prevent moisture contamination[35].

2.3.4 The geometry of the synthesized SPA catalysts.

The following quantities of raw materials were used during the synthesis of the SPA catalyst and in all synthesized catalysts SPAMT is defined as S = Solid, PA = Phosphoric Acid, M = Mined kieselguhr, T = Calcination temperature. For SPAMCaT, Ca = Calcium used for doping, the same is true for SPAMVT, V = Vanadium used for doping. The acronym SPAS was used where S = Synthetic kieselguhr. The photographs of the synthesized SPA catalysts are presented below showing distinct shapes of the synthesized catalysts.

SPAMT was prepared by impregnating a mixture of 166.4 g mined kieselguhr, 9.9 g corn starch with 499.6 g phosphoric acid. The following catalysts SPAM400, SPAM500, SPAM600, SPAM700 and SPAM800 were prepared.



Figure 2.5 The photograph of the synthesized cylindrically shaped unpromoted SPAM400 catalyst synthesized using mined kieselguhr and calcined at 400 ^{o}C showing cylindrical extrudates.

SPAMCaT was prepared by impregnating a mixture of 227.8 g mined kieselguhr, 11.6 g corn starch, 136.2 g Calcium triphosphate with 685.5 g phosphoric acid. SPAMCa400, SPAMCa500, SPAMCa600, SPAMCa700 and SPAMCa800 catalyst were prepared.



Figure 2.6 The photograph of the synthesized cylindrically shaped calcium promoted SPAMCa400 catalyst synthesized using mined kieselguhr and calcined at 400 ^{o}C.

SPAMQT was prepared by impregnating a mixture of 160.1 g, mined kieselguhr, 9.5 g corn starch with 499.5 g phosphoric acid. SPAMQ400, SPAMQ500, SPAMQ600, SPAMQ700 and SPAMQ800 were prepared.



Figure 2.7 The photograph of the synthesized quadrilobed shaped SPAMQ400 catalyst calcined at 400 ^{o}C and synthesized using mined kieselguhr showing distinct quadrilobed shaped extrudates with all four vertices.

SPAMQCaT was prepared by impregnating a mixture of 157.5 g mined kieselguhr, 10.1 g corn starch, 136.2 g Calcium triphosphate and 491.6 g phosphoric acid. SPAMQCa400, SPAMQCa500, SPAMQCa600, SPAMQCa700 and SPAMQCa800 were prepared.

SPAMVT was prepared by impregnating a mixture of 171.6 g, mined kieselguhr, 10.1 g corn starch, 18.9 g Vanadium pentoxide with 587.6 g phosphoric acid. SPAMV400, SPAMV500, SPAMV600, SPAMV700 and SPAMV800 were prepared.

SPAST was prepared by impregnating a mixture of 165.2 g synthetic kieselguhr, 8.8 g corn starch with 490.1 g phosphoric acid. SPAS400, SPAS500, SPAS600, SPAS700 and SPAS800 were prepared.



Figure 2.8 The photograph of the synthesized cylindrically shaped SPAS400 catalyst synthesized from synthetic kieselguhr, the catalyst is cylindrically shaped just like the SPAMT catalyst series.

SPASCa was prepared by impregnating a mixture of 168.1 g, synthetic kieselguhr, 8.4 g corn starch, 96.9 g Calcium triphosphate with 501.8 g phosphoric acid. Catalysts SPASCa400, SPASCa500, SPACa600, SPASCa700 and SPACa800 were prepared.



Figure 2.9 The photography of the synthesized cylindrical-shaped and calcium promoted SPASCa400 catalyst synthesized from synthetic kieselguhr and calcined at 400 ^{o}C.

2.4 Characterization of the synthesized SPA catalysts.

2.4.1 Free acid and crushing strength of the SPA catalysts.

In this work, determination of free acid was done using Titrando 888 auto titrator calibrated before experiment using pH buffer 4 and 7 an mV/pH slope of 97 and above was considered

acceptable. Thereafter about 1 g sample of grounded catalyst was immersed in 100 mL of deionized water in a 100 mL beaker with a magnetic stirrer at room temperature[36]. The sample was then titrated against sodium hydroxide to endpoint pH 4.4 and the results are reported in Chapter 3. However, the SPA catalyst-free acid concentration has an inverse relationship with SPA catalyst crushing strength. High free acid foster lower crushing strength and lower free acid fosters high crushing strength.

The SPA catalyst crushing strength characterization was performed using the Dr Schleuniger® hardness test instrument (MultiTest 50). The instrument was calibrated by an external service provider and its reliability was evaluated using commercial standard reference material. The instrument was fitted with movable and fixed jaws in the test area. A pellet under analysis was pushed in between the jaws. A moving jaw pushes it against a fixed jaw and the lateral force at the point of pellet breaking was recorded.

2.4.2 A study of the mercury intrusion pore volume and BET surface area of the synthesized SPA catalysts.

In literature, there is no pore volume and pore structure data for the SPA catalyst, hence in this work the mercury intrusion pore volume analysis technique was chosen to investigate the presence of macropores. This was done using AutoPore IV 9500 V1.09 instrument from Micromeritics Instrument Corporation. The instrument reliability was determined by running a commercial silica standard concurrently with the samples in different ports (the instrument have 4 low pressure and 2 high-pressure sample ports). In 1 port a reference material was analyzed and in the other 3 ports, experimental samples were analyzed. A deviation of the reference sample greater than 2 % would render analytical results unacceptable.

A sample mass between 1.0 g and 2.5 g of the catalyst in the form that it was synthesized was weighed and dried in the kiln at 200 ^{o}C for 1 hour to drive out moisture[37]. The prepared samples were loaded into the instrument and analyzed initially at low pressure and later at high pressure. The instrument had sample evacuation pressure of 50 µmHg, evacuation time of 5 minutes, mercury filling pressure of 1.5 psi and equilibration time of 10 seconds.

In addition to the macropore volume analysis, it was important for the analysis of micro and mesopores to be conducted as well. In view of that, the nitrogen physisorption technique was chosen for the surface area and pore volume (micro and mesopores) analysis of the synthesized solid phosphoric acid catalysts. The nitrogen physisorption technique uses adsorption/desorption isotherms of liquid nitrogen at −196 ^{o}C. The reliability of the instrument was checked by analyzing a known external standard of aluminium oxide and compare the results to the known value, a deviation to a maximum of 3 % was considered acceptable. In addition to that, the experiments per sample were repeated until at least 3 results agree then any result of the three is here reported. Brunauer-Emmett-Teller (BET) data was collected on a Micrometrics TRISTAR 2000 analyzer. About 0.2 g – 0.5 g of the SPA catalyst(calcined at 500 ^{o}C) samples were analyzed after degassing under N_2 at a temperature of 350 ^{o}C for six hours[38].

2.4.3 Determination of crystalline phases in synthesized SPA catalysts using the PXRD technique.

PXRD analysis of all synthesized SPA catalysts was done using Bruker D2 Phaser diffractometer operating at 30 kV and 10 mA current, fitted with a LynxEye (1D mode) detector and a goniometer with a circle radius of 141.1 mm. The instrument measurement reliability was always checked before the experiment by running a known commercial quartz standard reference material at the same settings as the experiment. The samples of synthesized SPA catalyst with a mass of 1 g to 2 g were ground to a fine powder and loaded onto the XRD sample holder which was taken to the instrument and analyzed.

All PXRD data collection experiments for the synthesized SPA catalyst were run at an angular angle range of 0 ^{o} to 50 ^{o}, but predominantly crystalline phases were only found in the angular range between 20 ^{o} and 35 ^{o}. The X-ray diffraction experiments were conducted in order to determine if the synthesized SPA catalysts were crystalline or amorphous[39]. The instrument settings that were used for all PXRD experiments are reported in Table 2.3 below.

Table 2.3 PXRD instrument settings used for all PXRD experiments.

Component	Value
X-ray source tube type	Copper
Wavelength	λ =1.54184 Å
Primary and secondary Soller slits	2.5 mm
Receiving Slit	2.5 mm
Fixed Divergence Slit	1.0 mm
Angular angle range	0 º - 90 º
Nickel Filter	yes
Scan type	Coupled Two theta/theta
Step size (º/Sec)	0.0080
Time per step (Sec)	0.13

Conventionally, knowledge of the crystallite size of the catalytic material provides the basis for the design of an optimal catalyst structure. Various crystallite size determination methods can be used, however, the Scherrer model remain accessible to researchers and it is fairly accurate[40]. The accuracy of the crystallite size from the Scherrer equation is influenced by the contributions of instrumental broadening, morphological effects and disorder to reflection width and the potential complication of their anisotropy[41]. In this work, the Scherrer model was used to calculate the crystallite size[42] this model assumes that all the crystallites are spherical[43].

In addition to the use of the Scherrer model for the determination of the crystallite size, the morphological investigation of the SPA catalysts can be accomplished by employing various techniques[44]. These are Differential Scanning Calorimetry (DSC), thermal analysis, dynamic light scattering, Porosimetry, interferometry and microscopy[45]. The Porosimetry techniques give information about the pores of the catalyst, one can determine pore structure and pore size[46]. This information is secondary, as useful as it is, it does not tell the morphology of the crystal

system of the catalyst. However, TEM and SEM techniques provide a structured and detailed morphological investigation of the catalytic material.

2.4.4 Investigation of the synthesized SPA catalysts grain geometry and elemental composition using TEM and EDS techniques.

Electron microscopy provides a real-time investigation of the catalyst structure[47], which reveals the crystal grains, shape of the grains, boundaries and information for the determination of lattice parameters[48]. SEM(Scanning Electron Microscopy) and TEM(Transmission Electron Microscopy) are the commonly used techniques in catalysis research[49]. They use the beam of electrons that travel through a vacuum where electromagnets are used to focus the beam on the sample resulting in interactions inside the irradiated sample affecting the electron beam[50]. These interactions and effects are detected and transformed into images which are then interpreted[51].

The main difference between SEM and TEM is that SEM creates an image by detecting backscattered electrons, while TEM uses transmitted electrons (electrons that pass through the sample) to create an image[52]. As a result, TEM gives information on the inner structure of the sample, such as crystal structure, morphology, and stress state information, while SEM provides information on the sample's surface and its composition[53].

In this work, transmission electron microscopy (TEM) was used to investigate the SPA catalysts morphology. TEM utilizes a beam of electrons that passes through the ultra-thin sample to the detector, a 2D image is formed using a charge-coupled device camera[54]. The images can be used to extract morphological, compositional, and crystallographic information engrained in them[55]. This technique creates high-resolution 2D images[56] which allows the researcher to view the sample at a molecular level and investigate a wide range of characteristics[57]. However, like any other analytical technique, TEM does have its limitations, it is laborious, expensive and require extensive training before one can generate reliable analytical results[58].

Herein, SPAM500, SPAMCa500, SPAMV500, SPAS500 and SPASCa500 catalysts were analyzed using TEM. Characterization was done using a JEOL JEM 2100 Transmission Electron Microscope operated at a voltage of 200 kV at the University of KwaZulu Natal laboratories[59]. Detailed

sample background data was provided in the service request form to the service provider to enable them to select the most suitable settings and reference material for data validation.

The catalyst pellets were ground in an agate mortar to fine powders[60]. A small amount of the catalyst powder was placed in ethanol (99.8 % Aldrich) to form a slurry which was ultrasonicated for 30 seconds to homogenize the sample[61]. It was then dropped cast onto a copper grid with a lacy carbon film and allowed to dry, after drying the samples were run on TEM[34]. In addition to the SPA catalyst TEM crystal investigation, the elemental composition of the synthesized SPA catalyst was spectroscopically determined.

Energy dispersive spectroscopy (EDS) is a non-destructive technique traditionally used in scanning electron microscopy (SEM) for the local determination of chemical elements in solid samples[62]. The sample is bombarded with electrons having energy above 30 keV[63]. The chemical composition is measured by illuminating a sample in the vacuum chamber with a focused electron beam[64]. The electrons bombarding the specimen surface are scattered into the material and ionizes the specimen atoms by knocking out secondary electrons from the stationary shells[65]. The resulting electron holes are filled by an avalanche of electrons from the outer shells of the atom[66].

The ionized atoms emit X-ray quanta of discrete energy, which are characteristic of the chemical elements of the sample under analysis[67]. The X-ray emitted photons are collected by an EDS detector near the sample and transmitted to the multi-channel analyzer, in which the oscillations are separated according to their amplitude[68]. The number of quanta (the intensity) of characteristic X-rays emitted in a given time interval by the atoms of the investigated element is proportional to the concentration of that element in the sample[69]. The spectra are transferred to the specialized computer equipped with specialized software for the collection, observation, calculation and storage of the spectral data[70].

The quantification of atomic composition using STEM-EDS has its challenges such as electron beam spreading and channelling[71] which can lead to the relative contribution from neighbouring columns. These effects are dependent on the concentration at the atomic

columns[72] however, its effect can be mitigated by the use of a fine probe that focuses on a specific column of atoms[73].

In this work, the STEM specimens were prepared by mechanical polishing, followed by Argon ion milling[74]. The atomic-scale chemical mapping and EDS spectral images were acquired as a series of frames, where the same focal point was scanned multiple times[75]. The spatial drifting of the frames was corrected to build up spectral image data[76]. The total spectral image collection time was 376 seconds. The EDS spectral image data were acquired with an electron probe of size <0.18 nm and a convergence angle of 23.3 ^{o} [77]. The elemental mapping was carried out by collecting point by point EDS spectrum of each of the corresponding pixels in the map. The collected maps were presented in the form of a matrix of coloured pixels with the intensity corresponding to the amount of the element[78].

2.5 Conclusion.

Herein, the SPA catalysts were successfully synthesized in the form of cylindrical extrudates with lengths in the range of 6.0 – 10.0 mm using synthetic and mined kieselguhr. The synthesis of quadrilobed SPA catalyst was met with the hindrance of the polymer inserts failing to withstand the pressure, however, a few quadrilobed pellets were synthesized. The use of quadrilobed shaped steel die plates need to be considered for this experiment in future studies. Synthesis of vanadium promoted SPA catalyst was also successfully carried out. In addition to that, the synthesis of cylindrically shaped unpromoted and calcium promoted SPA was met with no challenges. This led to the conclusion that a change in silica source has an insignificant effect on the shaping of the SPA catalyst.

2.6 References.

(1) Wu, J. Q.; Li, P.; Li, Y. G.; Liu, S. R.; Li, Y. S. Synthesis, Structural Characterization, and Olefin Polymerization Behavior of Vanadium(Iii) Complexes Bearing Tridentate Schiff Base Ligands. *Organometallics* **2009**, *28* (6), 1817–1825. https://doi.org/10.1021/om801028g.

(2) Zakeri, M.; Samimi, A.; Shafiee Afarani, M.; Salehirad, A. Effects of Porosity and Pore Size Distribution on Mechanical Strength Reliability of Industrial-Scale Catalyst during Preparation and Catalytic Test Steps. *Part. Sci. Technol.* **2018**, *36* (1), 96–103. https://doi.org/10.1080/02726351.2016.1220437.

(3) Gaber, A.; Abdel-Rahim, M. A.; Abdel-Latief, A. Y.; Abdel-Salam, M. N. Influence of Calcination Temperature on the Structure and Porosity of Nanocrystalline SnO 2 Synthesized by a Conventional Precipitation Method. *Int. J. Electrochem. Sci* **2014**, *9*, 81–95.

(4) Thommes, M.; Kaneko, K.; Neimark, A. V.; Olivier, J. P.; Rodriguez-Reinoso, F.; Rouquerol, J.; Sing, K. S. W. Physisorption of Gases, with Special Reference to the Evaluation of Surface Area and Pore Size Distribution (IUPAC Technical Report). *Pure Appl. Chem.* **2015**, *87* (9–10), 1051–1069. https://doi.org/10.1515/pac-2014-1117.

(5) Ercan, C.; Dautzenberg, F. M.; Yeh, C. Y.; Barner, H. E. Mass-Transfer Effects in Liquid-Phase Alkylation of Benzene with Zeolite Catalysts. *Ind. Eng. Chem. Res.* **1998**. https://doi.org/10.1021/ie970797b.

(6) Khabbouchi, M.; Hosni, K.; Mezni, M.; Srasra, E. Structural Characterizations and Mechanical Behavior of Activated Clay-Based Si5(PO4)6O and SiP2O7 Compounds. *Silicon* **2020**, *12* (1), 117–124. https://doi.org/10.1007/s12633-019-00218-1.

(7) Styskalik, A.; Skoda, D.; Moravec, Z.; Roupcova, P.; Barnes, E.; Pinkas, J. Non-Aqueous Template-Assisted Synthesis of Mesoporous Nanocrystalline Silicon Orthophosphate. *RSV Adv.* **2015**, *5*, 73670–73676. https://doi.org/10.1039/c5ra10982e.

(8) Leinenweber, K.; Stearns, L. A.; Nite, J. M.; Németh, P.; Groy, T. L. Structure of a New Form of Silicon Phosphate (SiP 2O 7) Synthesized at High Pressures and Temperatures. *J. Solid State Chem.* **2012**, *190*, 221–225. https://doi.org/10.1016/j.jssc.2012.02.031.

(9) Lawrence N Jacob. Reactivation of Solid Phosphoric Acid Catalyst the United States Patent

US2945822A. United States Patent US2945822A, 6 December 1957.

(10) Arias, M.; Laurenti, D.; Bellière, V.; Geantet, C.; Vrinat, M.; Yoshimura, Y. Preparation of Supported H3PW12040·6H2O for Thiophenic Compounds Alkylation in FCC Gasoline. *Appl. Catal. A Gen.* **2008**. https://doi.org/10.1016/j.apcata.2008.06.042.

(11) Wang, R.; Li, Y. Preparation of MCM-41 Supported Phosphoric Acid Catalyst for Thiophenic Compounds Alkylation in FCC Gasoline. *Catal. Commun.* **2010**, *11* (8), 705–709. https://doi.org/10.1016/j.catcom.2010.01.025.

(12) Galal Mors, H. E. Diatomite: Its Characterization, Modifications and Applications. *Asian J. Mater. Sci.* **2010**, *2* (3), 121–136. https://doi.org/10.3923/ajmskr.2010.121.136.

(13) Freeman, G. J. Rapid Estimation of Effective Bed Voidage for Kieselguhrs. *J. Inst. Brew.* **1993**, *99* (3), 219–221. https://doi.org/10.1002/j.2050-0416.1993.tb01162.x.

(14) Benkacem, T.; Hamdi, B.; Chamayou, A.; Balard, H.; Calvet, R. Physicochemical Characterization of a Diatomaceous upon an Acid Treatment: A Focus on Surface Properties by Inverse Gas Chromatography. *Powder Technol.* **2016**, *294*, 498–507. https://doi.org/10.1016/J.POWTEC.2016.03.006.

(15) Wang, Z. Y.; Zhang, L. P.; Yang, Y. X. Structural Investigation of Some Important Chinese Diatomites. *Glas. Phys. Chem.* **2009**, *35* (6), 673–679. https://doi.org/10.1134/S1087659609060182.

(16) Bettermann, P.; Liebau, F. The Transformation of Amorphous Silica to Crystalline Silica under Hydrothermal Conditions. *Contrib. to Mineral. Petrol.* **1975**, *53* (1), 25–36. https://doi.org/10.1007/BF00402452.

(17) Penn, R. L.; Soltis, J. A. Characterizing Crystal Growth by Oriented Aggregation. *CrystEngComm* **2014**, *16* (8), 1409–1418. https://doi.org/10.1039/c3ce41773e.

(18) Bunaciu, A. A.; Udriştioiu, E. gabriela; Aboul-Enein, H. Y. X-Ray Diffraction: Instrumentation and Applications. *Crit. Rev. Anal. Chem.* **2015**, *45* (4), 289–299. https://doi.org/10.1080/10408347.2014.949616.

(19) Šaponjić, A.; Stanković, M.; Majstorović, J.; Matović, B.; Ilić, S.; Egelja, A.; Kokunešoski, M. Porous Ceramic Monoliths Based on Diatomite. *Ceram. Int.* **2015**, *41* (8), 9745–9752.

https://doi.org/10.1016/j.ceramint.2015.04.046.

(20) Weiner, I.; Rust, M.; Donnelly, T. D. Particle Size Determination: An Undergraduate Lab in Mie Scattering. *Am. J. Phys.* **2001**, *69* (2), 129–136. https://doi.org/10.1119/1.1311785.

(21) Drake, R. M.; Gordon, J. E. Mie Scattering. *Am. J. Phys.* **1985**, *53* (10), 955–962. https://doi.org/10.1119/1.14011.

(22) Price, R. H.; Grover, E. Cosmological Expansion in the Classroom. *Am. J. Phys.* **2001**, *69* (2), 125–128. https://doi.org/10.1119/1.1287354.

(23) Matabal, P. Determination of Particle Size by Micrometrics Saturn DigiSizer II. *Clariant South. Africa Intern. Commun.* **2018**.

(24) Tsai, W. T.; Hsien, K. J.; Lai, C. W. Chemical Activation of Spent Diatomaceous Earth by Alkaline Etching in the Preparation of Mesoporous Adsorbents. In *Industrial and Engineering Chemistry Research*; American Chemical Society, 2004; Vol. 43, pp 7513–7520. https://doi.org/10.1021/ie0400651.

(25) Sing, K. S. W. Assessment of Surface Area by Gas Adsorption. In *Adsorption by Powders and Porous Solids: Principles, Methodology and Applications: Second Edition*; 2013. https://doi.org/10.1016/B978-0-08-097035-6.00007-3.

(26) Gulati, S. T. Design Considerations for Advanced Ceramic Catalyst Supports. In *SAE Technical Papers*; 2000. https://doi.org/10.4271/2000-01-0493.

(27) Wu, D.; Song, L.; Zhang, B.; Li, Y. Effect of the Mechanical Failure of Catalyst Pellets on the Pressure Drop of a Reactor. *Chem. Eng. Sci.* **2003**, *58* (17), 3995–4004. https://doi.org/10.1016/S0009-2509(03)00286-0.

(28) Egloff, G.; Jones, E. K. New and Advanced Developments in Tetramer, Cumene and Motor Polymer Manufacture. In *World Petroleum Congress Proceedings*; 1955.

(29) Lacroix, M.; Nguyen, P.; Schweich, D.; Pham Huu, C.; Savin-Poncet, S.; Edouard, D. Pressure Drop Measurements and Modeling on SiC Foams. *Chem. Eng. Sci.* **2007**, *62* (12), 3259–3267. https://doi.org/10.1016/j.ces.2007.03.027.

(30) Li, Z.; Mu, B.; Chui, S. N. C. Systematic Study of Properties of Extrudates with Incorporated Metakaolin or Silica Fume. *ACI Mater. J.* **1999**, *96* (5), 574–579. https://doi.org/10.14359/660.

(31) Bell, R. N. Composition of Strong Phosphoric Acids. *Ind. Eng. Chem.* **2002**, *40* (8), 1464–1467. https://doi.org/10.1021/IE50464A027.

(32) Ross, W. H.; Durgin, C. B.; Jones, R. M. The Composition of Commercial Phosphoric Acid. *J. Ind. Eng. Chem.* **2002**, *14* (6), 533–535. https://doi.org/10.1021/IE50150A027.

(33) Yip, C. W.; Hersey, J. A. Ordered or Random Mixing: Choice of System and Mixer. *Drug Dev. Ind. Pharm.* **1977**, *3* (5), 429–438. https://doi.org/10.3109/03639047709055622.

(34) Santra, C.; Shah, S.; Mondal, A.; Pandey, J. K.; Panda, A. B.; Maity, S.; Chowdhury, B. Synthesis, Characterization of VPO Catalyst Dispersed on Mesoporous Silica Surface and Catalytic Activity for Cyclohexane Oxidation Reaction. *Microporous Mesoporous Mater.* **2016**. https://doi.org/10.1016/j.micromeso.2015.10.046.

(35) Santander, J. A.; Alvarez, M.; Gutierrez, V.; Volpe, M. A. Solid Phosphoric Acid Catalysts Based on Mesoporous Silica for Levoglucosenone Production via Cellulose Fast Pyrolysis. *J. Chem. Technol. Biotechnol.* **2019**, *94* (2), 484–493. https://doi.org/10.1002/JCTB.5795.

(36) Matabal, P. QCM 01.3 Free Acid by Automatic Titration Using Titroline 5000. *Clariant Sasol Catal. Intern. Commun.* **2020**.

(37) Hajnos, M. Porosimetry. In *Encyclopedia of Earth Sciences Series*; Springer Netherlands, 2011; Vol. Part 4, pp 647–650. https://doi.org/10.1007/978-90-481-3585-1_125.

(38) Shaji, A.; Zachariah, A. K. Surface Area Analysis of Nanomaterials. In *Thermal and Rheological Measurement Techniques for Nanomaterials Characterization*; 2017. https://doi.org/10.1016/B978-0-323-46139-9.00009-8.

(39) Ingham, B.; Toney, M. F. X-Ray Diffraction for Characterizing Metallic Films. In *Metallic Films for Electronic, Optical and Magnetic Applications: Structure, Processing and Properties*; Elsevier Ltd., 2013; pp 3–38. https://doi.org/10.1533/9780857096296.1.3.

(40) Hargreaves, J. S. J. Some Considerations Related to the Use of the Scherrer Equation in Powder X-Ray Diffraction as Applied to Heterogeneous Catalysts. *Catal. Struct. React.* **2016**, *2* (1–4), 1–5. https://doi.org/10.1080/2055074X.2016.1252548.

(41) Lo, B. T. W.; Ye, L.; Tsang, S. C. E. The Contribution of Synchrotron X-Ray Powder Diffraction to Modern Zeolite Applications: A Mini-Review and Prospects. *Chem* **2018**, *4* (8), 1778–1808.

https://doi.org/10.1016/J.CHEMPR.2018.04.018.

(42) Bowen, A. W. The Importance of X-Ray Diffraction in the Non-Destructive Characterisation of High-Strength Aluminium Alloys. *Nondestruct. Charact. Mater. IV* **1991**, 247–257. https://doi.org/10.1007/978-1-4899-0670-0_30.

(43) Muniz, F. T. L.; Miranda, M. A. R.; Morilla dos Santos, C.; Sasaki, J. M. The Scherrer Equation and the Dynamical Theory of X-Ray Diffraction. *Acta Crystallogr. Sect. A Found. Adv.* **2016**, *72* (3), 385–390. https://doi.org/10.1107/S205327331600365X.

(44) Lee, K. O.; Cole, R.; Sekar, R.; Choi, M. Y.; Kang, J. S.; Bae, C. S.; Shin, H. D. Morphological Investigation of the Microstructure, Dimensions, and Fractal Geometry of Diesel Particulates. *Proc. Combust. Inst.* **2002**, *29* (1), 647–653. https://doi.org/10.1016/S1540-7489(02)80083-9.

(45) Nosé, V. Morphology Methods: Cell and Molecular Biology Techniques. *Mayo Clin. Proc.* **2001**, *76* (11), 1181. https://doi.org/10.4065/76.11.1181.

(46) Haugen, H. J.; Bertoldi, S. Characterization of Morphology-3D and Porous Structure. In *Characterization of Polymeric Biomaterials*; Elsevier, 2017; pp 21–53. https://doi.org/10.1016/B978-0-08-100737-2.00002-9.

(47) Moon, R. J.; Pöohler, T.; Tammelin, T. Microscopic Characterization of Nanofibers and Nanocrystals. *Mater. Energy* **2014**, 159–180. https://doi.org/10.1142/9789814566469_0011.

(48) Houghton, M. E.; Amidon, G. E. Microscopic Characterization of Particle Size and Shape: An Inexpensive and Versatile Method. *Pharm. Res. An Off. J. Am. Assoc. Pharm. Sci.* **1992**, *9* (7), 856–859. https://doi.org/10.1023/A:1015884428820.

(49) Mejías, F. J. R.; López-Haro, M.; Gontard, L. C.; Cala, A.; Fernández-Aparicio, M.; Molinillo, J. M. G.; Calvino, J. J.; Macías, F. A. A Novel Electron Microscopic Characterization of Core/Shell Nanobiostimulator Against Parasitic Plants. *ACS Appl. Mater. Interfaces* **2018**, *10* (3), 2354–2359. https://doi.org/10.1021/acsami.7b16873.

(50) Kobler, A.; Kübel, C. Challenges in Quantitative Crystallographic Characterization of 3D Thin Films by ACOM-TEM. *Ultramicroscopy* **2017**, *173*, 84–94. https://doi.org/10.1016/j.ultramic.2016.07.007.

(51) Keller, R. R.; Geiss, R. H. Transmission EBSD from 10nm Domains in a Scanning Electron

Microscope. *J. Microsc.* **2012**, *245* (3), 245–251. https://doi.org/10.1111/j.1365-2818.2011.03566.x.

(52) Sun, C.; Müller, E.; Meffert, M.; Gerthsen, D. Analysis of Crystal Defects by Scanning Transmission Electron Microscopy (STEM) in a Modern Scanning Electron Microscope. *Adv Struct Chem Imag* **2019**, *5*, 1. https://doi.org/10.1186/s40679-019-0065-1.

(53) Anjum, D. H. Characterization of Nanomaterials with Transmission Electron Microscopy. In *IOP Conference Series: Materials Science and Engineering*; Institute of Physics Publishing, 2016; Vol. 146, p 012001. https://doi.org/10.1088/1757-899X/146/1/012001.

(54) Egerton, R. F.; Li, P.; Malac, M. Radiation Damage in the TEM and SEM. In *Micron*; 2004; Vol. 35, pp 399–409. https://doi.org/10.1016/j.micron.2004.02.003.

(55) Donovan, P.; George, B.; Bruson, A.; Dufour, C.; Marchal, G.; Mangin, P. Interpretation of Transmission Electron Microscope Images of Amorphous Silicon/Germanium and Silicon/Iron Multilayers. *J. Appl. Phys.* **1991**, *69* (3), 1371–1376. https://doi.org/10.1063/1.347275.

(56) Abellan, P.; Woehl, T. J.; Parent, L. R.; Browning, N. D.; Evans, J. E.; Arslan, I. Factors Influencing Quantitative Liquid (Scanning) Transmission Electron Microscopy. *Chem. Commun.* **2014**, *50* (38), 4873–4880. https://doi.org/10.1039/c3cc48479c.

(57) Zhou, W.; Greer, H. F. What Can Electron Microscopy Tell Us Beyond Crystal Structures? *Eur. J. Inorg. Chem.* **2016**, *2016* (7), 941–950. https://doi.org/10.1002/ejic.201501342.

(58) Asadabad, M. A.; Eskandari, M. J. Transmission Electron Microscopy as Best Technique for Characterization in Nanotechnology. *Synth. React. Inorganic, Met. Nano-Metal Chem.* **2015**, *45* (3), 323–326. https://doi.org/10.1080/15533174.2013.831901.

(59) Ndlela, S. S.; Friedrich, H. B.; Cele, M. N. Effects of Framework Disruption of Ga and Ba Containing Zeolitic Materials by Thermal Treatment. *Catal. 2020, Vol. 10, Page 975* **2020**, *10* (9), 975. https://doi.org/10.3390/CATAL10090975.

(60) Coster, D.; Blumenfeld, A. L.; Fripiat, J. J. Lewis Acid Sites and Surface Aluminum in Aluminas and Zeolites: A High-Resolution NMR Study. *J. Phys. Chem.* **1994**, *98* (24), 6201–6211. https://doi.org/10.1021/j100075a024.

(61) Pyrz, W. D.; Buttrey, D. J. Particle Size Determination Using TEM: A Discussion of Image

Acquisition and Analysis for the Novice Microscopist. *Langmuir* **2008**, *24* (20), 11350–11360. https://doi.org/10.1021/la801367j.

(62) Goldstein, J. I.; Newbury, D. E.; Michael, J. R.; Ritchie, N. W. M.; Scott, J. H. J.; Joy, D. C.; Goldstein, J. I.; Newbury, D. E.; Michael, J. R.; Ritchie, N. W. M.; Scott, J. H. J.; Joy, D. C. Electron Beam—Specimen Interactions: Interaction Volume. In *Scanning Electron Microscopy and X-Ray Microanalysis*; Springer New York, 2018; pp 1–14. https://doi.org/10.1007/978-1-4939-6676-9_1.

(63) Janik, H.; Wrona, M. Asbestos. In *Encyclopedia of Analytical Science*; Elsevier, 2019; pp 107–116. https://doi.org/10.1016/B978-0-12-409547-2.14311-2.

(64) Ritchie, N. W. M.; Newbury, D. E.; Davis, J. M. EDS Measurements of X-Ray Intensity at WDS Precision and Accuracy Using a Silicon Drift Detector. In *Microscopy and Microanalysis*; 2012; Vol. 18, pp 892–904. https://doi.org/10.1017/S1431927612001109.

(65) Morard, G.; Hernandez, J.-A.; Guarguaglini, M.; Bolis, R.; Benuzzi-Mounaix, A.; Vinci, T.; Fiquet, G.; Baron, M. A.; Shim, S. H.; Ko, B.; Gleason, A. E.; Mao, W. L.; Alonso-Mori, R.; Lee, H. J.; Nagler, B.; Galtier, E.; Sokaras, D.; Glenzer, S. H.; Andrault, D.; Garbarino, G.; Mezouar, M.; Schuster, A. K.; Ravasio, A. In Situ X-Ray Diffraction of Silicate Liquids and Glasses under Dynamic and Static Compression to Megabar Pressures. *Proc. Natl. Acad. Sci.* **2020**, *117* (22), 11981–11986. https://doi.org/10.1073/PNAS.1920470117.

(66) Stanjek, H.; Häusler, W. Basics of X-Ray Diffraction. *Hyperfine Interact. 2004 1541* **2004**, *154* (1), 107–119. https://doi.org/10.1023/B:HYPE.0000032028.60546.38.

(67) Cranswick, L. M. D. Chapter 1: An Overview of Powder Diffraction. *Princ. Appl. Powder Diffr.* **2008**, 1–72.

(68) Goldstein, J. I.; Newbury, D. E.; Michael, J. R.; Ritchie, N. W. M.; Scott, J. H. J.; Joy, D. C.; Goldstein, J. I.; Newbury, D. E.; Michael, J. R.; Ritchie, N. W. M.; Scott, J. H. J.; Joy, D. C. Quantitative Analysis: The SEM/EDS Elemental Microanalysis k-Ratio Procedure for Bulk Specimens, Step-by-Step. In *Scanning Electron Microscopy and X-Ray Microanalysis*; Springer New York, 2018; pp 309–339. https://doi.org/10.1007/978-1-4939-6676-9_20.

(69) Nellist, P. D. Scanning Transmission Electron Microscopy. In *Springer Handbooks*; Springer, 2019; pp 49–99. https://doi.org/10.1007/978-3-030-00069-1_2.

(70) Jones, L.; Macarthur, K. E.; Fauske, V. T.; Van Helvoort, A. T. J.; Nellist, P. D. Rapid Estimation of Catalyst Nanoparticle Morphology and Atomic-Coordination by High-Resolution Z-Contrast Electron Microscopy. *Nano Lett.* **2014**, *14* (11), 6336–6341. https://doi.org/10.1021/nl502762m.

(71) Ponce, A.; Mejía-Rosales, S.; José-Yacamán, M. Chapter 37 Scanning Transmission Electron Microscopy Methods for the Analysis of Nanoparticles. *Methods Mol. Biol. 906*. https://doi.org/10.1007/978-1-61779-953-2_37.

(72) Nellist, P. D. The Principles of STEM Imaging. *Scanning Transm. Electron Microsc.* **2011**, 91–115. https://doi.org/10.1007/978-1-4419-7200-2_2.

(73) Reimer, L. Electron Diffraction Methods in TEM, STEM and SEM. *Scanning* **1979**, *2* (1), 3–19. https://doi.org/10.1002/sca.4950020101.

(74) Sun, C.; Müller, E.; Meffert, M.; Gerthsen, D. Analysis of Crystal Defects by Scanning Transmission Electron Microscopy (STEM) in a Modern Scanning Electron Microscope. *Adv. Struct. Chem. Imaging* **2019**, *5* (1), 1. https://doi.org/10.1186/s40679-019-0065-1.

(75) Abbasi, M.; Kim, D. I.; Guim, H. U.; Hosseini, M.; Danesh-Manesh, H.; Abbasi, M. Application of Transmitted Kikuchi Diffraction in Studying Nano-Oxide and Ultrafine Metallic Grains. *ACS Nano* **2015**, *9* (11), 10991–11002. https://doi.org/10.1021/acsnano.5b04296.

(76) Goldstein, J. I.; Newbury, D. E.; Michael, J. R.; Ritchie, N. W. M.; Scott, J. H. J.; Joy, D. C. *Scanning Electron Microscopy and X-Ray Microanalysis*; Springer New York, 2017. https://doi.org/10.1007/978-1-4939-6676-9.

(77) Wang, X.; Chauvat, M. P.; Ruterana, P.; Walther, T. Effective Absorption Correction for Energy Dispersive X-Ray Mapping in a Scanning Transmission Electron Microscope: Analysing the Local Indium Distribution in Rough Samples of InGaN Alloy Layers. *J. Microsc.* **2017**, *268* (3), 248–253. https://doi.org/10.1111/jmi.12643.

(78) Thomas, P.; Booth, C.; Harmon, R.; Markovic, S.; Twesten, R.; Jarausch, K. Elemental Mapping in Three Dimensions Using 4D STEM-EELS Tomography. *Microsc. Microanal.* **2008**, *14* (S2), 1384–1385. https://doi.org/10.1017/S1431927608086534.

Chapter 3

3. Results and Discussion.

3.1 Free Acid content of the synthesized SPA catalysts.

SPA catalyst has different species of phosphoric acid supported on kieselguhr[1]. These are orthophosphoric acid, pyrophosphoric acid, triphosphoric acid and polyphosphoric acid[2]. These acid species are weakly bonded to the support[3]. Hence, they are hydrolysable by immersing the catalyst in water at room temperature for at least ten minutes[4]. Hydrolysed acid can then be determined by titration using 0.5 molar sodium hydroxide (NaOH) to a pH of 4.4 [5]. During titration, orthophosphoric acid and pyrophosphoric acid react with sodium hydroxide to give sodium salts as shown in Reaction scheme 3.1 below.

$$H_3PO_4 + NaOH \longrightarrow NaH_2PO_4 + H_2O$$

$$NaH_2PO_4 + NaOH \longrightarrow Na_2HPO_4 + H_2O$$

$$H_4P_2O_7 + NaOH \longrightarrow Na_2H_2P_2O_7 + 2H_2O$$

$$Na_2H_2P_2O_7 + 2NaOH \longrightarrow Na_4P_2O_7 + 2H_2O$$

Reaction scheme 3.1 The reaction of orthophosphoric acid and pyrophosphoric acid with sodium hydroxide at room temperature(adapted from reference 6)[6].

Herein, the data from the titration experiments were used to calculate free acid based on the quantity of sodium hydroxide consumed and the mass of the sample used, the amount of free acid was calculated using Equations 3.1 and 3.2 below.

$$Free\ Acid(\%\ H_3PO_4) = \frac{C \times V \times 97.994}{M1} \qquad \text{Equation 3.1}$$

$$Free\ Acid(\%\ P_2O_5) = \frac{Free\ Acid\ \%\ H_3PO_4}{1.380} \qquad \text{Equation 3.2}$$

Where c is the concentration of NaOH in mol/L, V is the volume of NaOH in Litres, 97.994 mol/g is the molecular mass of phosphoric acid in mol/g and M1 is the mass of the sample in grams and 1.38 is the conversion factor from H_3PO_4 to P_2O_5.

In the synthesized SPA catalyst, the amount of free acid decreased with an increase in calcination temperature from 20.1 wt. % P_2O_5 at 400 ^oC for SPAM catalyst series to 1.5 wt. % P_2O_5 at 800 ^oC Figure 3.1 below.

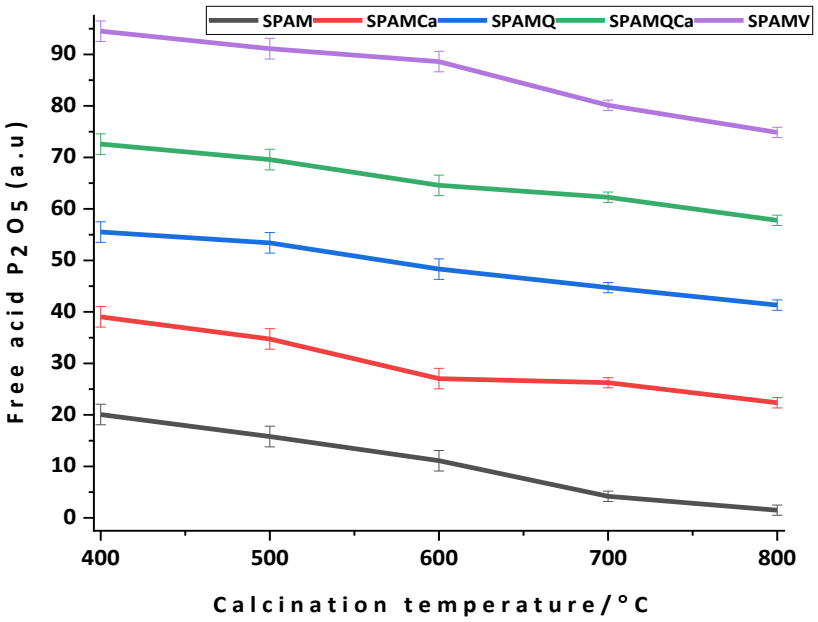


Figure 3.1 Influence of calcination temperature on SPA catalyst (synthesized from amorphous kieselguhr) free phosphoric acid (wt.% P_2O_5). Where SPAM is a cylindrical shaped solid phosphoric acid catalyst synthesized from mined kieselguhr, SPAMQ and SPAMQCa are quadrilobed shaped solid phosphoric acid catalysts synthesized from mined kieselguhr (unpromoted and calcium promoted). SPAMCa is a cylindrical shaped SPA catalyst synthesized from mined kieselguhr and SPAMV is vanadium promoted SPA catalyst synthesized from mined kieselguhr.

The decrease in free acid content in SPA catalysts with an increase in calcination temperature could be caused by thermal dehydration of phosphoric acid[7]. However, the free acid of the SPA catalysts synthesized from crystalline synthetic kieselguhr calcined at 400 ^oC reported very low acid content compared to the free acid in SPAM catalysts Figure 3.2 below.

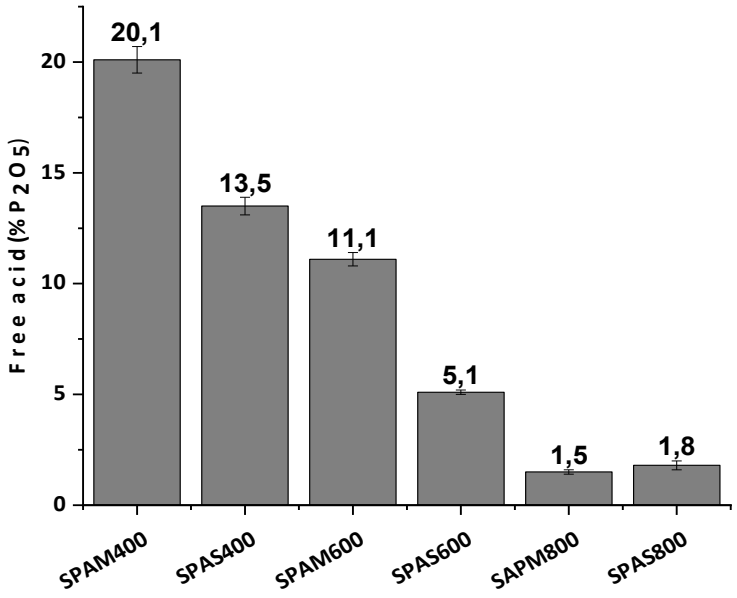


Figure 3.2 Variation in free phosphoric acid of the SPAM and SPAS catalyst synthesized from amorphous and crystalline kieselguhr, SPAM400 means SPA catalyst synthesized from mined kieselguhr calcined at 400 ^{o}C the same is true for SPAS800 stands for SPA catalyst synthesized from synthetic kieselguhr and calcined at 800 ^{o}C.

The difference in free phosphoric acid reported in Figure 3.2 above lies in the structural differences of the kieselguhr support used. Amorphous silica has isolated, vicinal and germinal silanols groups which interact wearily with phosphoric acid via H-bond[8]. However, SiOH groups on the surface of the synthetic kieselguhr enhance the adsorption behaviour of SiO_2 resulting in strong interaction between silica and phosphoric acid thereby forming silicon phosphates hence less free (unbonded) acid available[9].

The reported variation in free acid results of catalysts synthesized from amorphous and crystalline (α-cristobalite) kieselguhr prompted the author to do 7 free acid analyses of catalyst SPAM400 and catalysts SPAS400 and used the data to determine if there is a statistical significance variation in the free acid results.

Table 3.1 Free acid (% P_2O_5) results for SPAM400 and SPAS400 catalysts.

Run	SPAM400	SPAS400
1	20.1 ± 0.1	13.5 ± 0.1
2	19.8 ± 0.1	13.7 ± 0.1
3	20.4 ± 0.1	13.0 ± 0.1
4	20.3 ± 0.1	14.1 ± 0.1
5	19.5 ± 0.1	13.4 ± 0.1
6	20.1 ± 0.1	13.7 ± 0.1
7	20.1 ± 0.1	13.5 ± 0.1

The results in Table 3.1 above were used for statistical analysis and the following statistic were reported below in Table 3.2.

Table 3.2 Statistical data of catalyst SPAM400 and SPAS400 was used to perform a two-sample t-test analysis to determine if there is a significant variation in the free acid of the catalyst SPAM400 and SPAS400.

Statistic	Catalyst SPAM400	Catalyst SPAS400
Sample size	7	7
Degree of freedom	6	6
Sample mean	20.1 ± 0.1	13.6 ± 0.1
Sum of squared deviations	0.37	0.67
Variance	0.06	0.11

The two-sample independent mean analysis reported t-value = 41.38 and p-value < .00001 at

α = 0.01

The t-test results statistically support the conclusion that there is a significant difference in free acid exhibited by the amorphous and crystalline kieselguhr used in SPA catalysts synthesis. However, the decrease in free acid is associated with catalyst dehydration and subsequent conversion of the orthophosphoric acid to a more condensed pyrophosphoric acid[10].

$$\text{SPA.}\chi\, H_2O(s) \xrightarrow{\Delta} \chi H_2O(g) + \chi\text{-1.SPA(s)}$$

Reaction scheme 3.2 Dehydration of SPA catalyst.

Where Δ is heat energy in KJ.mol^{-1}.

However, dehydration of SPA catalyst result in changes in the chemical composition of free phosphoric acid[11] that is;

$$P_2O_5.3H_2O \xrightleftharpoons{\Delta} P_2O_5.2H_2O$$

Orthophosphoric acid Pyrophosphoric acid

Reaction scheme 3.3 Conversion of orthophosphoric acid to pyrophosphoric acid[12].

Where Δ is heat energy in KJ/mol.

It is evident from Reaction scheme 3.3 that, orthophosphoric acid is more hydrated compared to pyrophosphoric acid. This means that free acid in catalyst calcined at higher temperatures is in the form of pyrophosphoric acid[13]. Although pyrophosphoric free acid is beneficial to the catalysis of propene oligomerization by increasing selectivity and activity of the SPA catalyst[14], it takes harsh calcination conditions to synthesize it.

3.2 Correlation between the crushing strength and porosity of the synthesized SPA catalysts.

Hypothetically, low SPA catalyst-free acid should translate into its high catalyst hardness strength[15]. However, practically the relationship of SPA catalyst-free acid and hardness strength is not so simple. It is influenced by other parameters such as the phosphorus to silica ratio and the concentration of the phosphoric acid used for SPA catalyst synthesis[16]. High phosphorus to silica ratio results in high SPA catalyst crushing strength provided the phosphoric acid is highly concentrated in the form of pyrophosphoric acid[17].

The density of the silicon phosphate phases in the SPA catalyst guides SPA catalysts hardness strength. Silicon pyrophosphate has a density of 2.9 g/cm^3 and silicon orthophosphate has a density of 2.7 g/cm^3. The silicon phosphate density data implies that the catalyst with higher silicon pyrophosphate content should have higher catalyst hardness compared to catalysts with higher silicon orthophosphate[18].

In this work, the synthesized SPA catalysts were analyzed for crushing strength and the data was here used to calculate crushing hardness according to Equation 3.3 below[19].

$$C_S = \frac{F_{average}}{L_{average}} \qquad \text{Equation 3.3}$$

Where, C_s is the crushing strength of a catalyst series in N/mm, F is the average breaking force in Newtons of 50 analyzed catalyst pellets and L is the average length in millimetres of the 50 analyzed catalyst pellets[20].

To capture and minimize the catalyst hardness variation in individual pellets, fifty random SPA catalyst pellets per catalyst series were sampled for crush strength analysis. The pellets were run on the instrument using Easy Test Method with a length plausibility range of 6 – 8 mm[19]. The results are reported in Table 3.3 and plotted in Figure 3.3 below.

Table 3.3 Influence of calcination temperature on SPAM, SPAS and SPASCa crushing strength.

Calcination temperature/ ^{o}C	SPAM Crush(N/mm)	SPAS Crush(N/mm)	SPASCa Crush(N/mm)
400	38 ± 2	28 ± 2	35 ± 2
500	43 ± 2	30 ± 2	36 ± 2
600	47 ± 2	35 ± 2	36 ± 2
700	48 ± 2	35 ± 2	39 ± 2
800	48 ± 2	36 ± 2	40 ± 2

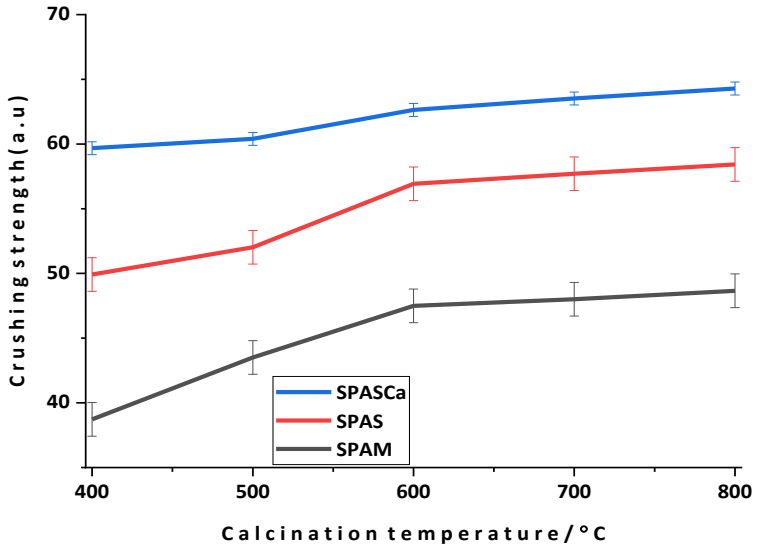


Figure 3.3 Influence of calcination temperature on crushing strength (N/mm) of catalyst SPAM, SPAS and SPASCa.

The catalyst SPAM, SPAS and SPASCa has seen an increase in catalyst crushing strength with an increase in calcination temperature. The increase in crushing strength is prevalent from calcination temperature of 400 ^{o}C until 600 ^{o}C, thereafter the catalyst hardness slowly plateaus off as shown in Figure 3.3 above. This shows that calcination of the SPA catalyst at

temperatures higher than 600 ^{o}C does not provide additional benefit to the mechanical strength, rather the crystal structure could be starting to decompose and release silicon dioxide[21].

The catalyst pore size influences the selectivity of the catalyst and provides the reaction platform for reactant material[22]. These parameters influence other catalyst inherent properties such as density and crushing strength.

In catalysis, pores are void spaces in a material that gaseous reactants, liquids and microscopic particles can occupy[23]. These pores increase the availability of surface area and enable the production of selective product[24]. This is achieved through, directing reactants and products of a particular structure that resonates with the shape of the available pores[25]. Pores are defined by their accessibility to the surface of the porous material, that is; a closed pore is inaccessible to the surfaces; a blind pore is accessible from the surface but does not travel completely from the upstream to the downstream surface and a through pore travels from the upstream surface to the downstream surface of a material[26].

3.3 Mercury intrusion pore volume of the synthesized SPA catalysts.

A gradual increase in mercury intrusion pore volume with an increase in calcination temperature for all catalysts series that was synthesized from mined kieselguhr was reported in Figure 3.4 below. However, the pore volume for catalyst SPAM800 was very low that is 0.20 mL/g the same result as that of catalyst SPAM500. During the mercury intrusion pore volume analysis experiment, the instrument runs at variable pressure. That is from low pressure to high pressure of about 60 000 psi[27]. At high pressure, material deformation may occur resulting in pore collapse, the result was suggesting a possible pore collapse mechanism[28,29].

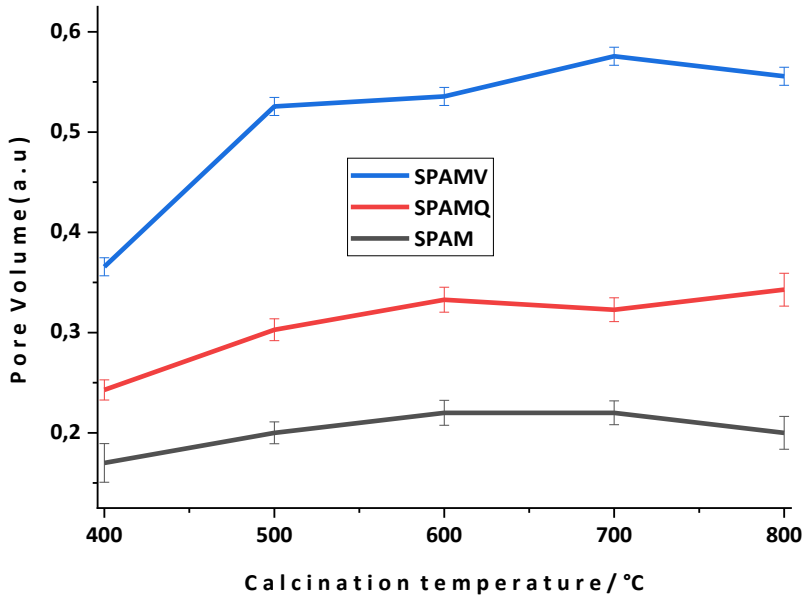


Figure 3.4 Mercury intrusion pore volume in mL/g of the SPAM, SPAMQ and SPAMV catalyst synthesized from mined kieselguhr. Data plotted in Figure 3.4 above is reported in Table 3.4 below.

Table 3.4 Mercury intrusion pore volume of the SPAM, SPAMQ and SPAMV catalyst synthesized from mined and amorphous kieselguhr.

Calcination temperature/ °C	Pore volume (mL/g)		
	SPAM	SPAMQ	SPAMV
400	0.17 ± 0.01	0.22 ± 0.01	0.08 ± 0.01
500	0.20 ± 0.01	0.28 ± 0.01	0.24 ± 0.01
600	0.22 ± 0.01	0.31 ± 0.01	0.25 ± 0.01
700	0.22 ± 0.01	0.3 ± 0.01	0.29 ± 0.01
800	0.20 ± 0.01	0.32 ± 0.01	0.27 ± 0.01

The catalyst that was not calcium promoted and the vanadium promoted SPA catalysts Figure 3.4 above has shown a gradual increase in pore volume until 500 ^{o}C calcination temperature. This could be ascribed to the combustion of volatile and organic material (corn starch) leaving open cavities accessible to mercury intrusion[30]. Near flattening of the curves between calcination temperatures of 500 ^{o}C and 600 ^{o}C indicate that all volatile and organic material that was occupying pores is lost through calcination[31].

Likewise, the increase in pore volume reported in SPAM and SPAMV catalysts beyond calcination temperature of 500 ^{o}C is a result of catalyst decomposition, followed by a subsequent decrease near 800 ^{o}C which is a result of pore collapse[29].

Table 3.5 Influence of calcination temperature on pore volume of calcium promoted catalysts SPA catalysts.

Calcination temperature/ ^{o}C	Pore volume (mL/g)	
	SPAMCa	SPAMQCa
400	0.20 ± 0.01	0.30 ± 0.01
600	0.25 ± 0.01	0.27 ± 0.01
800	0.32 ± 0.01	0.33 ± 0.01

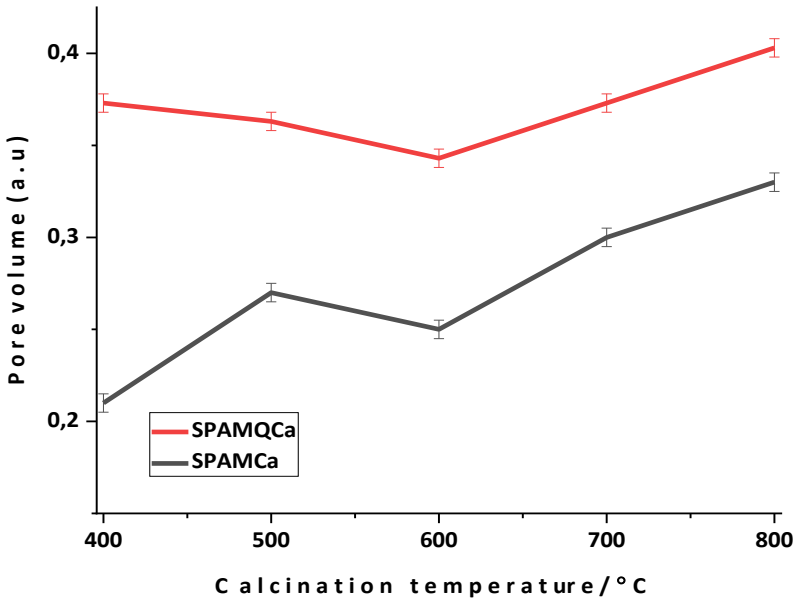


Figure 3.5 Influence of calcination temperature on pore volume of the synthesized calcium promoted SPA catalysts, the data accompanying this graph is reported in Table 3.5 above.

SPAMQCa and SPAMCa catalysts have shown a common trend in pore volume, a decrease in pore volume between calcination temperatures of 500 ^{o}C and 600 ^{o}C. This could be associated with structural rearrangement of the calcium phosphate, this is evident in the sudden increase in pore volume after 600 ^{o}C calcination temperature showing a resultant structural collapse[32].

The phenomenon of structural and pore collapse makes it difficult to explicitly differentiate pore volume influenced by material loss and the actual catalyst pore volume at 600 ^{o}C and above calcination temperature[33]. Hence in this study, the pore volume of the catalyst that was calcined at 500 ^{o}C was considered the best result. This calcination temperature was chosen since the best calcination temperature should be high enough to adequately address the porosity impediment caused by the volatile material effect and have the lowest possible material loss influence[34].

Figure 3.6 below shows the mercury intrusion pore volume of the catalyst that was calcined at 500 ^{o}C. SPAM500 reported the lowest pore volume results compared to SPAM500, SPAMQ500 and SPAMQCa500. This is because the catalyst is compacted cylindrical pellets formed under

high pressure during shaping hence low void space[35]. The pore volume data has shown that the SPA catalyst with a higher ratio of crystalline silicon orthophosphate phase has higher mercury intrusion pore volume compared to the SPA catalyst with a higher ratio of silicon pyrophosphate crystalline phase.

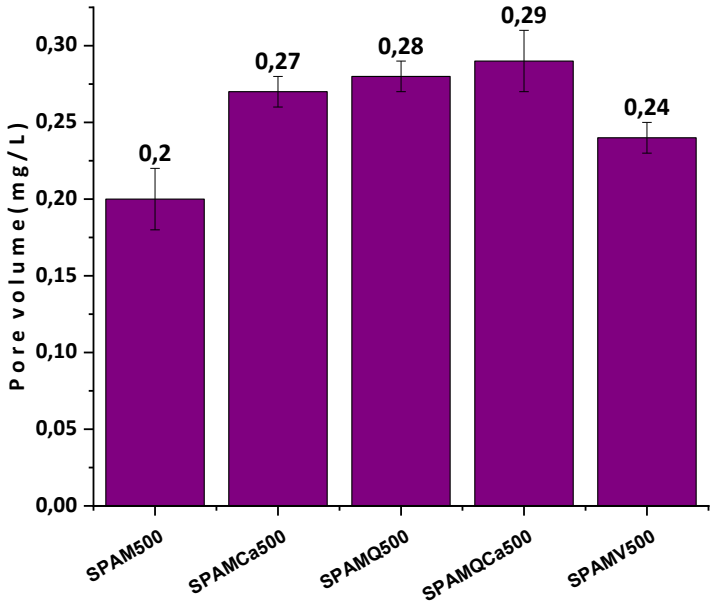


Figure 3.6 Mercury Intrusion Pore volume of the synthesized SPA catalysts calcined at the optimal temperature of 500 ^{o}C.

The pore volume data from the Mercury intrusion technique shows that there are no micropores in all synthesized SPA catalyst[36]. The results reported zero pore volume in all samples for pore diameter below 2 nm Figure 3.7 below. However, this is a confirmation that the Mercury Intrusion Porosimetry technique is not suitable for the analysis of a sample with micropores[37]. This is because the technique depends on the volume of mercury intrusion at a given pressure. That is, at maximum pressure mercury can only intrude pores as low as 0.003 µm[38], thus excluding the micropore range which is below 0.002 µm[39].

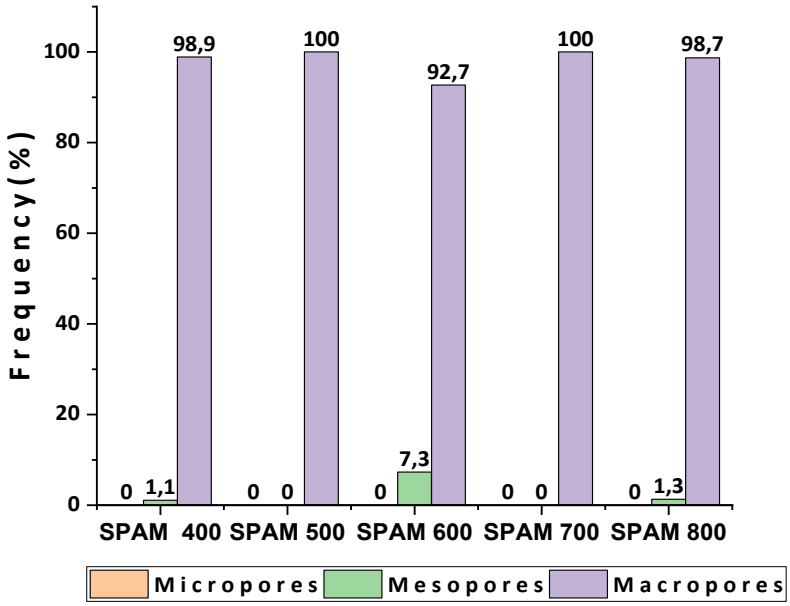


Figure 3.7 Mercury intrusion percentage pore diameter distribution for catalyst SPAMT series showing a high proportion of macropores.

In Figure 3.7 above, the SPAM catalyst series have macropores with all samples reporting at least 92 % of pores having pore diameter above 50 nm this could be that the method that was used for analysis cannot detect smaller pores hence it only reports the macropores data[40]. The same trend was reported in other SPA catalysts.

The porosity of a heterogeneous catalyst affects the mass diffusion properties by influencing the adsorption properties of the catalyst[41]. The presence of macropores enhances the transportation of bulky reactants and the final product in and out of the catalyst[42]. The pore volume of catalyst SPAS and SPASCa was determined using mercury intrusion porosimetry.

Table 3.6 Mecury intrusion pore volume and BET surface area for SPAS and SPASCa catalyst.

Catalyst	MIT Pore Volume mL/g	BET surface area m^2/g	BJH Desorption pore diameter nm
SPAS500	0.3 ± 0.01	2 ± 1	38 ± 2
SPASCa500	0.2 ± 0.01	2 ± 1	11 ± 2

Where MIT is a mercury intrusion technique.

There is a contrasting trend between catalysts synthesized from mined kieselguhr and those synthesized from synthetic kieselguhr when it comes to pore volume results Figure 3.8 below. SPAMT Catalyst series have shown an increase in pore volume with an increase in calcination temperature albeit tailing off at 600 ^{o}C. In addition to that, there is no difference in BET surface area of SPAS500 and SPASCa500, Table 3.6 above. This could be a result of a limit of surface area detection by the physisorption analyzer.

Table 3.7 Influence of calcination temperature on SPAS and SPASCa pore volume compared to SPAM catalysts.

Calcination temperature/ ^{o}C	SPAM (mL/g)	SPAS (mL/g)	SPASCa (mL/g)
400	0.17 ± 0.01	0.29 ± 0.01	0.27 ± 0.01
500	0.20 ± 0.01	0.27 ± 0.01	0.23 ± 0.01
600	0.22 ± 0.01	0.24 ± 0.01	0.20 ± 0.01
700	0.22 ± 0.01	0.33 ± 0.01	0.26 ± 0.01
800	0.20 ± 0.01	0.14 ± 0.01	0.19 ± 0.01

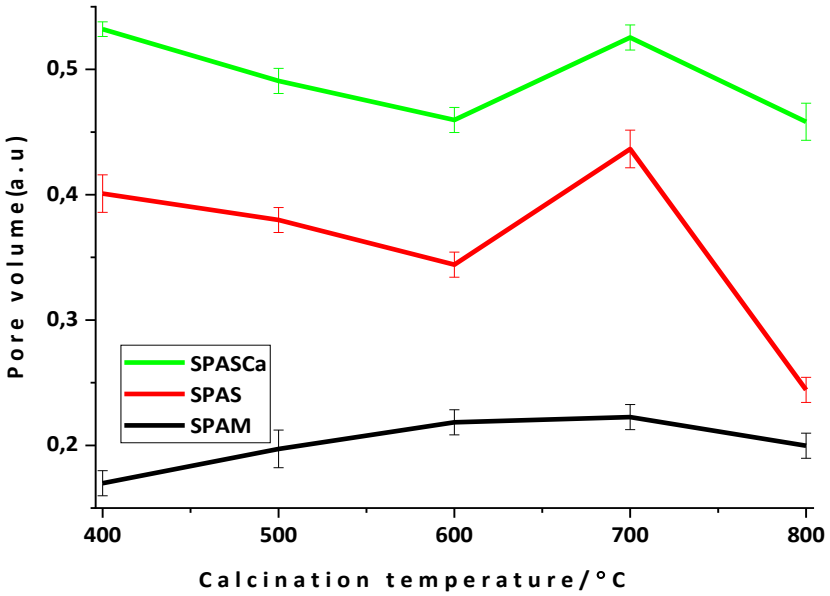


Figure 3.8. Influence of calcination temperature on the SPAS and SPASCa catalyst pore volume compared to SPAM catalyst, accompanying data is reported in Table 3.7 above.

The catalyst pore volume for catalyst SPAS and SPASCa series decreased gradually with an increase in calcination temperature from 400 ^{o}C until 600 ^{o}C. This is caused by pore collapse, surface reconstruction and sintering of particles together with blockage of micropores and mesopores[43]. The decrease in pore volume also in SPASCa is attributed to the effect of calcium pore impediment, the calcium oxide is sitting inside the pores thereby blocking the pores[44]. This is supported by BJH desorption average pore diameter of catalyst SPAS500 which is 38 nm and after calcium promotion went down to 11 nm Table 3.6 above.

The limitation of the mercury intrusion technique to determine micropores and mesopores was mitigated using a complementary Nitrogen adsorption technique. The technique uses nitrogen adsorption at a temperature of – 196 ^{o}C to determine specific surface area and pore volume[45].

3.4 BET surface area of the synthesized SPA catalysts and their pore structure.

Physisorption analysis is an important tool that can be used in the morphological characterization of the catalyst[46]. N_2 adsorption technique was here used to determine the BET

surface area of the synthesized SPA catalysts, Figure 3.9 below shows the BET surface area of the SPA catalysts synthesized from mined kieselguhr.

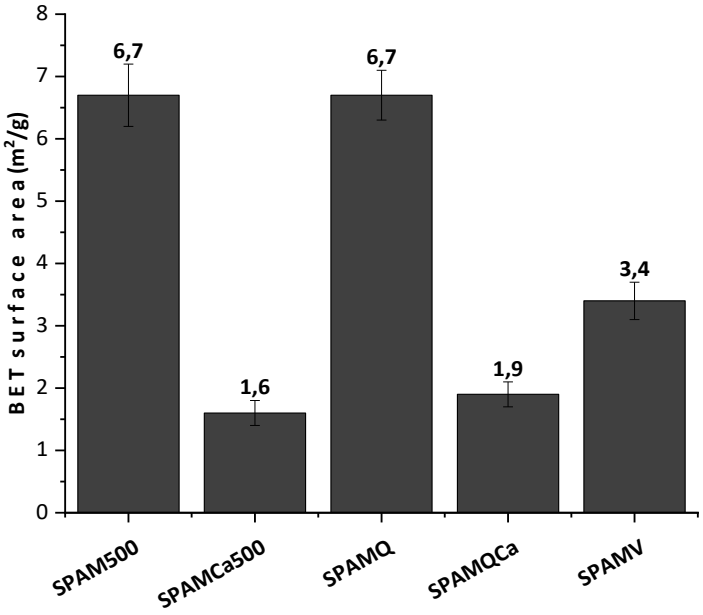


Figure 3.9 BET surface area of the SPA catalysts synthesized from mined kieselguhr, these results were reported after repeating the BET analysis experiments 3 times to determine the experimental uncertainty effect and the results agree.

The BET surface area results of unpromoted SPA catalyst SPAM500 and SMAQ500 indicate that there is no variation to the surface area of the cylindrically shaped SPA catalyst compared to the quadrilobed shaped SPA catalyst. However, on promotion with both calcium and vanadium, a drop in BET surface area was reported albeit low in vanadium promotion. This general decrease in BET surface area after the promotion is a result of surface inhomogeneity provided by the addition of promotion metal to the catalyst[47].

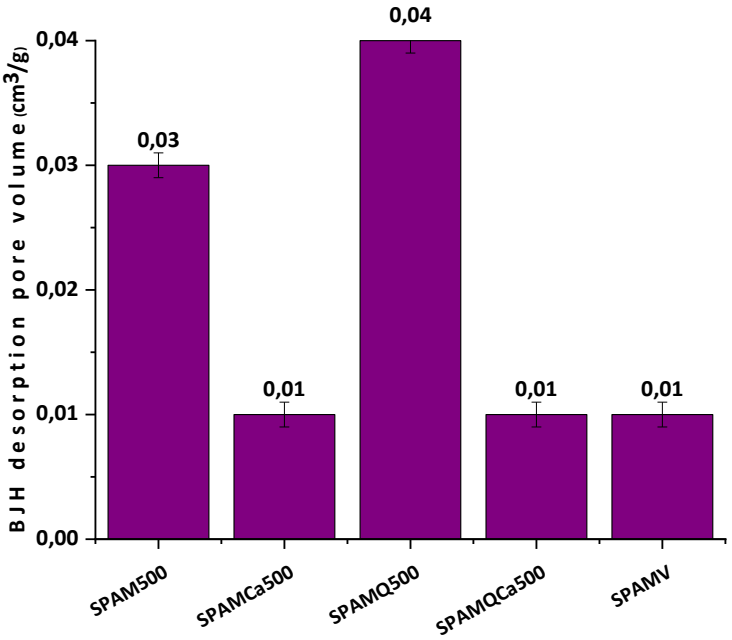


Figure 3.10 BJH desorption pore volume of the catalysts synthesized from mined kieselguhr.

The comparison of catalyst SPAM500 and SPAMQ500 BJH desorption pore volumes Figure 3.10 above also show insignificant differences in the pore volume results of the unpromoted catalysts synthesized from mined kieselguhr. Furthermore, there is a notable decrease in the pore volume of the promoted SPA catalysts, the decrease in BJH desorption pore volume is caused by metal clogging of pores[48]. This effect is more prevalent in SPAMCa500 catalyst which is calcium promoted than catalyst SPAMV500 which is vanadium promoted. BJH desorption pore volume was used to interpret the SPA catalyst pore volume results. This is because BJH adsorption corresponds to the progressive filling of the mesopores whilst BJH desorption refers to a sudden emptying of the same pores. Therefore, the desorption data provides the characteristics of the pore neck and the aesthetic pore size distribution.

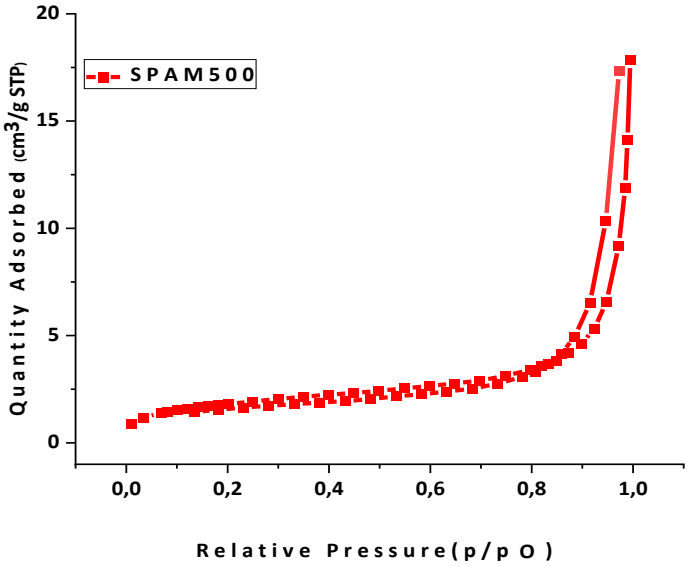


Figure 3.11 Isothermal linear plot showing adsorption and desorption behaviour of the SPAM500 catalyst.

The isothermal linear plot of the SPAM500 catalyst exhibited a well-defined type IV isotherm with an H1 hysteresis loop which has an inflexion point other than the final saturation plateaue[49]. The adsorption branch contains a low slope region associated with multilayer adsorption at pore walls, followed by pore condensation in mesopores ending with an inflexion point. This implies incomplete filling of pores and hence the availability of macropores [50]. This is in agreement with mercury intrusion macropore volume results reported earlier on.

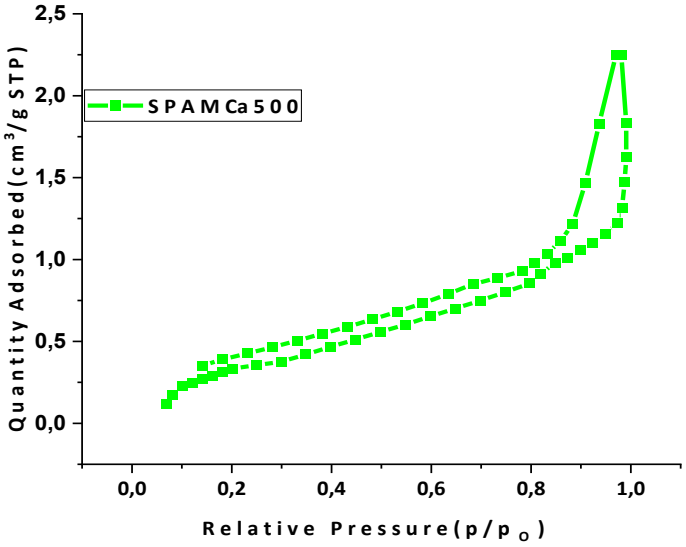


Figure 3.12 Isothermal linear plot showing the adsorption and desorption characteristics of the SPAMCa500 catalyst.

The isothermal linear plot of SPAMCa500 shows a well-defined type IV isotherm with an H1 hysteresis loop which has an inflexion point other than the final saturation plateaue[51]. This is indicative of pores that are connected by constrictions with other pores having no direct access to Nitrogen gas reservoir but indirect access through many constrictions and cavities[52].

Therefore, if evaporation is started when the pore system is filled, a cavity cannot empty as long as a vapour path is not created to the vapour reservoir but as soon as the pressure is reduced to a critical value, the pore system begins to empty, and many routes are created from the vapour reservoir to the buried pores. This result in the emptying of the whole pore system in a cascade-like giving the asymmetrical shape starting near relative pressure(P/P_O) 0.8 to 1.0 [53]. This shows that the catalyst has mesopore to macropores type of pores. The absence of a plateaued shape at P/Po = 1 indicate that the mesopores were not filled. That also succinctly supports the pore size results from MIT which shows that SPA catalyst has macropores and capillary type of pores.

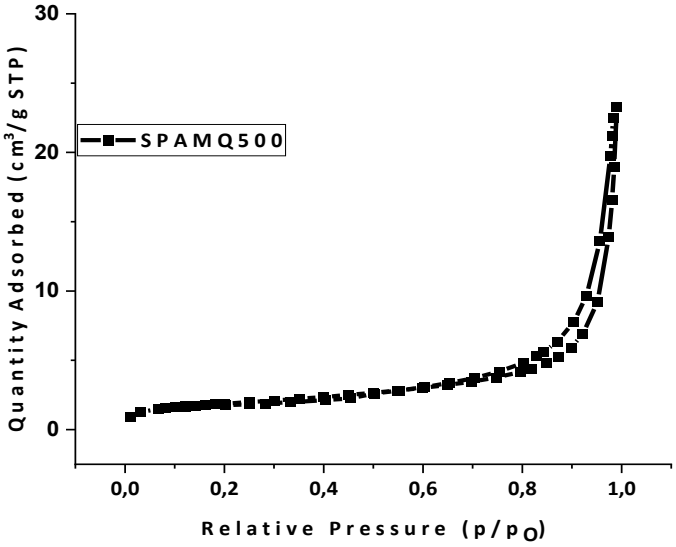


Figure 3.13 Isothermal linear plot showing the adsorption and desorption behaviour of the SPAMQ500 catalyst.

The isothermal linear plot of the SPAMQ500 catalyst has shown a Type IV isotherm with an H1 hysteresis loop. The adsorption branch contains a low slope region associated with multilayer adsorption at pore walls, followed by pore condensation in mesopores ending with an inflexion point[50]. The desorption branch proceeds into a narrow hysteresis loop, with the desorption branch parallel to the adsorption branch. This is indicative of a narrow distribution of uniform mesopores and limited pore network effects[54].

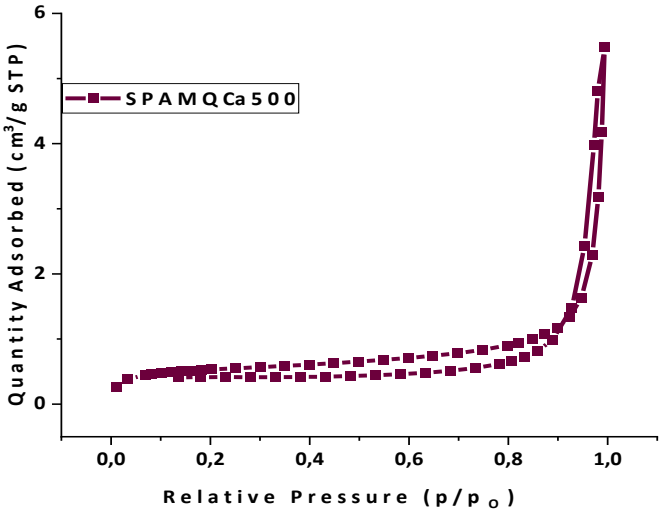


Figure 3.14 Isothermal linear plot showing the adsorption and desorption behaviour of the SPAMQCa500 catalyst.

The isothermal plot of both SPA catalyst SPAS500 and SPASCa500 exhibited a Type IV isotherm with an H3 hysteresis loop. This tells us that the catalyst has non-rigid aggregates of plate-like particles resulting in slit-shaped and ink bottle pores[55].

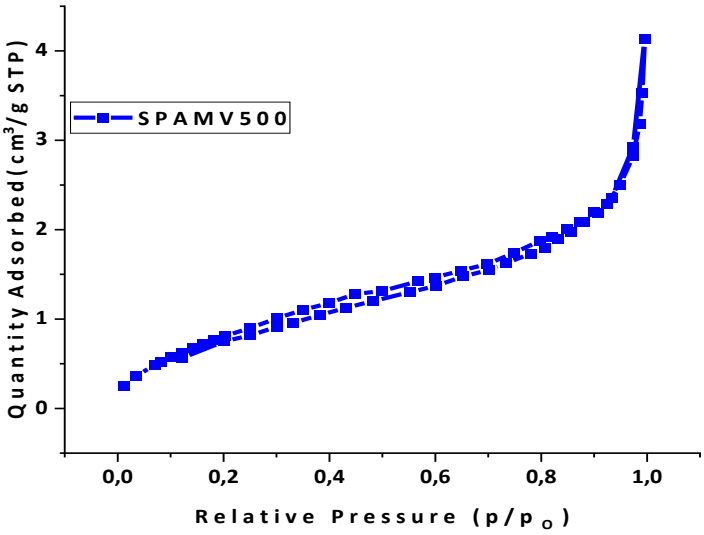


Figure 3.15 Isothermal linear plot showing the adsorption and desorption characteristics of the SPAMV500 catalyst.

The isothermal plot of SPAMV500 Figure 3.15 has shown a Type II isotherm with an H3 hysteresis loop, the results are associated with unrestricted monolayer-multilayer adsorption, a condition indicative of the catalyst characterized by mesopores and to some extent macropores [56]. This behaviour can be caused by assemblages of slit-shaped pores, which is a result of macropores networks that are not filled with pore condensate[57].

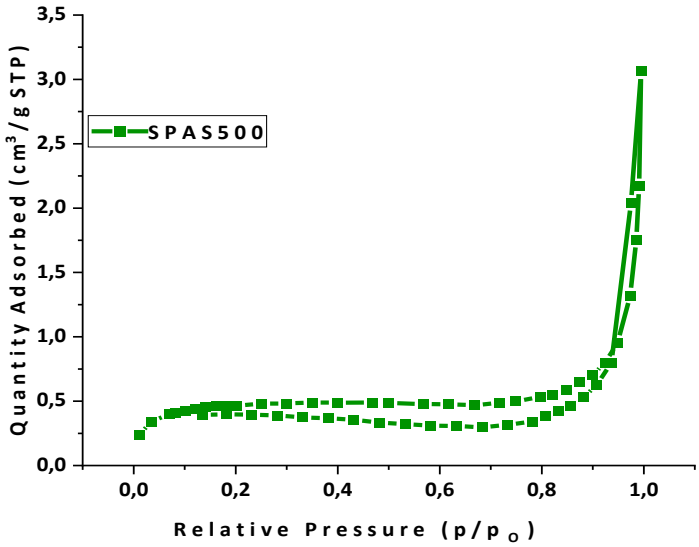


Figure 3.16a The isothermal linear plot showing the adsorption and desorption behaviour of the SPAS500 catalyst.

The isothermal linear plot of the SPAS500 catalyst has shown a Type IV isotherm with an H1 hysteresis loop. The adsorption/desorption branches are near parallel with an asymptotic closure that is indicative of the presence of mesopores[50]. The desorption branch proceeds into a narrow hysteresis loop, near parallel to the adsorption branch. This is indicative of a narrow distribution of uniform mesopores and limited pore network effects[54].

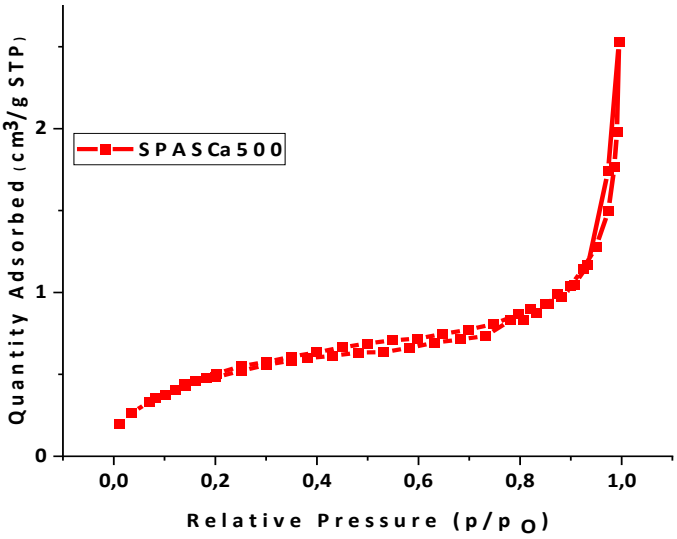


Figure 3.16b The Isothermal linear plot showing the adsorption and desorption characteristics of the SPASCa500 catalyst.

The isothermal plot of SPASCa500 exhibited a Type IV isotherm with an H3 hysteresis loop characterized by near perpendicular closure[45]. This tells us that the catalyst has non-rigid aggregates of plate-like particles resulting in slit-shaped and ink bottle pores[30]. However, the point of inflexion at a relative pressure of (P/P_O = 0.0 - 0.2) indicate completion of monolayer coverage [49]. The inflexion reported between relative pressure of 0.4 – 0.9 corresponds to capillary condensation, with a steepness increased towards relative pressure 1.0 indicates a narrow pore size distribution[53]. This also shows that pore blockage by calcium promotion was nonselective. The BET experimental results emphasized the presence of mesopores in the SPA catalyst.

3.5 Crystalline phases of the synthesized SPA catalysts.

Silica and phosphorus react to give different silicon phosphate polymorphs herein, crystalline phase identification was done on all diffractograms with the help of Diffracplus Eva software and ICDD (international centre for diffraction data) database. The SPAM catalyst had silicon-orthophosphate PDF 00-022-1380 and silicon-pyrophosphate PDF 00-022-1320 phases Figure 3.17 below. This agrees with the results reported by Clearfield and his coworkers[58]. The

tetragonal silicon pyrophosphate belongs to space group $P6_3$ with a = 14.2 Å, b = 7.8 Å and c = 7.4 Å, α = β = γ = 90 ° [59]. The hexagonal silicon orthophosphate belongs to space group $R\bar{3}$ with lattice parameters a = b = 7.8 Å and c = 24.0 Å , α = β = 90 ° and γ = 120 ° [60]. The data from literature has shown that the SPA catalyst crystalline phase peaks are predominant in the angular range of 20 ° to 35 ° hence the same range was used in this work.

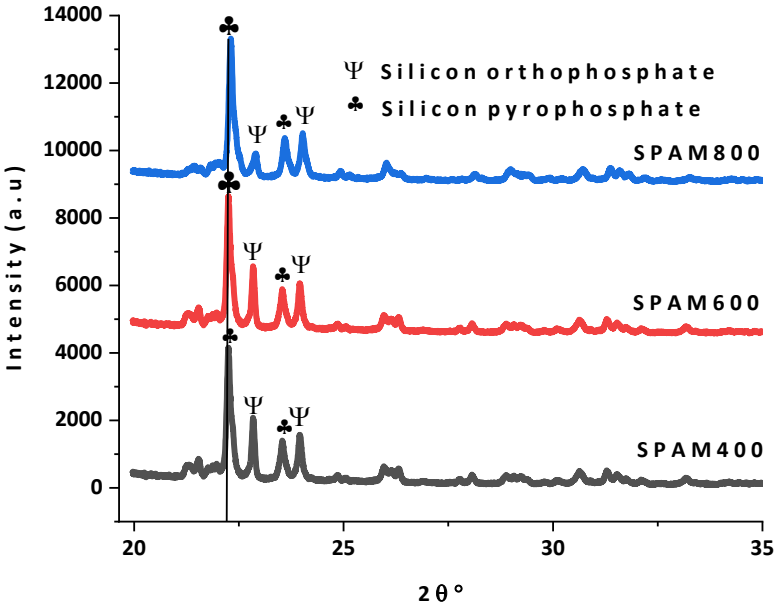


Figure 3.17 Influence of calcination temperature on the transformation of silicon orthophosphate to silicon pyrophosphate of the SPAM catalysts.

The peak ratio of the silicon orthophosphate peak in SPAM catalyst calcined at 400 °C relative to the silicon pyrophosphate peak at the same calcination temperatures changes with an increase in calcination temperature. At higher calcination temperature the silicon pyro peak height becomes predominantly greater than silicon orthophosphate peak height indicating an increase in crystallinity[61]. This shows the interrelationship between the silicon pyrophosphate and silicon orthophosphate phases. The transformation from silicon orthophosphate to silicon pyrophosphate is directly influenced by calcination temperature[62]. However, random errors from sample loading of the PXRD instrument could have also contributed to the variation in peak height albeit within a margin of error.

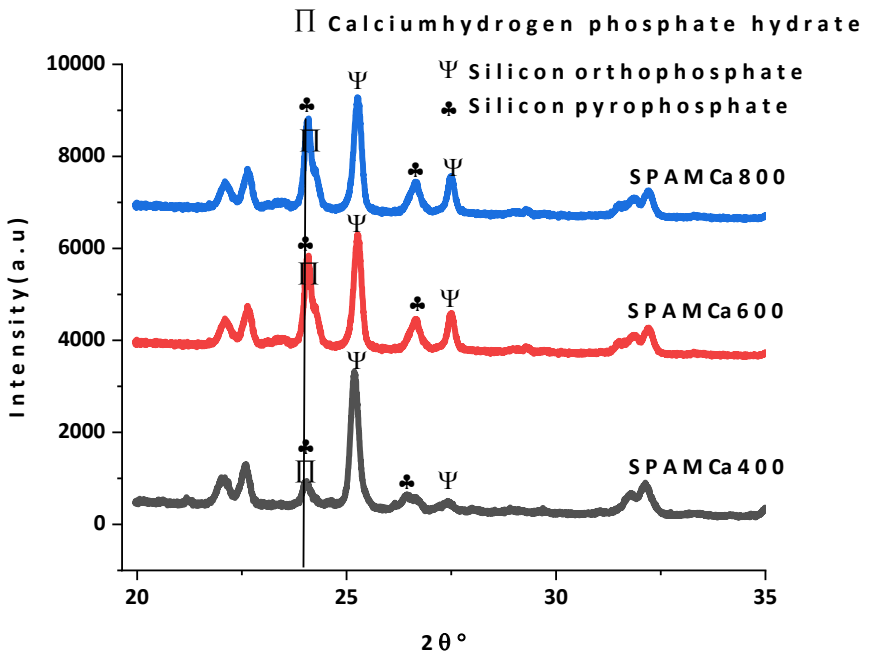


Figure 3.18 Influence of calcination temperature on the crystalline phase transformations of the calcium promoted SPA catalysts synthesized from mined kieselguhr.

Calcium reacted with phosphoric acid to form calcium hydrogen phosphate this resulted in a minority additional calcium hydrogen phosphate hydrate phase being identified. On higher calcination temperature, a peak shift to the higher two theta angle was reported in Figure 3.18 above. The silicon pyrophosphate peak two-theta angle at 400 ^{o}C calcination temperature was 23.9 ^{o} which shifted to 24.1 ^{o} on 600 ^{o}C and 800 ^{o}C calcination temperatures. The calcium doping could result in crystallographic distortion, causing a change in unit cell geometry, thus a change in atomic coordinates within a unit cell, the data is suggesting that this may have occurred [63].

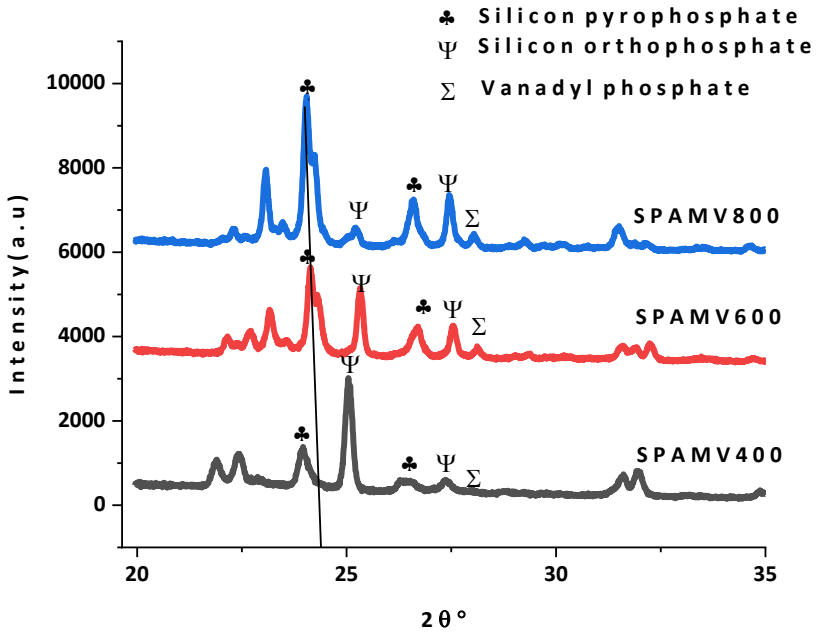


Figure 3.19. Effect of calcination temperature on the crystalline phase transformations of the vanadium promoted SPA catalysts synthesized from mined kieselguhr.

On promoting SPA catalyst with vanadium, vanadium reacted with phosphoric acid to form an additional vanadium pyrophosphate phase. However, a peak shift at a higher calcination temperature was observed. At 400 ^{o}C the silicon pyrophosphate peak is at the two-theta angle of 23.9 ^{o} which shifted on calcination to 24.3 ^{o}. Vanadium promotion caused the SPA catalyst compositional change, which could result in a change in lattice parameters which was further affected by calcination at a higher temperature. The data is suggesting that this could have happened, however, a peak shift in the XRD diffractogram of 0.4 ^{o} is within a margin of error[64].

The XRD patterns of the synthesized SPA catalyst using crystalline synthetic kieselguhr are shown in Figures 3.20 and 3.21 below. The objective was to investigate the effect of synthetic kieselguhr on SPA catalysts crystalline phases. Catalyst SPAST series reported silicon-orthophosphate PDF 00-022-1380 and silicon-pyrophosphate PDF 00-022-1320 crystalline phases and a further calcium hydrogen phosphate hydrate crystalline phase PDF 00 -009 - 0347 was reported for the calcium promoted SPASCa catalyst.

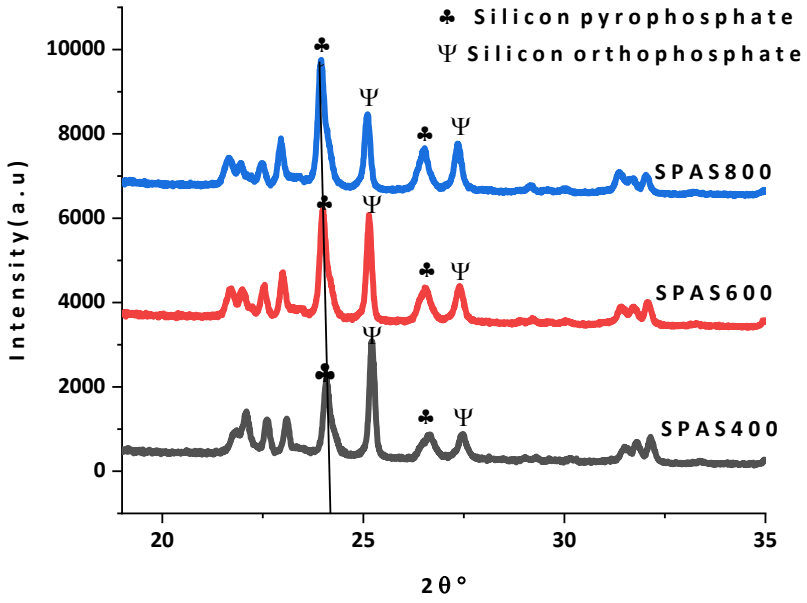


Figure 3.20 Influence of calcination temperature on the crystalline phases of the SPA catalysts synthesized from synthetic kieselguhr.

The XRD diffractogram of the SPA catalysts synthesized from crystalline synthetic kieselguhr Figure 3.20 above has shown similar silicon phosphate phases in comparison to the diffractogram of the SPA catalysts synthesized from amorphous mined kieselguhr Figure 3.17. The same trend of increase in silicon pyrophosphate with the increase in calcination temperature was also observed.

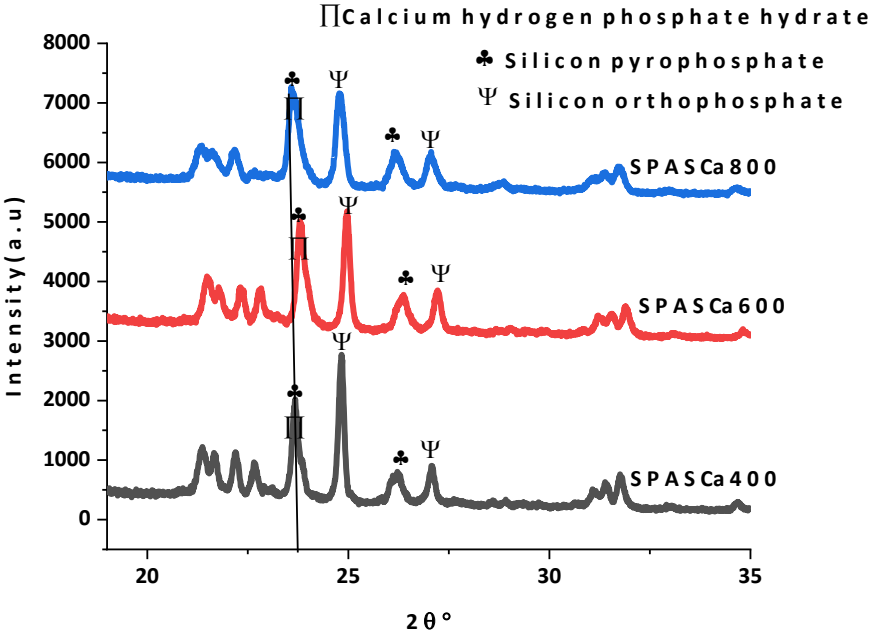


Figure 3.21 Influence of calcination temperature on the crystalline phase transformations of the calcium promoted SPA catalysts synthesized from crystalline synthetic kieselguhr.

Calcination temperature has shown to have a similar effect on calcium promoted SPA catalysts synthesized from crystalline synthetic kieselguhr compared to calcium promoted SPA catalysts synthesized from amorphous kieselguhr Figure 3.18. The same trend of peak shift towards the higher two theta angle was observed with the same explanation as that of calcium promoted SPA catalysts synthesized from amorphous kieselguhr Figure 3.18.

Conventionally, knowledge of the crystallite size of the catalytic material provides the basis for the design of an optimal catalyst structure. In this work, the Scherrer equation was used to calculate the crystallite size. However, the basis of the Scherrer equation is that the width of a powder X-ray diffraction reflection relates to coherent diffraction domain size which is perpendicular to the diffraction plane being analyzed[65]. Therefore, it is the crystalline domain size, which is being determined in Equation 3.4 below.

$$d = \frac{K\lambda}{\beta COS\theta} \qquad \text{Equation} \qquad 3.4$$

Where, d is the coherent diffraction domain size, λ is the wavelength of the X-ray source used, β is the reflection width (2Θ), Θ is the Bragg angle in radians and K is the shape constant assumed to be spherical[66].

The reflection width β can be affected by instrumental broadening[67]. Quartz standard reference material data was used to calculate structural reflection width.

$$\beta_{structural} = \beta_{observed} - \beta_{standard} \qquad \text{Equation} \qquad 3.5$$

K = 0.94 was used assuming spherical crystallite shape, the reflection width calculated according to equation 5 is independent of the broadening effect and was used to calculate crystallite size.

Table 3.8 below shows the crystallite data from the study of the SPAM and SPAS catalysts series done in this work.

Table 3.8 Influence of calcination temperature on crystallite size of the SPA catalyst synthesized from amorphous and crystalline kieselguhr.

Calcination temperature/ ^{o}C	SPAM Catalyst	SPAS Catalyst
	Average crystallite size/nm	
400	59 ± 2	68 ± 2
500	110 ± 2	98 ± 2
600	110 ± 3	180 ± 4
700	110 ± 3	179 ± 4
800	126 ± 3	177 ± 3

The SPAS catalyst calcined at 400 ^{o}C has a larger crystallite size compared to catalyst SPAM catalyst Table 3.8 above. A general increase in crystallite size with an increase in calcination temperature was reported, however, the catalyst synthesized from crystalline kieselguhr (SPAS) reported bigger crystallites than the catalyst synthesized from amorphous kieselguhr (SPAM).

This is associated with the formation of more crystals in the catalyst as a result of an appropriate environment for crystal growth[68]. The crystallization process begins with nucleation and aggregation of viable nuclei with crystalline structure followed by crystal growth which proceeds via the addition of crystal slabs and crystal oligomers[69]. Synthetic crystalline kieselguhr has crystal nuclei which provide crystalline seeds for the development of new crystal development this phenomenon enhances crystal growth[70].

Table 3.9 Variation in crystallite size of the SPA catalysts synthesized from amorphous and crystalline synthetic kieselguhr.

Catalyst	Average crystallite size(nm)
SPAM400	59 ± 2
SPAS400	68 ± 2
SPAM600	110 ± 3
SPAS600	180 ± 4
SPAM800	126 ± 3
SPAS800	177 ± 3

The variation in crystallite sizes of the SPA catalyst synthesized from synthetic and amorphous kieselguhr indicate that there is variation in the pore volume of the catalysts synthesized from the two silica sources[71]. Aggregation of bigger crystallites promotes higher catalyst porosity compared to the aggregation of small crystallite size which fosters low catalyst pore volume[72].

Table 3.9 above, the crystallite size of the catalyst increases with an increase in calcination temperature, however, for catalyst SPAS, the crystallite size tailed off at 600 ^{o}C which implies that the crystal structure is stable at that temperature range[73].

In this work, the percentage total relative crystallinity is the sum of all the silicon phosphate phases identified compared to the crystalline phase of the commercial reference material (quartz standard) with a peak at 21.3 º two-theta and a d-spacing of 4.168.

Quantification of the crystalline phases was calculated according to the following formulae.

$$\% \text{ Silicon orthophosphate } = \frac{net\ area\ of\ the\ most\ intense\ silicon\ orthophosphate\ peak}{net\ area\ of\ the\ \ quartz\ reference\ peak} \times 100 \qquad 3.6$$

$$\% \text{ Silicon pyrophosphate} = \frac{net\ area\ of\ \ the\ most\ intense\ silicon\ pyrophosphate\ peak}{net\ area\ of\ the\ quartz\ reference\ peak} \times 100 \qquad 3.7$$

$$\text{Net area} = (FWHM\ \times Peak\ height) \qquad 3.8$$

Where FWHM is full with at half maximum of a peak at 2Ɵ of 21.3 º and d-spacing of 4.168 for quartz standard, 25 º and d-spacing of 3.579 for silicon orthophosphate and 24 º and d-spacing of 3.643 for silicon pyrophosphate. Equation 3.6 was used for the calculation of the % calcium phosphate silicate phase.

$$\% \text{ Total crystallinity } = \% \text{ Silicon orthophosphate} + \% \text{ Silicon pyrophosphate}^{74} \qquad 3.9$$

A general increase in relative total crystallinity for catalyst synthesized from synthetic kieselguhr for both unpromoted and calcium promoted SPA catalyst was reported, Figure 3.23 below.

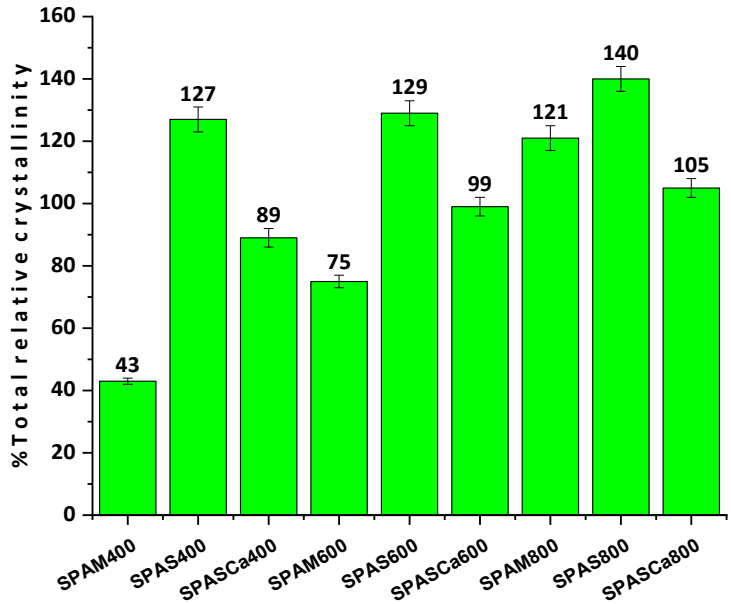


Figure 3.22 Influence of calcination temperature on total relative crystallinity(all results are reported in percentages), standard error per measurement of 3 % according to the method of analysis was reported[74].

The SPA catalyst synthesized from mined kieselguhr shows lower relative total crystallinity at 400 ^{o}C calcination temperature which is 43.1 % compared to 127.1 % for SPAS catalyst. This should be attributed to the fact that mined kieselguhr was amorphous compared to crystalline synthetic kieselguhr. Hence, nucleation is the first step of crystallization in SPA catalyst synthesized from amorphous kieselguhr[75]. Whereas the SPA catalyst synthesized from crystalline kieselguhr, calcination at 400 ^{o}C would see crystal growth and crystal propagation, to investigate further this hypothesis TEM characterization was performed and will be explained in Chapter 4.

The total relative crystallinity results show that there is a relative crystallinity benefit to using synthetic kieselguhr for the synthesis of SPA catalyst which is 1.5 fold higher than the crystallinity of catalyst synthesized from amorphous kieselguhr. The improved relative crystallinity goes a long way in positively improving the crushing strength of the SPA catalysts[76]. Coetzee et al, reported that SPA catalyst with high silicon pyrophosphate has high crushing strength[77]. The silicon pyrophosphate results of the SPA catalyst calcined at 400 ^{o}C for the catalyst synthesized from the crystalline kieselguhr is higher, 34.6 % compared to 7.6 % of the catalyst synthesized from amorphous kieselguhr.

According to Jichang Zhang et al, a SPA catalyst with high silicon pyrophosphate content has the best catalytic activity and lifetime for propene oligomerization[14]. Indeed the SPA catalyst synthesized from crystalline kieselguhr should have high catalytic activity and lifetime because it posses a very high silicon pyrophosphate content.

3.6 References:

(1) Ipatieff, V. N.; Corson, B. B. Gasoline from Ethylene by Catalytic Polymerization. *Ind. Eng. Chem.* **1936**. https://doi.org/10.1021/ie50319a027.

(2) De Klerk, A.; Leckel, D. O.; Prinsloo, N. M. Butene Oligomerization by Phosphoric Acid Catalysis: Separating the Effects of Temperature and Catalyst Hydration on Product Selectivity. *Ind. Eng. Chem. Res.* **2006**. https://doi.org/10.1021/ie060207m.

(3) De Klerk, A.; Engelbrecht, D. J.; Boikanyo, H. Oligomerization of Fischer-Tropsch Olefins: Effect of Feed and Operating Conditions on Hydrogenated Motor-Gasoline Quality. In *Industrial and Engineering Chemistry Research*; 2004. https://doi.org/10.1021/ie0495675.

(4) Ipatieff, V. N.; Schmerling, L. Ethylation of Benzene in Presence of Solid Phosphoric Acid. *Ind. Eng. Chem.* **1946**, *38* (4), 400–402. https://doi.org/10.1021/ie50436a017.

(5) Yu Shen, C.; Louis, S. *United States Patent Office 3,371,992 Formation of Crystalline Pyrophosphoric Acid*; 1968.

(6) Gerber, A. B.; Miles, F. T. Determination of Ortho-, Pyro-, and Metaphosphoric Acids: By Colorimetric PH Titrations. *Ind. Eng. Chem. - Anal. Ed.* **1938**, *10* (9), 519–524. https://doi.org/10.1021/ac50125a007.

(7) Ohtsuka, H.; Aomura, K. Activation of Solid Phosphoric Acid by Heat Treatment. *Bull. Japan Pet. Inst.* **1962**, *4*, 3–14. https://doi.org/10.1627/jpi1959.4.3.

(8) Yuan, P.; Wu, D. Q.; Chen, Z.; Chen, Z. W.; Lin, Z. Y.; Diao, G. Y.; Peng, J. L. H-1 MAS NMR Spectra of Hydroxyl Species on Diatomite Surface G-4601-2010. *CHINESE Sci. Bull.* **2001**.

(9) Murashov, V.; Harper, M.; Demchuk, E. Impact of Silanol Surface Density on the Toxicity of Silica Aerosols Measured by Erythrocyte Haemolysis. *J. Occup. Environ. Hyg.* **2006**, *3* (12), 718–723. https://doi.org/10.1080/15459620601015950.

(10) *United States Patent (19) Heymer et Al. 54) Process for the Manufacture Of*; 1972.

(11) Sawant, A. D.; Raut, D. G.; Deorukhkar, A. R.; Desai, U. V.; Salunkhe, M. M. Silica Supported Orthophosphoric Acid (H 3PO 4. SiO 2): A Green, Heterogeneous Catalyst for Solvent-Free Oxathioacetalization of Aldehydes. *Green Chem. Lett. Rev.* **2011**. https://doi.org/10.1080/17518253.2010.544682.

(12) Chakrabarty, M.; Mukherjee, R.; Mukherji, A.; Arima, S.; Harigaya, Y. Phosphoric Acid-on-Silica Gel: A Green Catalyst for the Synthesis of Symmetrical Bis(Indolyl)Alkanes. *Heterocycles* **2006**. https://doi.org/10.3987/COM-06-10783.

(13) Schwarzer, R.; du Toit, E.; Nicol, W. Solid Phosphoric Acid Catalysts: The Effect of Free Acid Composition on Selectivity and Activity for 1-Hexene Dimerisation. *Appl. Catal. A Gen.* **2009**, *369* (1–2), 83–89. https://doi.org/10.1016/j.apcata.2009.09.002.

(14) Zhang, J.; Yan, Y.; Chu, Q.; Feng, J. Solid Phosphoric Acid Catalyst for Propene Oligomerization : Effect of Silicon Phosphate Composition. *Fuel Process. Technol.* **2015**, *135*, 2–5. https://doi.org/10.1016/j.fuproc.2014.09.007.

(15) Cavani, F.; Girotti, G.; Terzoni, G. Effect of Water in the Performance of the 'Solid Phosphoric Acid' Catalyst for Alkylation of Benzene to Cumene and for Oligomerization of Propene. *Appl. Catal. A, Gen.* **1993**. https://doi.org/10.1016/0926-860X(93)80083-3.

(16) Duduk, A. United States Patent: 8257554 United States Patent: 8257554. **1972**, *1* (12), 1–8.

(17) Jameson, R. F. The Composition of the 'Strong' Phosphoric Acids. *J. Chem. Soc.* **1959**. https://doi.org/10.1039/JR9590000752.

(18) Makart, H. Untersuchungen an Siliciumphosphaten. *Helv. Chim. Acta* **1967**, *50* (2), 399–405. https://doi.org/10.1002/hlca.19670500208.

(19) Cloete, J. Determination of Crushing Strength. *Clariant Sasol Catal. Intern. Commun.* **2018**.

(20) Ratnawulan; Fauzi, A.; AE, S. H. Effect of Calcination Temperature on Phase Transformation and Crystallite Size of Copper Oxide (CuO) Powders. *AIP Conf. Proc.* **2017**,

1868 (1), 060009. https://doi.org/10.1063/1.4995173.

(21) Liu, Q.; Liu, W.; Lü, L.; Li, R.; Liang, B.; Yue, H.; Tang, S.; Li, C. Study on Reactions of Gaseous P2O5 with Ca3(PO4)2 and SiO2 during a Rotary Kiln Process for Phosphoric Acid Production. *Chinese J. Chem. Eng.* **2018**, *26* (4), 795–805. https://doi.org/10.1016/j.cjche.2017.11.016.

(22) Kiyomi, O.; Kazuhisa, M.; Nurunnabi, M.; Yangyong, L.; Isao, T.; Megumu, I. Effects of Pore Size of Ru SiO 2 Catalysts Prepared by Alkoxide Method on Fischer-Tropsch Reaction. *J. Japan Pet. Inst.* **2007**, *50* (6), 349–353.

(23) Gu, T.; Chen, F.; Shen, Q.; Zhang, L. Low-Temperature Preparation of Porous SiC Ceramics Using Phosphoric Acid as a Pore-Forming Agent and a Binder. *Ceram. Int.* **2019**, *45* (13), 16470–16475. https://doi.org/10.1016/j.ceramint.2019.05.179.

(24) Shcherban, N. D.; Filonenko, S. M.; Yaremov, P. S.; Nauky, P. Micro-Mesoporous Zeolite-like Matrices. **2017**, *52* (6), 356–361. https://doi.org/10.1007/s11237-017-9490-1.

(25) McDaniel, M. P. Influence of Catalyst Porosity on Ethylene Polymerization. *ACS Catal.* **2011**, *1* (10), 1394–1407. https://doi.org/10.1021/CS2003033.

(26) Zakeri, M.; Samimi, A.; Shafiee Afarani, M.; Salehirad, A. Effects of Porosity and Pore Size Distribution on Mechanical Strength Reliability of Industrial-Scale Catalyst during Preparation and Catalytic Test Steps. *Part. Sci. Technol.* **2018**, *36* (1), 96–103. https://doi.org/10.1080/02726351.2016.1220437.

(27) Cebeci, Ö. Mercury Intrusion Porosimetry Theory and Its Application to Air-Entrained Cement Pastes and Mortars. *Retrosp. Theses Diss.* **1977**. https://doi.org/https://doi.org/10.31274/rtd-180813-4556.

(28) Borja, R. I. Multiscale Modeling of Pore Collapse Instability in High-Porosity Solids. In *III European Conference on Computational Mechanics*; Springer Netherlands, 2008; pp 10–10. https://doi.org/10.1007/1-4020-5370-3_10.

(29) Cheng, L. R.; Chen, R.; Shi, H. J.; Lu, F. Y. The Pore Collapse 'Hot-Spots' Model Coupled

with Brittle Damage for Solid Explosives. *Shock Vib.* **2014**, *2014*. https://doi.org/10.1155/2014/972414.

(30) Shonnard, D. Synergistic Effects between Hydrolysis Time and Microporous Structure in Poplar. *ACS Sustain. Chem. Eng.* **2019**, *7*, 12920–12929. https://doi.org/10.1021/acssuschemeng.9b01926.

(31) Liebau, F.; Bissert, G.; Köppen, N. Synthese Und Kristallographische Eigenschaften Einiger Phasen Im System SiO2–P2O5. *ZAAC - J. Inorg. Gen. Chem.* **1968**, *359* (3–4), 113–134. https://doi.org/10.1002/zaac.19683590302.

(32) Dorozhkin, S. V. Surface Reactions of Apatite Dissolution. *J. Colloid Interface Sci.* **1997**. https://doi.org/10.1006/jcis.1997.4942.

(33) Leinenweber, K.; Stearns, L. A.; Nite, J. M.; Németh, P.; Groy, T. L. Structure of a New Form of Silicon Phosphate (SiP 2O 7) Synthesized at High Pressures and Temperatures. *J. Solid State Chem.* **2012**, *190*, 221–225. https://doi.org/10.1016/j.jssc.2012.02.031.

(34) Gulati, S. T. Design Considerations for Advanced Ceramic Catalyst Supports. In *SAE Technical Papers*; 2000. https://doi.org/10.4271/2000-01-0493.

(35) Lei, G.; Cao, N.; Mcpherson, B. J.; Liao, Q.; Chen, W. Open a Novel Analytical Model for Pore Volume Compressibility of Fractal Porous Media. *Sci. Rep.* **2019**, *C*, 1–11. https://doi.org/10.1038/s41598-019-51091-2.

(36) Villarroel Rocha, J.; Barrera, D.; Sapag, K. Improvement in the Pore Size Distribution for Ordered Mesoporous Materials with Cylindrical and Spherical Pores Using the Kelvin Equation. In *Topics in Catalysis*; 2011. https://doi.org/10.1007/s11244-011-9631-z.

(37) Guo, A.; Roso, M.; Modesti, M.; Maire, E.; Adrien, J.; Colombo, P. Characterization of Porosity, Structure, and Mechanical Properties of Electrospun SiOC Fiber Mats. *J. Mater. Sci. 2015 5012* **2015**, *50* (12), 4221–4231. https://doi.org/10.1007/S10853-015-8973-5.

(38) Giesche, H. Mercury Porosimetry. In *Handbook of Porous Solids*; Wiley-VCH Verlag GmbH, 2008; pp 309–351. https://doi.org/10.1002/9783527618286.ch9.

(39) Lenormand, R. Interpretation of Mercury Injection Curves to Derive Pore Size Distribution. *Int. Symp. Soc. Core Anal.* **2003**, *Internatio*, SCA2003-52.

(40) Rigby, S. P.; Chigada, P. I.; Wang, J.; Wilkinson, S. K.; Bateman, H.; Al-duri, B.; Wood, J.; Bakalis, S.; Miri, T. Improving the Interpretation of Mercury Porosimetry Data Using Computerised X-Ray Tomography And. *Chem. Eng. Sci.* **2019**, *66* (11), 2328–2339. https://doi.org/10.1016/j.ces.2011.02.031.

(41) Medeiros-Costa, I. C.; Laroche, C.; Pérez-Pellitero, J.; Coasne, B. Characterization of Hierarchical Zeolites: Combining Adsorption/Intrusion, Electron Microscopy, Diffraction and Spectroscopic Techniques. *Microporous Mesoporous Mater.* **2019**, *287*, 167–176. https://doi.org/10.1016/j.micromeso.2019.05.057.

(42) Kruk, M.; Jaroniec, M.; Sayari, A. Application of Large Pore MCM-41 Molecular Sieves to Improve Pore Size Analysis Using Nitrogen Adsorption Measurements. *Langmuir* **1997**. https://doi.org/10.1021/la970776m.

(43) Ding, Y.; Zhao, C.; Li, Y.; Ma, Z.; Lv, X. Effect of Calcination Temperature on the Structure and Catalytic Performance of the Cu-Mcm-41 Catalysts for the Synthesis of Dimethyl Carbonate. *Quim. Nova* **2018**, *41* (10), 1156–1161. https://doi.org/10.21577/0100-4042.20170291.

(44) Jimeńez-García, G.; De Lasa, H.; Quintana-Solorźano, R.; Maya-Yescas, R. Catalyst Activity Decay Due to Pore Blockage during Catalytic Cracking of Hydrocarbons. *Fuel* **2013**, *110*, 89–98. https://doi.org/10.1016/j.fuel.2012.10.082.

(45) Sing, K. S. W. Assessment of Surface Area by Gas Adsorption. In *Adsorption by Powders and Porous Solids: Principles, Methodology and Applications: Second Edition*; 2013. https://doi.org/10.1016/B978-0-08-097035-6.00007-3.

(46) Thommes, M.; Kaneko, K.; Neimark, A. V.; Olivier, J. P.; Rodriguez-Reinoso, F.; Rouquerol, J.; Sing, K. S. W. Physisorption of Gases, with Special Reference to the Evaluation of Surface Area and Pore Size Distribution (IUPAC Technical Report). *Pure Appl. Chem.* **2015**, *87* (9–10), 1051–1069. https://doi.org/10.1515/pac-2014-1117.

(47) Leng, L.; Xiong, Q.; Yang, L.; Li, H.; Zhou, Y.; Zhang, W.; Jiang, S.; Li, H.; Huang, H. An Overview on Engineering the Surface Area and Porosity of Biochar. *Sci. Total Environ.* **2021**, *763*, 144204. https://doi.org/10.1016/J.SCITOTENV.2020.144204.

(48) Ye, G.; Zhou, X.; Coppens, M.-O.; Zhou, J.; Yuan, W.; Ye, G. Influence of Catalyst Pore Network Structure on the Hysteresis of Multiphase Reactions. *AIChE J.* **2016**. https://doi.org/10.1002/aic.15415.

(49) Thommes, M.; Kaneko, K.; Neimark, A. V.; Olivier, J. P.; Rodriguez-Reinoso, F.; Rouquerol, J.; Sing, K. S. W. Physisorption of Gases, with Special Reference to the Evaluation of Surface Area and Pore Size Distribution (IUPAC Technical Report). *Pure Appl. Chem.* **2015**, *87* (9–10), 1051–1069. https://doi.org/10.1515/pac-2014-1117.

(50) Thommes, M. Physical Adsorption Characterization of Nanoporous Materials. *Chemie Ing. Tech.* **2010**, *82* (7), 1059–1073. https://doi.org/10.1002/CITE.201000064.

(51) Lastoskie, C.; Gubbins, K. E.; Quirke, N. Pore Size Distribution Analysis of Microporous Carbons: A Density Functional Theory Approach. *J. Phys. Chem.* **1993**, *97* (18), 4786–4796. https://doi.org/10.1021/j100120a035.

(52) Grosman, A.; Ortega, C. Nature of Capillary Condensation and Evaporation Processes in Ordered Porous Materials. *Langmuir* **2005**, *21* (23), 10515–10521. https://doi.org/10.1021/la051030o.

(53) Morishige, K.; Tarui, N. Capillary Condensation of Nitrogen in Ordered Mesoporous Silica with Bicontinuous Gyroid Structure. *J. Phys. Chem. C* **2007**, *111* (1), 280–285. https://doi.org/10.1021/jp064946s.

(54) Ye, G.; Sun, Y.; Zhou, X.; Zhu, K.; Zhou, J.; Coppens, M. Method for Generating Pore Networks in Porous Particles of Arbitrary Shape , and Its Application to Catalytic Hydrogenation of Benzene. *Chem. Eng. J.* **2017**, *329*, 56–65. https://doi.org/10.1016/j.cej.2017.02.036.

(55) Rajagopalan, K.; Luss, D. Influence of Catalyst Pore Size on Demetallation Rate. *Ind. Eng.*

Chem. Process Des. Dev. **1979**, *18* (3), 459–465. https://doi.org/10.1021/i260071a019.

(56) Ding, L.; Gao, H.; Xie, F.; Li, W.; Bai, H.; Li, L. Porosity-Enhanced Polymers from Hyper-Cross-Linked Polymer Precursors. *Macromolecules* **2017**, *50* (3), 956–962. https://doi.org/10.1021/ACS.MACROMOL.6B02715.

(57) Ye, G.; Wang, H.; Zhou, X.; Keil, F. J.; Coppens, M.; Yuan, W. Optimizing Catalyst Pore Network Structure in the Presence of Deactivation by Coking. *AIChE J.* **2019**, *65* (10), e16687. https://doi.org/10.1002/aic.16687.

(58) Krawietz, T. R.; Lin, P.; Lotterhos, K. E.; Torres, P. D.; Barich, D. H.; Clearfield, A.; Haw, J. F. Solid Phosphoric Acid Catalyst: A Multinuclear NMR and Theoretical Study. *J. Am. Chem. Soc.* **1998**, *120* (33), 8502–8511. https://doi.org/10.1021/ja9813461.

(59) Poojary, D. M.; Borade, R. B.; Campbell, F. L.; Clearfield, A. Crystal Structure of Silicon Pyrophosphate (Form I) from Powder Diffraction Data. *J. Solid State Chem.* **1994**, *112* (1), 106–112. https://doi.org/10.1006/jssc.1994.1273.

(60) Poojary, D. M.; Borade, R. B.; Clearfield, A. Structural Characterization of Silicon Orthophosphate. *Inorganica Chim. Acta* **1993**, *208* (1), 23–29. https://doi.org/10.1016/S0020-1693(00)82879-0.

(61) Özdemir, H.; Öksüzömer, M. A. F.; Gürkaynak, M. A. Effect of the Calcination Temperature on Ni / MgAl 2 O 4 Catalyst Structure and Catalytic Properties for Partial Oxidation of Methane. *Fuel* **2014**, *116*, 63–70. https://doi.org/10.1016/j.fuel.2013.07.095.

(62) Wang, R.; Wan, J.; Li, Y.; Sun, H. An Improvement of MCM-41 Supported Phosphoric Acid Catalyst for Alkylation Desulfurization of Fluid Catalytic Cracking Gasoline. *Fuel* **2015**. https://doi.org/10.1016/j.fuel.2014.11.093.

(63) Huhti, A.-L.; Gartaganis, P. A. The Composition of the Strong Phosphoric Acids. *Can. J. Chem.* **1956**. https://doi.org/10.1139/v56-102.

(64) Mittemeijer, E. J.; Welzel, U. The 'State of the Art' of the Diffraction Analysis of Crystallite

Size and Lattice Strain. *Zeitschrift fur Krist.* **2008**, *223* (9), 552–560. https://doi.org/10.1524/ZKRI.2008.1213.

(65) J. S. J. Hargreaves. Powder X-Ray Diffraction and Heterogeneous Catalysis. *Crystallogr. Rev.* **2005**, *11* (1), 21–34. https://doi.org/10.1080/08893110500078324.

(66) Ingham, B.; Toney, M. F. X-Ray Diffraction for Characterizing Metallic Films. In *Metallic Films for Electronic, Optical and Magnetic Applications: Structure, Processing and Properties*; Elsevier Ltd., 2013; pp 3–38. https://doi.org/10.1533/9780857096296.1.3.

(67) Monshi, A.; Foroughi, M. R.; Monshi, M. R. Modified Scherrer Equation to Estimate More Accurately Nano-Crystallite Size Using XRD. *World J. Nano Sci. Eng.* **2012**, *02* (03), 154–160. https://doi.org/10.4236/wjnse.2012.23020.

(68) Menad, K.; Feddag, A.; Rubenis, K. Synthesis and Study of Calcination Temperature Influence on the Change of Structural Properties of the LTA Zeolite. *Rasayan J. Chem* **2016**, *9*, 788–797.

(69) Bozhilov, K. N.; Valtchev, V. Zeolite Crystal Growth Analysis by Dissolution. *Microsc. Microanal.* **2019**, *25* (S2), 816–817. https://doi.org/10.1017/s1431927619004811.

(70) Richardson, J. F.; Harker, J. H.; Backhurst, J. R. *Chemical Engineering: Particle Technology and Separation Processes: Fifth Edition*; Elsevier Inc., 2013; Vol. 2. https://doi.org/10.1016/C2009-0-25733-3.

(71) Sistani, A.; Saghatoleslami, N.; Nayebzadeh, H. Influence of Calcination Temperature on the Activity of Mesoporous CaO/TiO2–ZrO2 Catalyst in the Esterification Reaction. *J. Nanostructure Chem.* **2018**, *8* (3), 321–331. https://doi.org/10.1007/s40097-018-0276-3.

(72) da Silva, L. M.; de Oliveira Santiago Santos, G.; de Salles Pupo, M. M.; Eguiluz, K. I. B.; Salazar-Banda, G. R. Influence of Heating Rate on the Physical and Electrochemical Properties of Mixed Metal Oxides Anodes Synthesized by Thermal Decomposition Method Applying an Ionic Liquid. *J. Electroanal. Chem.* **2018**, *813*, 127–133. https://doi.org/10.1016/j.jelechem.2018.02.026.

(73) Chen, X.; Qian, Y.; Chen, Z.; Gui, Z. Effects of Ionic Radius on Structure and Superconductivity for High-Tc Oxide Superconductors. *Phys. Status Solidi* **1992**, *130* (2), 415–420. https://doi.org/10.1002/pssa.2211300219.

(74) Matabal, P. QCM 06 Determination of Relative Crystallinity by XRD Diffraction. *Clariant Sasol Catal. Intern. Commun.* **2019**, *2*.

(75) Tong, D.-G.; Chu, W.; Luo, Y.-Y.; Ji, X.-Y.; He, Y. Effect of Crystallinity on the Catalytic Performance of Amorphous Co-B Particles Prepared from Cobalt Nitrate and Potassium Borohydride in the Cinnamaldehyde Hydrogenation. *J. Mol. Catal. A Chem.* **2007**, *265*, 195–204. https://doi.org/10.1016/j.molcata.2006.10.032.

(76) Egloff, G.; Jones, E. K. New and Advanced Developments in Tetramer, Cumene and Motor Polymer Manufacture. In *World Petroleum Congress Proceedings*; 1955.

(77) Coetzee, J. H.; Mashapa, T. N.; Prinsloo, N. M.; Rademan, J. D. An Improved Solid Phosphoric Acid Catalyst for Alkene Oligomerization in a Fischer-Tropsch Refinery. *Appl. Catal. A Gen.* **2006**, *308*, 204–209. https://doi.org/10.1016/j.apcata.2006.04.023.

Chapter 4

4. Unravelling the morphology of the synthesized SPA catalysts.

4.1 Introduction

Solid phosphoric acid catalyst properties such as activity, selectivity and deactivation depend on the catalyst microstructure[1]. The catalyst is characterized by macropores which provide sufficient pore surface area for the polymerization of olefins[2]. The pore size influences the adsorbate and catalyst interaction, macropores foster catalysis of bulky reactants with micropores favouring the reaction of non-bulky compounds consequently increasing the catalyst selectivity, reactivity and lifetime[3,4]. These physical parameters of the SPA catalyst are somewhat related to the morphology of the catalyst[5].

Recent developments in the synthesis of nanoscale materials and technologies have given an edge to research for the development of catalysis performance by further understanding the reactivity at the nanoscale[6,7]. Based on industrial results, the performance of the SPA catalyst in oligomerization reactions is firmly linked to its morphology and structure[8]. Knowledge and understanding of these fundamental topics in SPA catalysis are crucial in the advancement of the oligomerization process[9]. Further research is required to increase the ongoing efforts to understand and optimize the structure of the SPA catalysts[10].

The SPA catalyst studied in this chapter was synthesized using the impregnation method as stated in Chapter 2. This synthesis technique has high reproducibility and promotes the homogeneous distribution of silicon and phosphorus atoms on the catalyst[11]. These elements form the backbone of the SPA catalyst[12]. High homogeneity in silicon and phosphorus enables control over the resulting polymorph of the crystalline phases synthesized[13]. This is crucial in controlling the acidity of the catalyst[14] since a high amount of phosphorus translates into a high content of acidic species as a result of a 1:3 ratio of phosphorus to hydrogen in phosphoric acid (H_3PO_4) used in the synthesis of the SPA catalyst[15].

4.2 Crystal structure of SPA catalysts synthesized from mined kieselguhr.

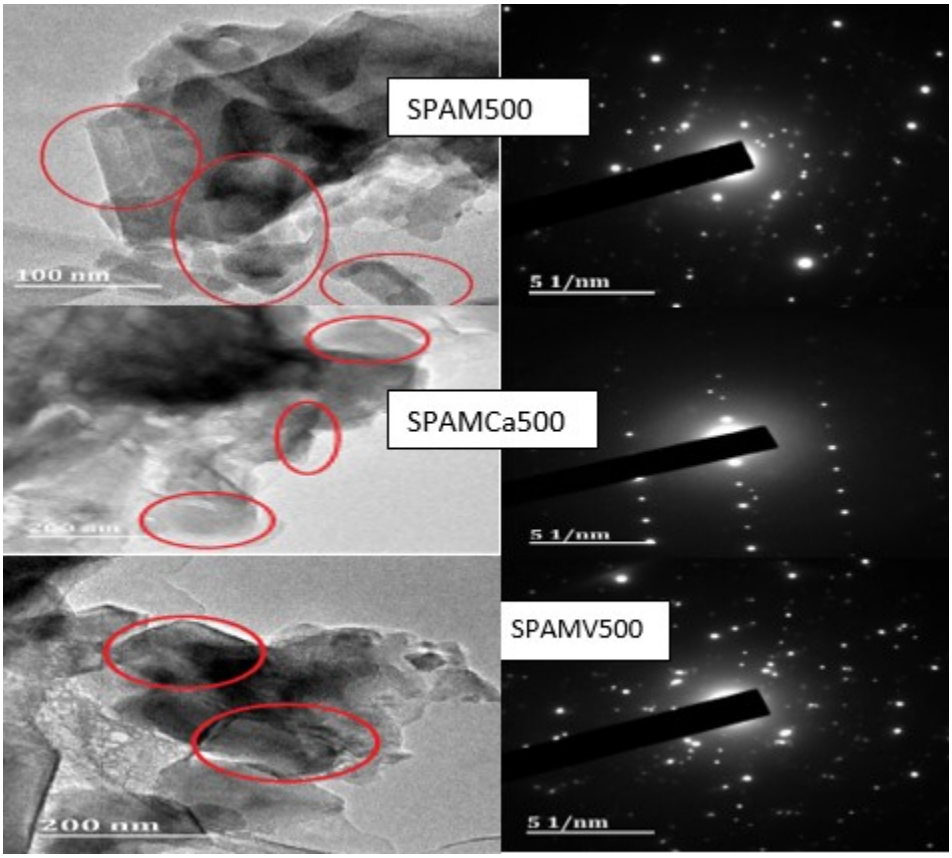


Figure 4.1 Microstructure (left side) and SAED (right side) of the catalysts synthesized from amorphous kieselguhr. The catalyst showed individual grains encircled in red.

Selected area electron diffraction (SAED) in Figure 4.1 above shows spots emanating from a single crystalline solid phosphoric acid catalyst. This means that the synthesized SPAM500, SPAMCa500 and SPAMV500 catalysts were a single crystalline solid. This implies that the crystal lattice of the entire samples of the synthesized SPA catalyst was continuous. This agrees with the data reported by Clearfield and his coworkers.

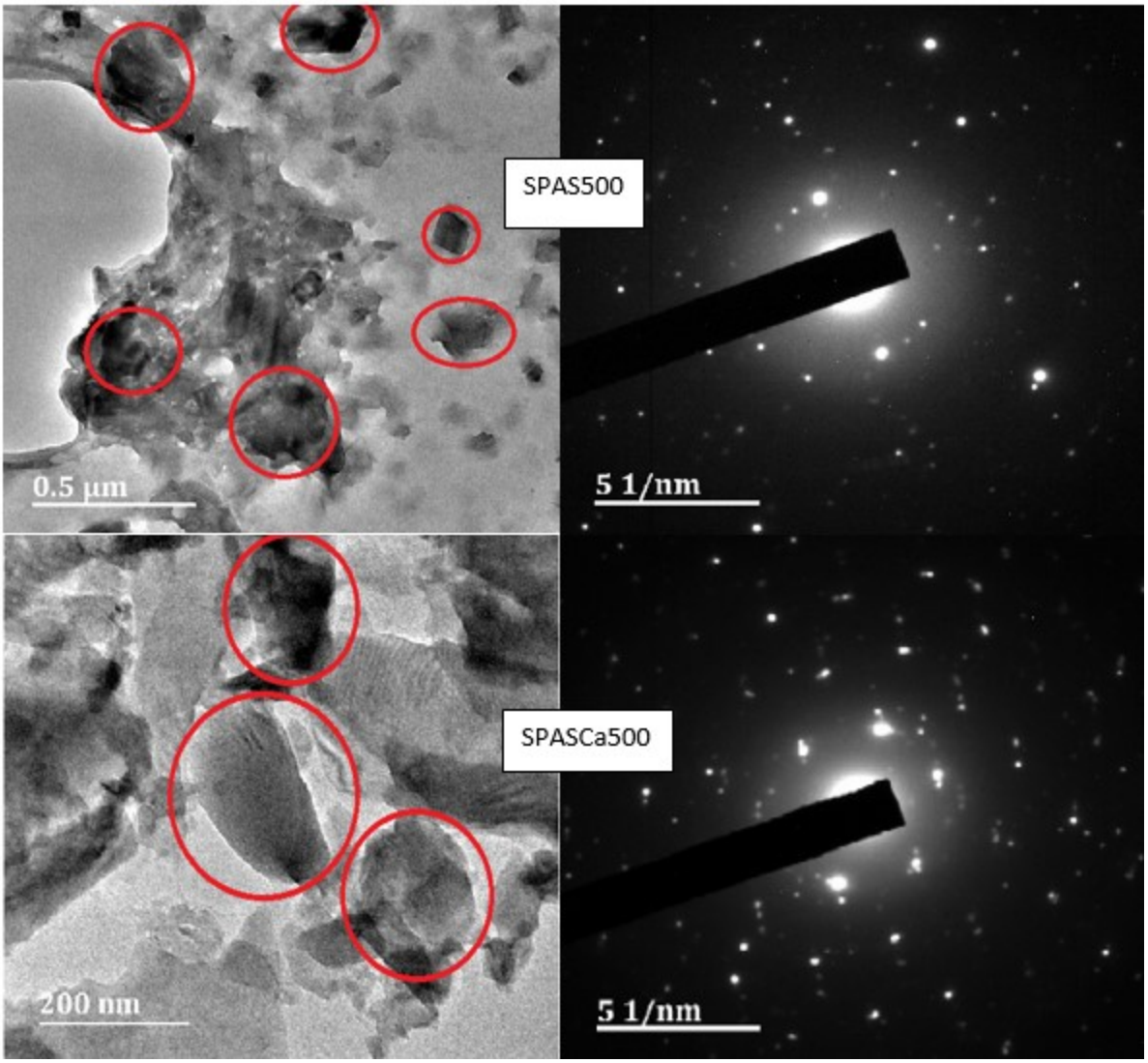


Figure 4.2 Microstructure and SAED of the SPAS500 and SPASCa500 catalysts synthesized from crystalline synthetic kieselguhr (single grains encircled in red). The SAED images of both the catalysts are showing spots emanating from a single crystalline material.

The morphological data from both mined and synthetic kieselguhr support material gave rise to the development of single-crystalline SPA catalysts grains.

4.3 Crystalline grain size of the catalysts synthesized from synthetic and mined kieselguhr.

The solid phosphoric acid catalyst grain size was analysed by measuring two perpendicular lengths from the grain in the TEM image with ImageJ software and then the length was calculated as the average dimension along the two axes of at least sixty grains[16].

Table 4.1 The mean grain size of the unpromoted and promoted SPA catalyst measured by TEM[17].

Catalyst	Average TEM grain size (nm)	Average XRD crystallite size(nm)
SPAM500	170 ± 8	110 ± 3
SPAMCa500	200 ± 6	180 ± 4
SPAMV500	247 ± 9	126 ± 3
SPAS500	188 ± 4	98 ± 3
SPASCa500	251 ± 3	98 ± 2

The grain sizes reported in Table 4.1 are larger than the XRD crystallite sizes calculated using the Scherrer equation assuming spherical crystallites in Chapter 3[18]. Data from XRD analysis can be used to measure crystallite size whereas data from TEM is used to measure the grain size[19]. It should be noted that the crystallite size does not necessarily correspond to the grain sizes, a single grain can be made up of one or more crystallites which can be separated by grain boundaries[20]. The TEM images of the SPA catalyst analyzed in this work has shown that the morphology of the catalyst has grains that are tetragonally and hexagonally shaped. This is a huge deviation from the spherical crystallites assumed by the Scherrer model.

The data shows that there is no significant difference in the grain size of the catalyst synthesized from mined kieselguhr (SPAM500) compared to the catalyst synthesized from synthetic kieselguhr (SPAS500) as shown in Figure 4.3 below.

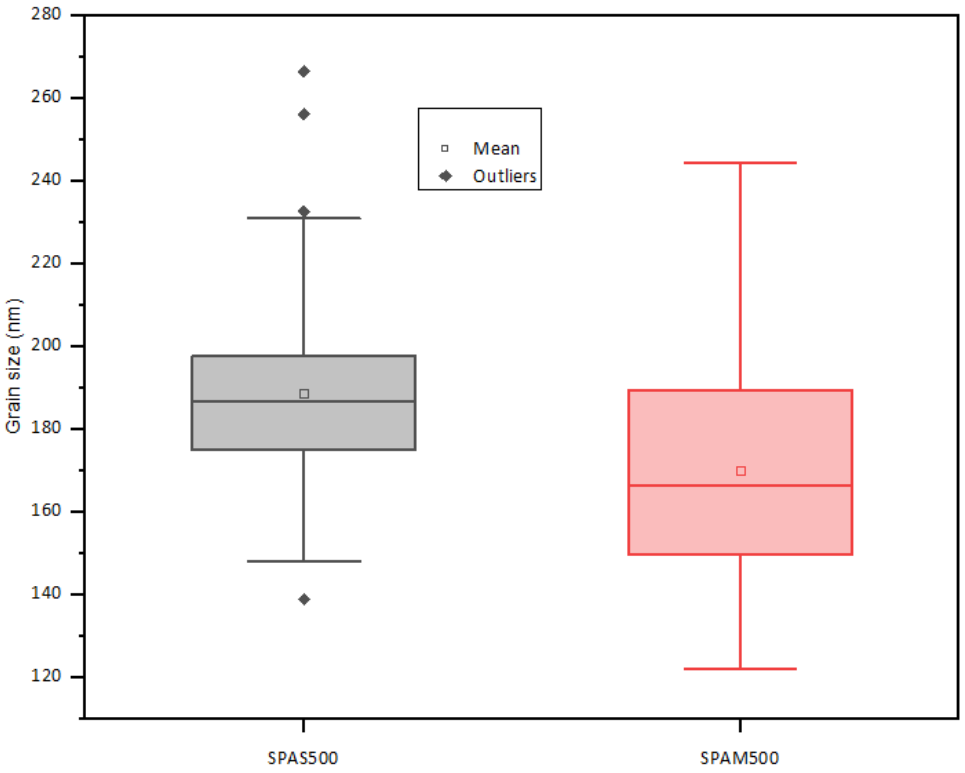


Figure 4.3 The grain size box plot of SPAM500 and SPAS500 showing the overlap in the grain sizes of the two catalysts.

The box plot in Figure 4.3 above is showing the overlapping of the two boxes of SPAS500 and SPAM500. In addition to that the median of the SPAS500 is also overlapping with the box of the SPAM500 catalyst. This means that there is no difference in grain size of the SPAS500 and SPAM500 catalyst synthesized from the two different kieselguhr types.

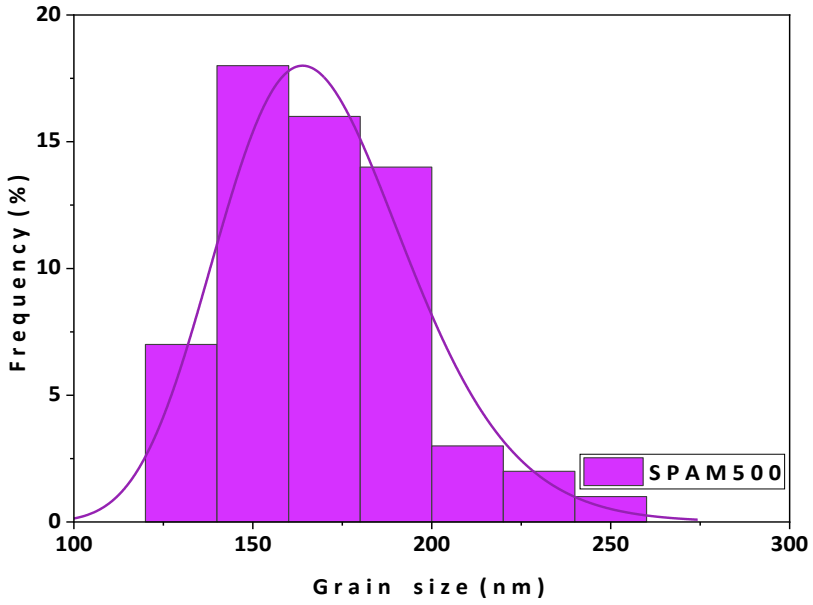


Figure 4.4 SPAM500 grain size distribution, the plot follows a lognormal distribution with grains size ranging from 122 nm to 244 nm $\pm$ 8 nm.

The grain size distribution of SPAM500 as shown in Figure 4.4, is influenced by the crystallization mechanism[21] in which, nucleation and growth process, start with nuclei formation on a homogeneous and random basis simultaneously with other grown crystallites[22]. The growing nucleus grows into a grain until it impinges on other growing grains, at which point the growth in the direction perpendicular to the interface stops without coarsening resulting in near-symmetrical variation in grain size[23].

The same crystallization mechanism of SPAM500 cannot be said for SPAMCa500 catalyst. SPAMCa500 grain size exhibited a bimodal distribution which is influenced by the chemical environment[24]. The presence of calcium atoms in the growing crystals of SPAMCa500 has not resulted in an increase or decrease of crystal size, it rather affected the grain size distribution as shown in Figure 4.5 below.

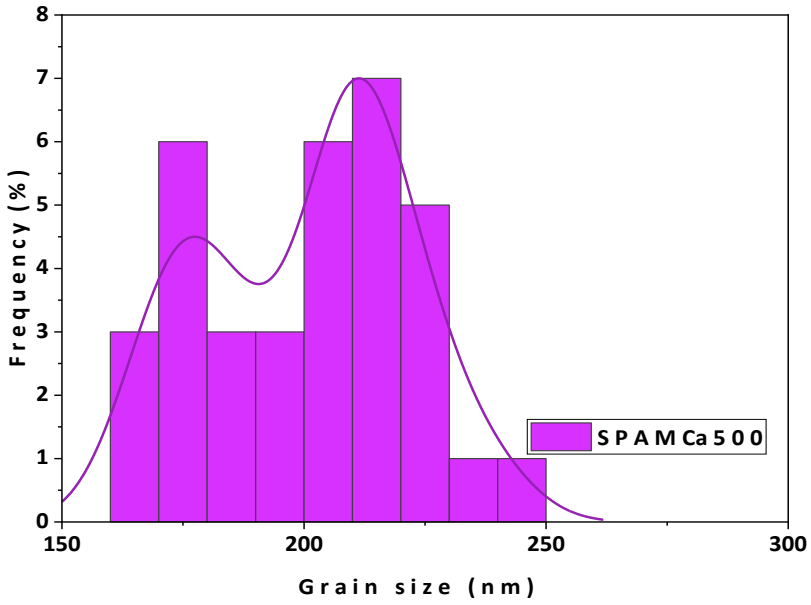


Figure 4.5 SPAMCa500 grain size distribution follows a Kernel smooth distribution.

After calcium promotion, the grain size range of SPAMCa500 was 164 nm – 240 nm $\pm$ 6 nm. This is the same grain size range as SPAM500; however, SPAMCa500 grain size distribution follows a bimodal Kernel smooth distribution[24]. This implies that there are two distinct grain size groups with two peaks. The nucleation and growth process which foster bimodal grain size distribution starts with nuclei formation on a heterogeneous and random basis[25]. The growing nucleus grows into a grain until it impinges on other growing grains, at which point the coarsening takes place resulting in asymmetrical grain size[26,27]. Three more size distribution analysis experiments of this sample were conducted to determine if the data set was having an outlier, the results have shown that the distribution is exactly a Kernel smooth distribution.

The SPAMV500 catalyst promoted with vanadium reported bigger grains compared to SPAM500 and the distribution also followed a Kernel smooth distribution as shown in Figure 4.6 below.

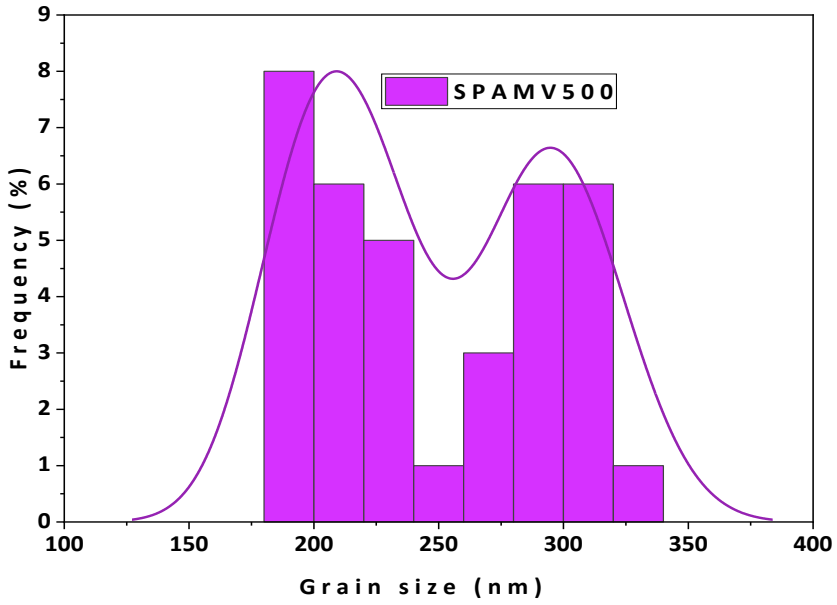


Figure 4.6 SPAMV500 grain size distribution of the catalyst promoted with vanadium.

The SPAMV500 grain sizes follow a Kernel smooth distribution with equally spaced grains. 50 % of the grains have size on the lower side ranging from 182 nm – 244 nm $\pm$ 8 nm. The other 50 % of the grains have grain size on the upper side ranging from 246 nm – 334 nm $\pm$ 8 nm. The crystallization mechanism of SPAMV500 follows the same route as SPAMCa500 reported above hence they have a similar type of grain size distribution.

The SPAMV500 catalyst showed a broader grain size distribution, ranging from 182 nm to 334 nm $\pm$ 7 nm. The maximum grain size of the SPAMV500 catalyst is higher than that of SPAMCa500. This could be a result of the difference in Van der Waals radius of calcium (231 pm) compared to that of vanadium (205 pm)[28]. The calcium divalent ion has a bigger ionic radius than the vanadium ions, the presence of ions with a smaller ionic radius causes a decrease in lattice parameters of the parent compound. The shrinkage in unit cells aids the coarsening process during crystallization which leads to the formation of larger grains[29]

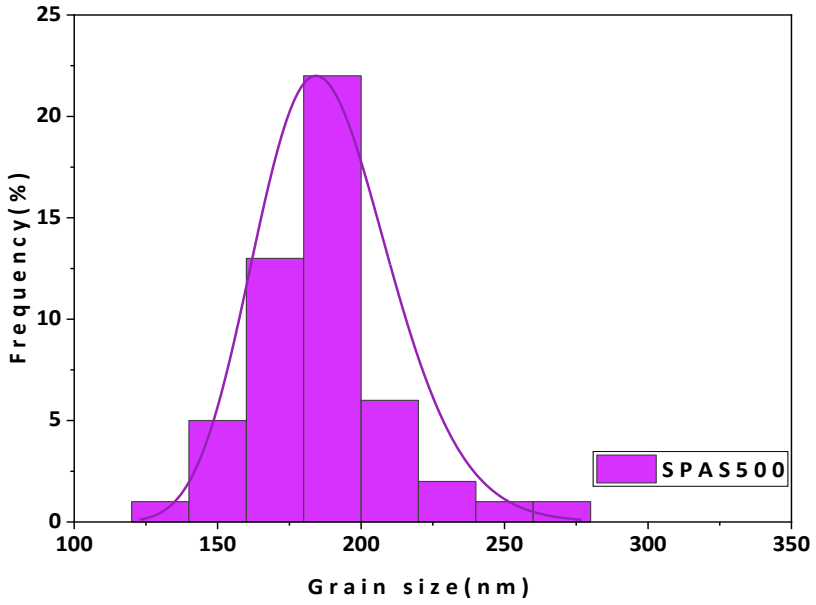


Figure 4.7 SPAS500 grain size distribution, the grains are following a lognormal distribution.

The SPACa500 catalyst grains size follows a lognormal distribution with a size range of 138 nm to 266 nm $\pm$ 3 nm.

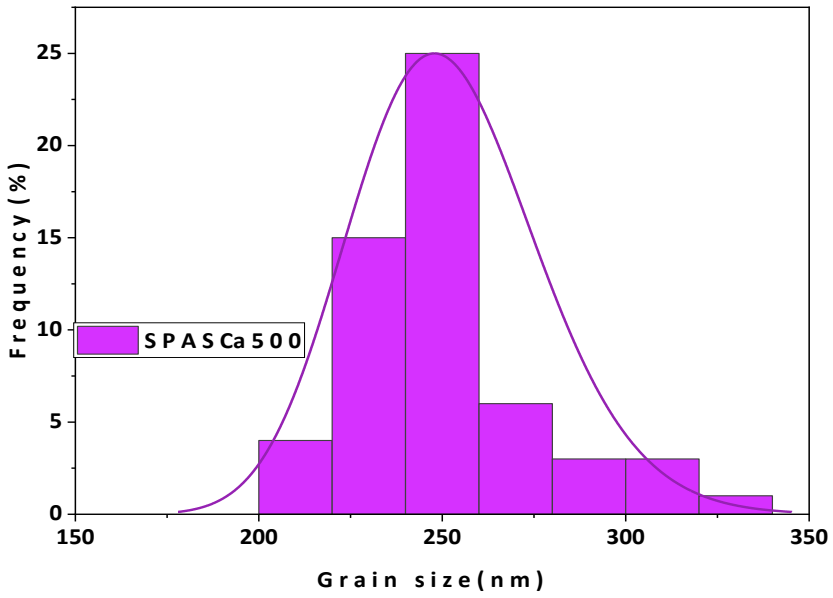


Figure 4.8 SPASCa500 catalyst grain size distribution.

The grain sizes of the SPASCa500 catalyst range from 204 nm to 338 nm $\pm$ 3 nm

However, the grain size distribution does not have a bimodal distribution like in SPAMCa500. This is attributed to differences in crystallization mechanisms of amorphous and crystalline silica[30]. The solid phase transformation of amorphous kieselguhr into crystal grains requires energy to initiate the nucleation process[31]. After which, the strain increases in the amorphous matrix as well as in grains giving rise to the inhomogeneous growth rate of the grains due to their elastic anisotropy[32]. In addition to this, the amorphous kieselguhr crystallization can result in more point defects, due to the existence of short-range structural order in which the type and density of the defects depend on growth and post-growth conditions experienced by the grain[33].

However, in cristobalite synthetic kieselguhr, there are cristobalite nuclei present fostering epitaxial crystallization which requires less thermal energy as compared to amorphous kieselguhr[34]. This results in inhomogeneous grains growth rates, ultimately giving well-structured grains.

4.4 Crystal grain geometry of the synthesized SPA catalysts.

The microstructural analysis using STEM shows the presence of tetragonal silicon pyrophosphate and hexagonally shaped silicon orthophosphate as shown in Figure 4.9 below. The silicon pyrophosphate is in a tetragonal crystal system and silicon orthophosphate has a hexagonal symmetry[35].

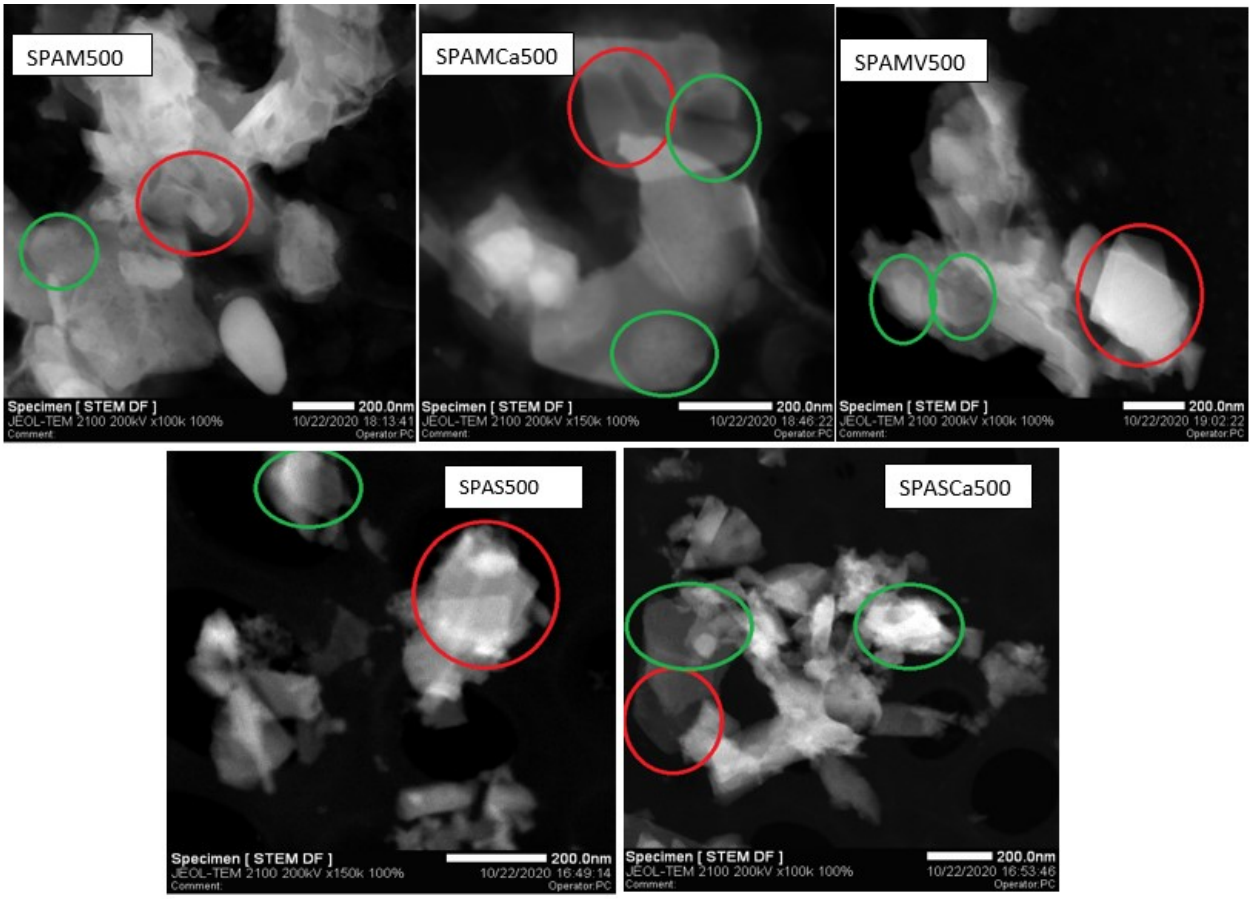


Figure 4.9 The crystal morphology and grain shapes of the SPA catalysts synthesized from both amorphous and synthetic kieselguhr. The images are showing distinct tetragonal shapes encircled in red, and the hexagonal system is encircled in green.

4.5 Atomic composition of the SPA catalysts synthesized from both amorphous and crystalline kieselguhr.

The atomic composition of four major elements of solid phosphoric acid was determined by STEM EDS. The obtained atomic compositions of silicon, phosphorus, calcium, and vanadium are reported in Table 4.2 below.

Table 4.2 Elemental composition of the synthesized SPA catalysts calcined at 500 ^{o}C.

Catalyst	Silicon (%)	Phosphorus (%)	Calcium (%)	Vanadium (%)
SPAM500	8 ± 0.1	20 ± 0.1	ND	ND
SPAMCa500	7 ± 0.1	15 ± 0.1	0.38 ± 0.1	ND
SPAMV500	9 ± 0.1	21 ± 0.1	ND	0.33 ± 0.1
SPAS500	7 ± 0.1	18 ± 0.1	ND	ND
SPASCa500	5 ± 0.1	13 ± 0.1	0.25 ± 0.1	ND

ND is not detected; this implies that the atomic concentration of a particular sample is below the detection limit of the instrument used.

SPAS500 and SPASCa500 reported a low percentage of silicon compared to SPAM500, SPAMCa500 and SPAMV500. This agrees with lower silicon dioxide content in synthetic kieselguhr relative to mined kieselguhr[36].

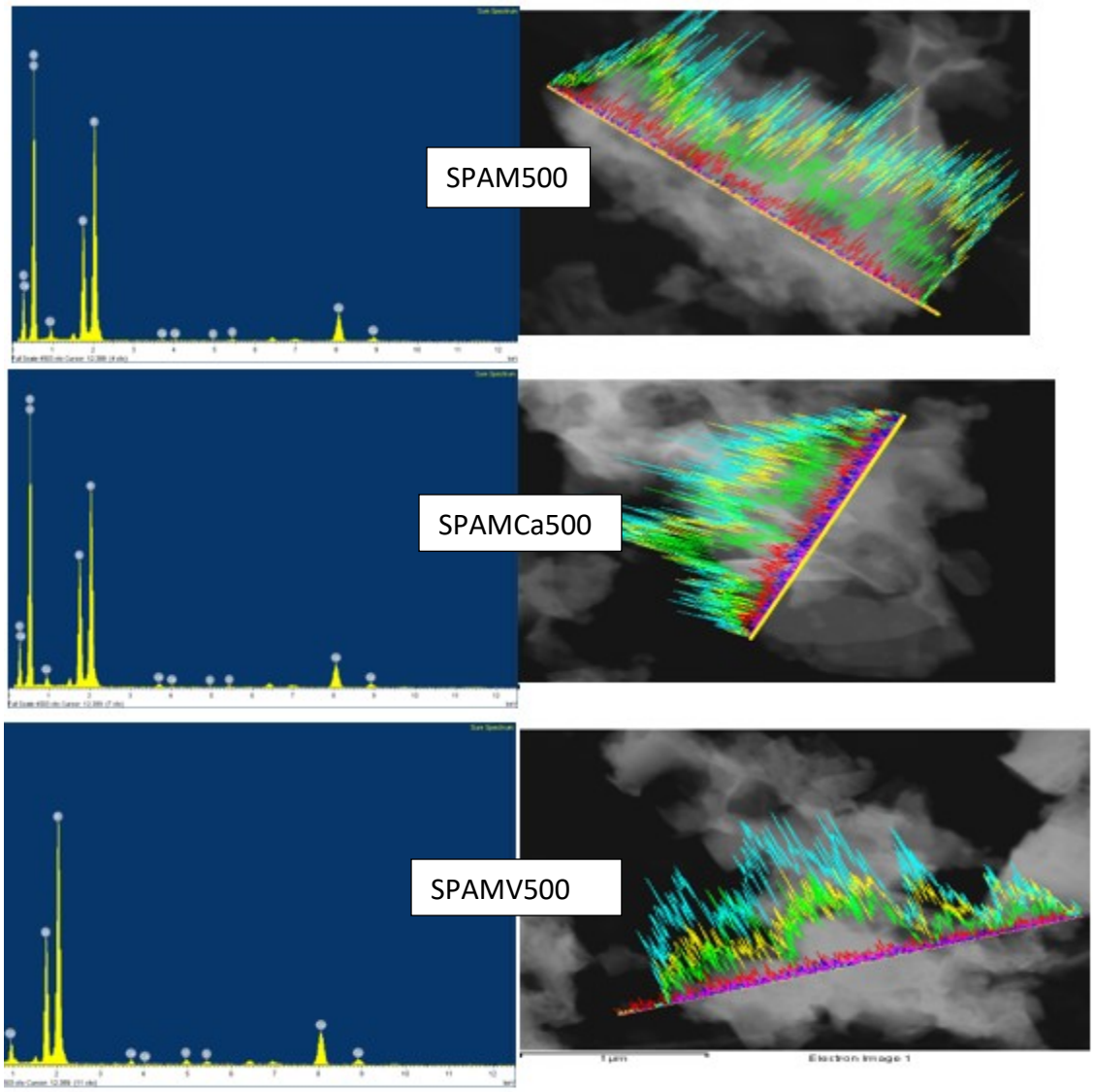


Figure 4.10 EDS map and the STEM images of the SPAM500, SPAMCa500 and SPAMV catalyst.

In the STEM image, yellow = oxygen, green = silicon, purple = vanadium, red = carbon,

Blue = calcium and blue/green = phosphorus.

The catalyst synthesized from mined kieselguhr has shown no variation in the silicon and phosphorus content as seen in Table 4.2 and Figure 4.10 above. The phosphorus to silicon ratio is 2.1 to 2.5, whereas the catalyst synthesized from synthetic kieselguhr has reported low silicon concentrations and have a phosphorus to silicon ratio of 2.7 and 2.8. The higher phosphorus to silicon ratios reported in catalyst synthesized from synthetic kieselguhr shows

that the catalyst could have more active material phosphorus pentoxide which is characterized as equivalent acid sites[37]. This agrees with the high silicon pyrophosphate phase of this catalyst reported in Chapter 3 and consequently higher catalyst activity[38].

The elemental distribution of silicon and phosphorus in SPA catalyst is crucial and here the elemental homogeneity was determined by focusing the beam of electrons on at least five different sample positions. The average percentages of the major elements are reported in Table 4.3 below[39].

Table 4.3 Calcium and vanadium composition determined by STEM EDS at different focal points of the sample.

Focal point number	SPAMCa500 (% Ca)	SPASCa500 (% Ca)	SPAMV500(%V)
1	0.32	0.10	0.33
2	0.36	ND	0.32
3	0.53	0.13	0.40
4	0.26	0.19	0.30
5	0.44	0.84	ND

ND = Not detected.

SPAMCa500 catalyst has shown the homogeneous distribution of calcium as shown in Table 4.3

However, the catalyst synthesized from synthetic kieselguhr has shown inhomogeneity to the calcium distribution with focal point 2 not detecting any calcium. It reported a large variation in calcium content ranging from 0.10 % to 0.84 %, possibly, this could be caused by the migration of calcium ions at a calcination temperature of 500 ^{o}C[40]. SPAMV500, although focal point five had no vanadium detected, does not translate into variation regarding vanadium distribution, it could be a result of random atomic distribution[41]. This is supported by the homogeneous distribution of vanadium in all other four focal points. Hence the absence of vanadium at focal point five is attributed to the random distribution of vanadium atoms with equal overall atomic composition resulting in one spot appearing as low to no vanadium[42].

4.6 References.

(1) Ipatieff, V. N.; Corson, B. B. Gasoline from Ethylene by Catalytic Polymerization. *Ind. Eng. Chem.* **1936**. https://doi.org/10.1021/ie50319a027.

(2) De Klerk, A. Oligomerization of 1-Hexene and 1-Octene over Solid Acid Catalysts. *Ind. Eng. Chem. Res.* **2005**. https://doi.org/10.1021/ie0487843.

(3) Ross, J. Heterogeneuos Catalysis. *Heterog. Catal.* **2012**, *2665* (96), iii. https://doi.org/10.1016/B978-0-444-53363-0.10009.

(4) Max, J. H.; Chia, W. L.; Ning, Y. Promoting Heterogeneous Catalysis beyond Catalyst Design. *Chem. Sci.* **2020**, *11*, 1456–1468. https://doi.org/10.1039/c9sc05947d.

(5) Araujo, L. R. R. de; Scofield, C. F.; Pastura, N. M. R.; Gonzalez, W. de A. H3PO4/Al2O3 Catalysts: Characterization and Catalytic Evaluation of Oleic Acid Conversion to Biofuels and Biolubricant. *Mater. Res.* **2006**, *9* (2), 181–184. https://doi.org/10.1590/S1516-14392006000200013.

(6) Hartman, T.; Geitenbeek, R. G.; Wondergem, C. S.; Van Der Stam, W.; Weckhuysen, B. M. Operando Nanoscale Sensors in Catalysis: All Eyes on Catalyst Particles. *ACS Nano* **2020**, *14* (4), 3725. https://doi.org/10.1021/acsnano.9b09834.

(7) Prinsen, P.; Luque, R. Chapter 1: Introduction to Nanocatalysts. In *RSC Catalysis Series*; Royal Society of Chemistry, 2019; Vol. 2019-January, pp 1–36. https://doi.org/10.1039/9781788016292-00001.

(8) Guo, B.; Wang, R.; Li, Y. The Performance of Solid Phosphoric Acid Catalysts and Macroporous Sulfonic Resins on Gasoline Alkylation Desulfurization. *Fuel Process. Technol.* **2010**. https://doi.org/10.1016/j.fuproc.2010.07.012.

(9) Gulati, S. T. Design Considerations for Advanced Ceramic Catalyst Supports. In *SAE Technical Papers*; 2000. https://doi.org/10.4271/2000-01-0493.

(10) Huang, W.; Li, W. X. Surface and Interface Design for Heterogeneous Catalysis. *Physical Chemistry Chemical Physics*. Royal Society of Chemistry January 2, 2019, pp 523–536. https://doi.org/10.1039/c8cp05717f.

(11) Khabbouchi, M.; Hosni, K.; Mezni, M.; Srasra, E. Structural Characterizations and Mechanical Behavior of Activated Clay-Based Si5(PO4)6O and SiP2O7 Compounds. *Silicon* **2020**, *12* (1), 117–

124. https://doi.org/10.1007/s12633-019-00218-1.

(12) Wilcher, F. P.; Chao, T. Solid Phosphoric Acid Catalyst. *United States Pat. US4912279A* **1992**.

(13) Fernández-Lorenzo, C.; Esquivias, L.; Barboux, P.; Maquet, J.; Taulelle, F. Sol-Gel Synthesis of SiO2P2O5 Glasses. *J. Non. Cryst. Solids* **1994**, *176* (2–3), 189–199. https://doi.org/10.1016/0022-3093(94)90077-9.

(14) Johnson, O. Acidity and Polymerization Activity of Solid Acid Catalysts. *J. Phys. Chem.* **1955**. https://doi.org/10.1021/j150531a007.

(15) Ross, W. H.; Jones, R. M.; Durgin, C. B. The Purification of Phosphoric Acid by Crystallization. *Ind. Eng. Chem.* **2002**, *17* (10), 1081–1083. https://doi.org/10.1021/IE50190A031.

(16) Schindelin, J.; Arganda-Carreras, I.; Frise, E.; Kaynig, V.; Longair, M.; Pietzsch, T.; Preibisch, S.; Rueden, C.; Saalfeld, S.; Schmid, B.; Tinevez, J. Y.; White, D. J.; Hartenstein, V.; Eliceiri, K.; Tomancak, P.; Cardona, A. Fiji: An Open-Source Platform for Biological-Image Analysis. *Nature Methods*. July 2012, pp 676–682. https://doi.org/10.1038/nmeth.2019.

(17) Buscombe, D.; Masselink, G. Grain-Size Information from the Statistical Properties of Digital Images of Sediment. *Sedimentology* **2009**, *56* (2), 421–438. https://doi.org/10.1111/j.1365-3091.2008.00977.x.

(18) Valério, A.; Morelhão, S. L. Usage of Scherrer's Formula in X-Ray Diffraction Analysis of Size Distribution in Systems of Monocrystalline Nanoparticles. *Inst. Physics, Univ. Sao Paulo, Sao Paulo, SP, Brazil* **2019**.

(19) Rice, S. B.; Chan, C.; Brown, S. C.; Eschbach, P.; Han, L.; Ensor, D. S.; Stefaniak, A. B.; Bonevich, J.; Vladár, A. E.; Walker, A. R. H.; Zheng, J.; Starnes, C.; Stromberg, A.; Ye, J.; Grulke, E. A. Particle Size Distributions by Transmission Electron Microscopy: An Interlaboratory Comparison Case Study. *Metrologia* **2013**, *50* (6), 663–678. https://doi.org/10.1088/0026-1394/50/6/663.

(20) Seyring, M.; Song, X.; Rettenmayr, M. Advance in Orientation Microscopy: Quantitative Analysis of Nanocrystalline Structures. *ACS Nano* **2011**, *5* (4), 2580–2586. https://doi.org/10.1021/nn1023126.

(21) Buscombe, D. Estimation of Grain-Size Distributions and Associated Parameters from Digital Images of Sediment. *Sediment. Geol.* **2008**, *210* (1–2), 1–10.

https://doi.org/10.1016/j.sedgeo.2008.06.007.

(22) Penn, R. L.; Soltis, J. A. Characterizing Crystal Growth by Oriented Aggregation. *CrystEngComm* **2014**, *16* (8), 1409–1418. https://doi.org/10.1039/c3ce41773e.

(23) An, S.; Li, J.; Li, Y.; Li, S.; Wang, Q.; Liu, B. Two-Step Crystal Growth Mechanism during Crystallization of an Undercooled Ni 50 Al 50 Alloy. *Sci. Rep.* **2016**, *6* (1), 1–10. https://doi.org/10.1038/srep31062.

(24) Magee, A. C.; Ladani, L. Representation of a Microstructure with Bimodal Grain Size Distribution through Crystal Plasticity and Cohesive Interface Modeling. *Mech. Mater.* **2015**, *82*, 1–12. https://doi.org/10.1016/j.mechmat.2014.12.002.

(25) Bard, A. B.; Zhou, X.; Xia, X.; Zhu, G.; Lim, M. B.; Kim, S. M.; Johnson, M. C.; Kollman, J. M.; Marcus, M. A.; Spurgeon, S. R.; Perea, D. E.; Devaraj, A.; Chun, J.; De Yoreo, J. J.; Pauzauskie, P. J. A Mechanistic Understanding of Nonclassical Crystal Growth in Hydrothermally Synthesized Sodium Yttrium Fluoride Nanowires. *Chem. Mater.* **2020**. https://doi.org/10.1021/acs.chemmater.9b04076.

(26) Li, C.; Seyring, M.; Li, X.; Zhong, Y.; Ren, Z.; Rettenmayr, M. Effect of Heat Treatment Combined with an Alternating Magnetic Field on Microstructure and Mechanical Properties of a Ni-Based Superalloy. *Metall. Mater. Trans. A Phys. Metall. Mater. Sci.* **2019**, *50* (4), 1837–1850. https://doi.org/10.1007/s11661-019-05141-z.

(27) Stawski, T. M.; Freeman, H. M.; Van Driessche, A. E. S.; Hövelmann, J.; Besselink, R.; Wirth, R.; Benning, L. G. Particle-Mediated Nucleation Pathways Are Imprinted in the Internal Structure of Calcium Sulfate Single Crystals. *Cryst. Growth Des.* **2019**, *19* (7), 3714–3721. https://doi.org/10.1021/acs.cgd.9b00066.

(28) Vermaas, F. H. S.; Schmidt, E. R. The Influence of Ionic Radii of Cations and Covalent Forces on the Unit Cell Dimensions of Spinels. *Beiträge zur Mineral. und Petrogr.* **1959**, *6* (4), 219–232. https://doi.org/10.1007/BF01130325.

(29) Chen, X.; Qian, Y.; Chen, Z.; Gui, Z. Effects of Ionic Radius on Structure and Superconductivity for High-Tc Oxide Superconductors. *Phys. Status Solidi* **1992**, *130* (2), 415–420. https://doi.org/10.1002/pssa.2211300219.

(30) R.M. Carr, W. S. F. Some Observations on the Crystallization of Amorphous Silica. *Am. Mineral.* **1958**, *43*, 908–916.

(31) Li, C. T. Transformation Mechanism between High-Quartz and Keatite Phases of LiAlSi2O6 Compositon. *Acta Crystallogr. Sect. B Struct. Crystallogr. Cryst. Chem.* **1971**, *27* (6), 1132–1140. https://doi.org/10.1107/s0567740871003649.

(32) Viladot, D.; Veron, M.; Gemmi, M.; Peiro, F.; Portillo, J.; Estrade, S.; Mendoza, J.; Llocra-Isern, N.; Nicolopoulos, S. Orientation and Phase Mapping in the Transmission Electron Microscope Using Precession-Assisted Diffraction Spot Recognition: State-of-the-Art Results. *J. Microsc.* **2013**, *252* (1), 23–34. https://doi.org/10.1111/jmi.12065.

(33) Ori, G.; Montorsi, M.; Pedone, A.; Siligardi, C. Insight into the Structure of Vanadium Containing Glasses: A Molecular Dynamics Study. In *Journal of Non-Crystalline Solids*; 2011; Vol. 357, pp 2571–2579. https://doi.org/10.1016/j.jnoncrysol.2011.02.002.

(34) Horwell, C. J.; Williamson, B. J.; Llewellin, E. W.; Damby, D. E.; Le Blond, J. S. The Nature and Formation of Cristobalite at the Soufrière Hills Volcano, Montserrat: Implications for the Petrology and Stability of Silicic Lava Domes. *Bull. Volcanol.* **2013**, *75* (3), 1–19. https://doi.org/10.1007/s00445-013-0696-3.

(35) Poojary, D. M.; Borade, R. B.; Clearfield, A. Structural Characterization of Silicon Orthophosphate. *Inorganica Chim. Acta* **1993**, *208* (1), 23–29. https://doi.org/10.1016/S0020-1693(00)82879-0.

(36) Southard, R. J.; Li, X.; Eisen, E. A.; Pinkerton, K. E. Silica, Crystalline. In *Encyclopedia of Toxicology: Third Edition*; Elsevier, 2014; pp 266–269. https://doi.org/10.1016/B978-0-12-386454-3.00061-0.

(37) Fougret, C. M.; Atkins, M. P.; Hölderich, W. F. Influence of the Carrier on the Catalytic Performance of Impregnated Phosphoric Acid in the Hydration of Ethylene. *Appl. Catal. A Gen.* **1999**. https://doi.org/10.1016/S0926-860X(98)00416-5.

(38) Huhti, A.-L.; Gartaganis, P. A. The Composition of the Strong Phosphoric Acids. *Can. J. Chem.* **1956**. https://doi.org/10.1139/v56-102.

(39) Asadabad, M. A.; Eskandari, M. J. Transmission Electron Microscopy as Best Technique for Characterization in Nanotechnology. *Synth. React. Inorganic, Met. Nano-Metal Chem.* **2015**, *45* (3), 323–326. https://doi.org/10.1080/15533174.2013.831901.

(40) Freund, H. J. The Surface Science of Catalysis and More, Using Ultrathin Oxide Films as Templates: A Perspective. *J. Am. Chem. Soc.* **2016**, *138* (29), 8985–8996. https://doi.org/10.1021/jacs.6b05565.

(41) Fan, Z.; Gao, F.; Jiang, B.; Que, Z. Impeding Nucleation for More Significant Grain Refinement. *Sci. Rep.* **2020**, *10* (1), 1–11. https://doi.org/10.1038/s41598-020-66190-8.

(42) Hirvonen, P.; Fan, Z.; Ervasti, M. M.; Harju, A.; Elder, K. R.; Ala-Nissila, T. Energetics and Structure of Grain Boundary Triple Junctions in Graphene. *Sci. Rep.* **2017**, *7* (1), 1–14. https://doi.org/10.1038/s41598-017-04852-w.

Chapter 5.

5.1 Conclusions and recommendations for future studies.

The cylindrically shaped catalyst SPAM, SPAMCa, SPAS and SPASCa series were successfully synthesized. The experimental data of this work has shown that the silica source, either amorphous kieselguhr or crystalline synthetic kieselguhr, did not influence the cylindrical shaping of the synthesized SPA catalyst. However, the synthesis of the quadrilobed shaped catalyst SPAMQ series was hindered by the failure of polymer inserts as they failed to withstand the palletization pressure and deformed. In this work, it was noted that there is no correlation between the failure of polymers inserts and the silica source, therefore variation in silicon dioxide content of the support material does not influence forming of the SPA catalyst. In that regard, the use of a metallic die with quadrilobed shapes should be considered in the future synthesis of quadrilobed SPA catalysts. The synthesis of the vanadium promoted SPAMV series was herein achieved with no challenges.

The SPA catalysts synthesis conditions have been shown to influence the physical parameters of the SPA catalyst differently. The extrudability of the SPA material has always been a driving force in employing the mixing temperature as high as 200 ^{o}C[1]. Herein, the SPAM, SPAMCa, SPAS and SPASCA catalyst was synthesized with a mixing temperature of 75 ^{o}C and pre-calcined before forming and later successfully formed cylindrical extrudates. That means the mixing temperature of silica and phosphoric acid is independent of the extrudability of the material, but the pre-calcination step influences the forming of a cylindrical SPA catalyst. The mixing of the raw materials at a lower temperature is advantageous in limiting the migration of essential elements resulting in the homogeneous synthesis of the SPA catalyst, this is supported by the elemental distribution data of the SPA catalyst synthesized in this dissertation[2].

The data from all the synthesized SPA catalysts in this work have shown that there is a notable decrease in free acid associated with an increase in calcination temperature from 400 ^{o}C to 800 ^{o}C. Although the synthesized SPA catalyst structure was shown to be stable up to 600 ^{o}C calcination temperature. It is concluded that the catalyst synthesized from amorphous kieselguhr has higher free acid content compared to the catalyst synthesized from synthetic

crystalline kieselguhr. This is after all the catalyst synthesized from amorphous kieselguhr had higher P_2O_5 content in all corresponding calcination temperatures. This supports the deduction that silicon dioxide in crystalline kieselguhr strongly reacted with phosphoric acid to form silicon phosphates whereas there are weak interactions between phosphoric acid and silica in catalysts synthesized from amorphous kieselguhr[3].

In this work, different crystalline phases were identified, these are silicon orthophosphate, silicon pyrophosphate, hydrated calcium hydrogen phosphate and vanadium pyrophosphate. Quantification of the minority crystalline phases was hindered by the overlapping with the majority crystalline phases. The benefit of the formation of additive phases such as vanadium pyrophosphate which was reported for vanadium doped SPA catalyst on SPA catalyst hardness was outweighed by the development of larger crystal grains (larger grains foster lower catalyst hardness).

Furthermore, calcination temperature also affected the crystallinity of the SPA catalyst albeit differently. An increase in calcination temperature was correlated to an increase in crystallization even though, the catalyst synthesized from amorphous silica has shown a decrease in silicon orthophosphate on the increase of the calcination temperature. This led to a hypothesis that the conversion of silicon orthophosphate to silicon pyrophosphate is an endothermic reaction[4].

There is no significant variation in the average grain size of the catalyst synthesized from amorphous kieselguhr compared to the catalysts synthesized from crystalline kieselguhr. Nevertheless, calcium and vanadium promotion increased the grain size of the catalyst synthesized from both silica sources even though they contain different grain size distributions. In amorphous kieselguhr, both calcium and vanadium influenced the formation of grain size that follows a bimodal distribution but in synthetic kieselguhr, calcium influenced the formation of grains that follow a lognormal grain size distribution. This led to the conclusion that calcium fosters the development of a homogeneous nucleation process in the crystallization of the SPA catalyst synthesized from amorphous kieselguhr[5].

The fact that both calcium and vanadium promotion enhances the synthesis of larger grain sizes compared to the grain size of unpromoted SPA catalyst means that the metal promotion of SPA catalyst by calcium and vanadium cannot result in improved SPA catalyst hardness[6]. Since small grain size inhibits migration of dislocations as they have a large number of grain boundaries per unit area[7]. Subsequently, there could be dislocations accumulated up at the grain boundaries, this gives rise to internal stresses, as a result, energy is needed to initiate material flow and to overcome dislocation pile-up stresses ultimately resulting in increased catalyst hardness[8].

Therefore the SPA catalyst promoter that fosters the synthesis of smaller grain size of the catalyst compared to the grain size of unpromoted SPA catalyst will enhance SPA catalyst hardness[9], this forms the scope of the future research to solve the mechanical strength of the SPA catalyst. The data from the STEM-EDS study has revealed that there is a homogeneous distribution of silicon, phosphorus, calcium, and vanadium in all synthesized SPA catalysts. It is here concluded that the SPA catalyst impregnation synthesis method is stable and promote high repeatability which should give rise to the formation of uniform pores with a distinct pore volume[10]. This was verified by an XRD measurement in which the calcium phosphate hydrate hydrogen and vanadium pyrophosphate phases were referenced using the ICDD database.

Herein, the SPA catalyst porosity studies were conducted to gain an insight into the effect of synthesis conditions on SPA catalyst pore structure. It is here reported that there is a steady increase in mercury intrusion macro-pore volume from the synthesized SPA catalysts calcined between 400 ^{o}C and 600 ^{o}C. This implies that the catalyst structure was stable at this calcination temperature range[11]. However, a steep increase in macropore volume of the SPA catalysts calcined beyond 600 ^{o}C was reported.

This was caused by the structural collapse and decomposition of silicon phosphates to silicon dioxide and phosphorus pentoxide[10]. To that effect, it was decided that 500 ^{o}C calcination temperature is the optimum calcination temperature that retains the SPA catalyst structure integrity. The SPA catalyst porosity analysis was also conducted using a complimentary N_2 adsorption technique. The BJH desorption pore-volume of the SPA catalyst calcined at 500 ^{o}C was found to be decreasing by at least five times on calcium and vanadium promotion. The

porosity study forms the novelty part of this study since this kind of data is not available in the open literature.

In addition to that, the catalyst calcined at 500 ^{o}C should have the optimum specific catalyst surface area. It was reported that the BET surface area of the synthesized SPAMCa500 catalyst was 76.6 ± 0.3 % lower than that of SPAM500. The same result was observed for SPAMV500 which was 48.7 ± % 0.3 lower than that of SPAM500. This led to the deduction that calcium promotion of SPA catalyst can lead to significant BET surface area losses, but vanadium promotion can result in a moderate loss of BET surface area.

Analysis into the effect of calcium and vanadium promotion on the synthesized SPA catalyst pore volume was also conducted to validate the conclusion on BET surface area losses. The BJD desorption pore volumes with a diameter between 1.7 nm and 300 nm for SPAMCa500 was 87.4 ± 1 % lower than that of SPAM500 with the same pore diameter. Further, the BJD desorption pore volume of the pores with a diameter between 1.7 nm and 300 nm for SPAMV500 was 78.3 ± 1 % lower than that of SPAM500 with the same pore diameter. This shows that calcium promotion of SPA catalyst resulted in micropore impediment[12]. That is an accumulation of the calcium atoms at the opening of the micropores or just inside the pore channels causing micropore blockages, these micropores have a significant contribution to the surface and once they are blocked a decrease in the surface area is evident[13]. This led to the conclusion that vanadium is a better promoter of SPA catalyst than calcium.

The pore volume and pore structure of the SPA catalyst forms the basis of future research on SPA catalyst development. The work can focus on the development of granular microstructure by employing different structure-directing agents such that, the increase in grain size caused by vanadium promotion in this work will be engineered in such a way that the voids between the SPA catalyst crystal grains will provide mesopores[14]. The formed mesopores can enhance the catalyst BET surface area[15]. However, this will also depend on synthesis methodology and the amount of the catalyst synthesised[16]. The use of FT-IR spectroscopy to unravel the different functional groups in the newly engineered SPA catalyst in future is here suggested.

The limitation of this research is that the synthesized SPA catalyst was not subjected to performance testing to determine the relationship between the synthesized SPA catalyst structure and its efficiency in propylene oligomerization. However, this is part of the work to be conducted in future. Knowledge from such a test can be used in synchronization with the novel ideas generated out of this research to enhance the optimization of the SPA catalyst structure.

5.2 References.

(1) Coetzee, J. H.; Mashapa, T. N.; Prinsloo, N. M.; Rademan, J. D. An Improved Solid Phosphoric Acid Catalyst for Alkene Oligomerization in a Fischer-Tropsch Refinery. *Appl. Catal. A Gen.* **2006**, *308*, 204–209. https://doi.org/10.1016/j.apcata.2006.04.023.

(2) Stawski, T. M.; Freeman, H. M.; Van Driessche, A. E. S.; Hövelmann, J.; Besselink, R.; Wirth, R.; Benning, L. G. Particle-Mediated Nucleation Pathways Are Imprinted in the Internal Structure of Calcium Sulfate Single Crystals. *Cryst. Growth Des.* **2019**, *19* (7), 3714–3721. https://doi.org/10.1021/acs.cgd.9b00066.

(3) Rangsriwatananon, K.; Chaisena, A.; Thongkasam, C. Thermal and Acid Treatment on Natural Raw Diatomite Influencing in Synthesis of Sodium Zeolites. *J. Porous Mater.* **2008**, *15* (5), 499–505. https://doi.org/10.1007/s10934-007-9098-2.

(4) Poojary, D. M.; Borade, R. B.; Campbell, F. L.; Clearfield, A. Crystal Structure of Silicon Pyrophosphate (Form I) from Powder Diffraction Data. *J. Solid State Chem.* **1994**, *112* (1), 106–112. https://doi.org/10.1006/jssc.1994.1273.

(5) Spinella, C.; Lombardo, S.; Priolo, F. Crystal Grain Nucleation in Amorphous Silicon. *J. Appl. Phys.* **1998**, *84* (10), 5383–5414. https://doi.org/10.1063/1.368873.

(6) Jung, B. B.; Lee, H. K.; Park, H. C. Effect of Grain Size on the Indentation Hardness for Polycrystalline Materials by the Modified Strain Gradient Theory. *Int. J. Solids Struct.* **2013**, *50* (18), 2719–2724. https://doi.org/10.1016/j.ijsolstr.2013.05.002.

(7) Stoloff, N. S. Intermetallics: Mechanical Properties. In *Encyclopedia of Materials: Science and Technology*; Elsevier, 2001; pp 4213–4225. https://doi.org/10.1016/b0-08-043152-6/00740-3.

(8) Li, K.; Li, S.; Xue, Y.; Fu, H. Microstructure Characterization and Mechanical Properties of a Laves-Phase Alloy Based on Cr2Nb. *Int. J. Refract. Met. Hard Mater.* **2013**, *36*, 154–161. https://doi.org/10.1016/j.ijrmhm.2012.08.009.

(9) Naghizadeh, M.; Mirzadeh, H. Effects of Grain Size on Mechanical Properties and

Work-Hardening Behavior of AISI 304 Austenitic Stainless Steel. *steel Res. Int.* **2019**, *90* (10), 1900153. https://doi.org/10.1002/srin.201900153.

(10) Menad, K.; Feddag, A.; Rubenis, K. Synthesis and Study of Calcination Temperature Influence on the Change of Structural Properties of the LTA Zeolite. *Rasayan J. Chem* **2016**, *9*, 788–797.

(11) Ding, Y.; Zhao, C.; Li, Y.; Ma, Z.; Lv, X. Effect of Calcination Temperature on the Structure and Catalytic Performance of the Cu-Mcm-41 Catalysts for the Synthesis of Dimethyl Carbonate. *Quim. Nova* **2018**, *41* (10), 1156–1161. https://doi.org/10.21577/0100-4042.20170291.

(12) Jimeńez-García, G.; De Lasa, H.; Quintana-Solorźano, R.; Maya-Yescas, R. Catalyst Activity Decay Due to Pore Blockage during Catalytic Cracking of Hydrocarbons. *Fuel* **2013**, *110*, 89–98. https://doi.org/10.1016/j.fuel.2012.10.082.

(13) Cychosz, K. A.; Thommes, M. Progress in the Physisorption Characterization of Nanoporous Gas Storage Materials. *Engineering*. Elsevier Ltd August 1, 2018, pp 559–566. https://doi.org/10.1016/j.eng.2018.06.001.

(14) Kutarov, V. V. Analytical Equation for the Mesopore Size Distribution Function of Open Cylindrical Capillaries. *Adsorpt. Sci. Technol.* **2019**, *37* (6), 468–479. https://doi.org/10.1177/0263617419846000.

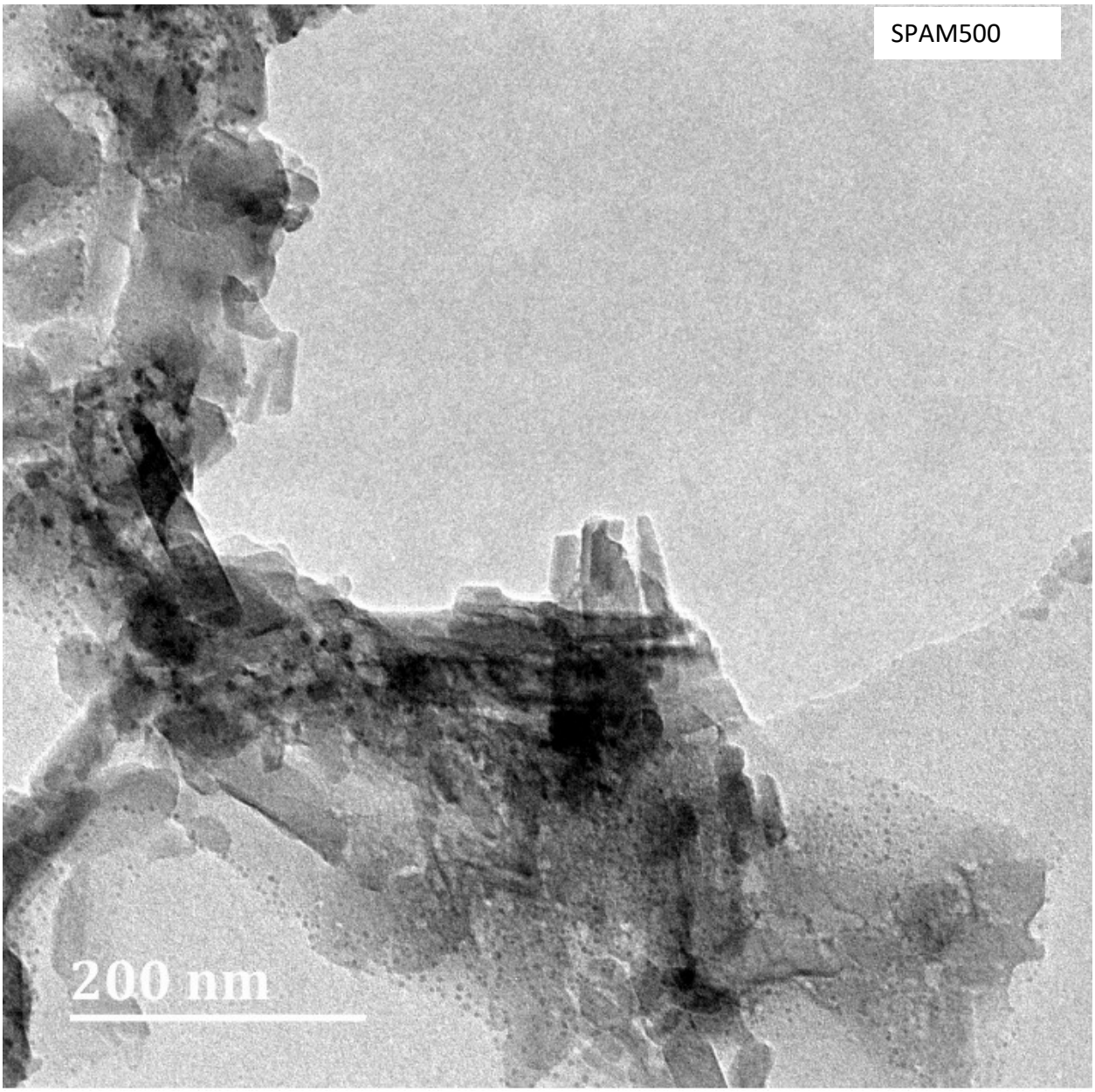
(15) Zhang, L.; Ke, M.; Song, Z.; Liu, Y.; Shan, W.; Wang, Q.; Xia, C.; Li, C.; He, C. Improvement of the Catalytic Efficiency of Butene Oligomerization Using Alkali Metal Hydroxide-Modified Hierarchical ZSM-5 Catalysts. *Catalysts* **2018**, *8* (8). https://doi.org/10.3390/CATAL8080298.

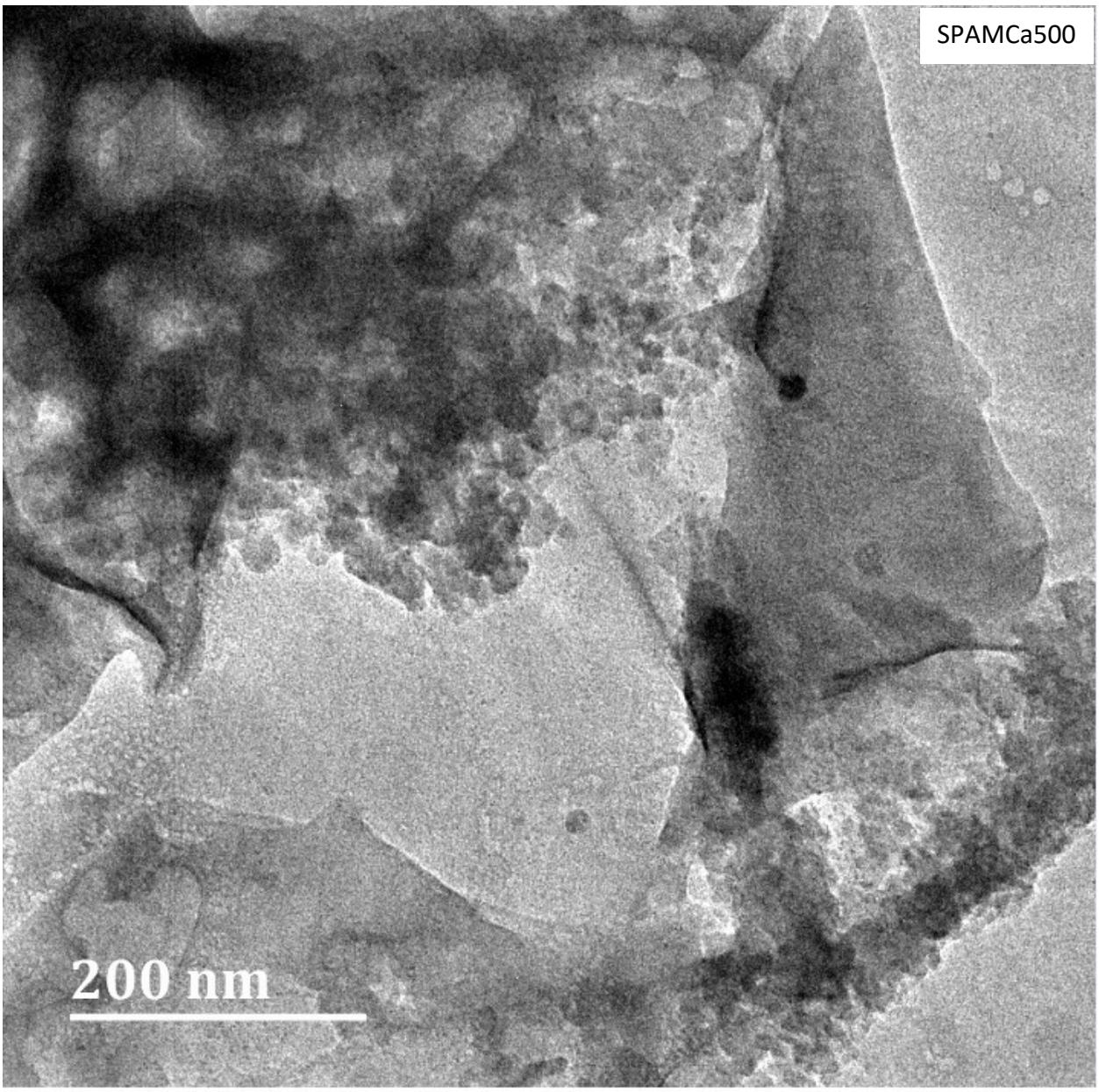
(16) Villarroel Rocha, J.; Barrera, D.; Sapag, K. Improvement in the Pore Size Distribution for Ordered Mesoporous Materials with Cylindrical and Spherical Pores Using the Kelvin Equation. In *Topics in Catalysis*; 2011. https://doi.org/10.1007/s11244-011-9631-z.

Appendix.

Chapter 4 Supporting information.

TEM images of the SPAM, SPAMCa and SPAMV catalysts.




SPAMCa500
200 nm

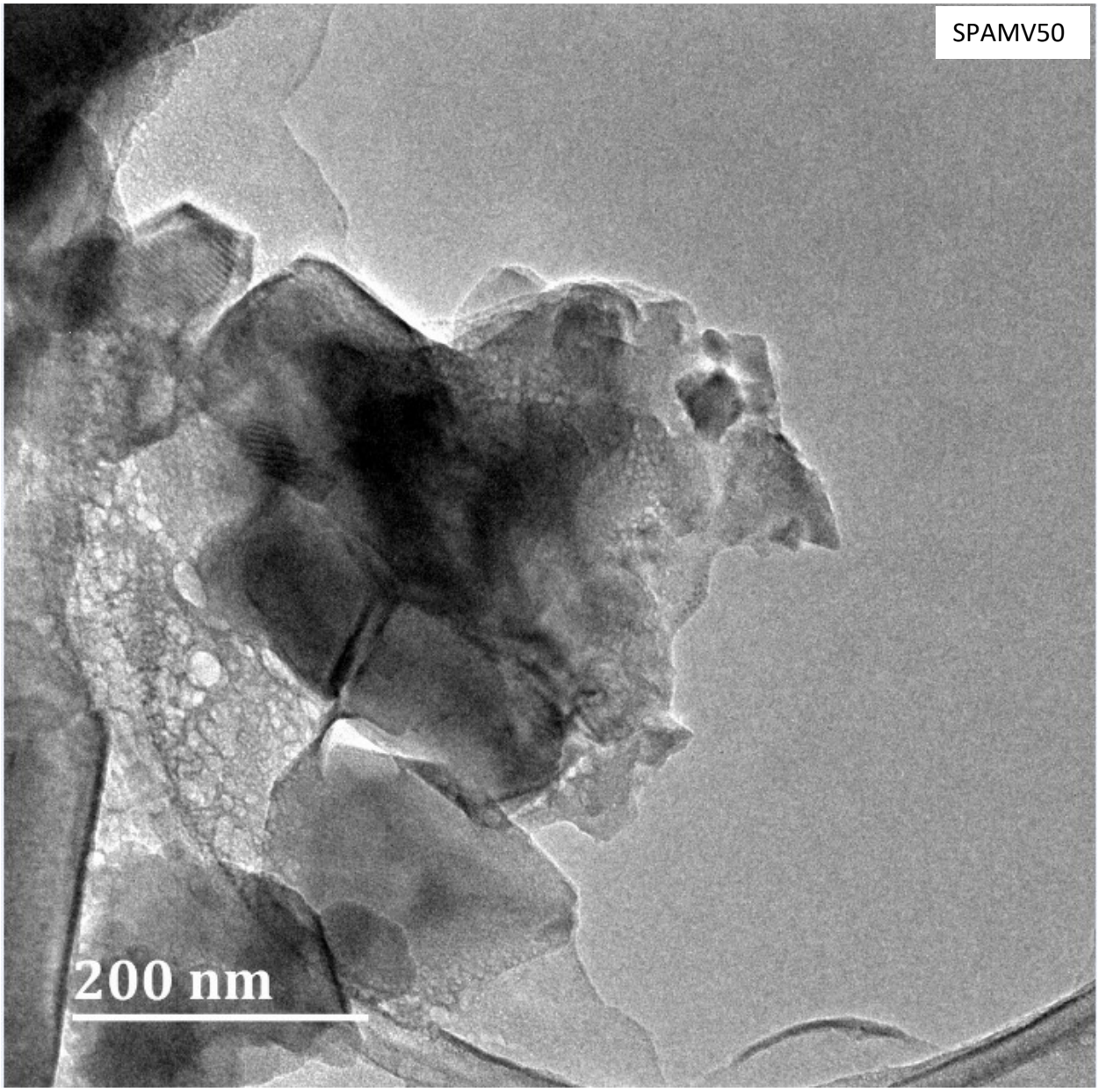


Table A1. SPA catalysts mass loss on ignition.

Catalyst	Mass(g) at 400 ^{o}C	Mass(g) at 800 ^{o}C	Mass(g) at 1000 ^{o}C
SPAM	5.2 ± 0.1	4.8 ± 0.1	4.6 ± 0.1
SPAMV	5.1 ± 0.1	4.6 ± 0.1	4.6 ± 0.1
SPAS	5.4 ± 0.1	4.9 ± 0.1	4.8 ± 0.1